Angular Filters for Angular Domain Imaging Optical Tomography in Highly Scattering Media

by

Paulman Chan

B.A.Sc, Simon Fraser University, 2005

A THESIS SUBMITTED IN PARTIAL FULFILLMENT
OF THE REQUIREMENTS FOR THE DEGREE OF
MASTER OF APPLIED SCIENCE
in the School of Engineering Science

SIMON FRASER UNIVERSITY

Summer 2008

APPROVAL

Name: **Paulman Konn Yan Chan**

Degree: **Master of Applied Science**

Title of Thesis: **Angular Filters for Angular Domain Imaging Optical Tomography in Highly Scattering Media**

Examining Committee:

Chair: **Dr. Andrew Rawicz**
Professor, School of Engineering Science

_____

Dr. Glenn Chapman
Senior Supervisor
Professor, School of Engineering Science

_____

Dr. Bozena Kaminska
Supervisor
Professor, School of Engineering Science

_____

Dr. Marinko Sarunic
Internal Examiner
Assistant Professor, School of Engineering Science

Date Defended/Approved: _____

Abstract

Angular Domain Imaging performs Optical Tomography imaging through highly scattering media by rejecting scattered light through micromachined Angular Filter Array (AFA) tunnels or an aperture-based Spatial Filter (SF) while accepting non-scattered light with only small angular deviations from the source. AFA imaging using a laser diode source (λ = 670 nm) resolves 153 µm structures at a Scattering Ratio (SR) of 10^7:1 in a milk-based scattering solution and 204 µm patterns for chicken tissue $\leq$ 3.8 mm thick. Carbon deposition and NH_4OH silicon roughening of the AFA tunnels is shown to reduce background scattered light. Smaller tunnel geometries and scan steps improve image resolution. A lens with aperture ADI Spatial Filtering was studied to verify theoretical predictions of the tradeoff between resolution and scattered light rejection. SF ADI with an Argon laser resolved 102 µm structures in a SR = 1.4×10^7:1 milk solution.

Acknowledgements

I would like to thank my supervisor, Dr. Glenn Chapman, for guiding me through both my undergraduate thesis and now my master's thesis work. I have learned about seeing the big picture without neglecting the fine details, the importance of valuing those who study under you, and not an insignificant assortment of science-fiction trivia and tech news due to the privilege of working with you. I would also like to thank my committee members, Dr. Bozena Kaminska and Dr. Marinko Sarunic, who have both been involved with my research and provided direction, in addition to my committee chair, Dr. Andrew Rawicz. I would like to thank the Natural Sciences and Engineering Research Council of Canada for funding one year of my graduate research. I greatly appreciate the opportunity to work with Fartash Vasefi on this project over the last three years. In addition, I will always remember my time spent in Dr. Chapman's research laboratory, informally known as the *Sardine Can*, with great affection due to the numerous friends gained as a result. I would like to thank William Woods for his expertise in assisting and facilitating much of my clean room operations. I would also like to thank my colleagues and classmates for enriching (rather than depressing) my studies and research over the last eight years at Simon Fraser University, with special mention to the members of Dr. Ash Parameswaran's research laboratory. To my family, thank you for making this journey of mine possible – I could not be where I am with the opportunities afforded to me if it were not for you. Ultimately, I thank my God, through Jesus Christ, who said "let there be light", and there was **light** – and later, universities, too.

Table of Contents

List of Figures

List of Tables

List of Abbreviations

ADI:	Angular Domain Imaging
AFA:	Angular Filter Array
CSC:	Cylindrical-spherical-cylindrical
CCD:	Charge-coupled device
CMOS:	Complimentary metal-oxide-semiconductor
DOT:	Diffuse Optical Tomography
MFP:	Mean Free Path
NIR:	Near-infrared
OCT:	Optical Coherence Tomography
OT:	Optical Tomography
SR:	Scattering ratio
SMCA:	Silicon micromachined collimating array
TD:	Time Domain

Chapter 1

Introduction

X-ray imaging has traditionally been employed in medical imaging to determine the contents and structure of tissue because x-ray wavelengths are able to pass through tissue largely unscattered. Thus, two-dimensional projection and computed tomography x-ray imaging are often used for diagnostic and routine screening of patients. However, this introduces an element of risk for human subjects because x-rays are a form of ionizing radiation that can damage cells and are a known carcinogen [1]. Visible and near-infrared wavelengths are non-ionizing, and thus can be safer for imaging human tissue compared to x-rays. In addition, various constituents of human tissue can respond differently to light depending on the wavelength [2], thus yielding additional information regarding the physical and chemical contents of the tissue (e.g. tissue vascularization or blood oxygen content). Using optical wavelengths instead of x-rays also allows for the use of smaller, low-power, more portable, and relatively low-cost sources such as laser diodes, which broadens the potential applications for optical imaging.

Optical imaging through highly scattering media has applications ranging from medical imaging of human tissues, to maritime navigation through fog, et cetera. However, an extremely high proportion of the light that enters a highly scattering medium is scattered along random paths within the medium before emerging at a wide range of angles. Such high proportions of scattered to non-scattered light obscure the contents of the medium from simple optical inspection and make it difficult to resolve an accurate image. Biological tissues exhibit extremely high scattered to non-scattered light ratios that make it difficult to image through even modest tissue thicknesses. For example, one estimate in the literature describes a scattered to non-scattered photon ratio of 10^{11}:1 as a significant target for successful image detection through a 5 cm thickness of human breast tissue for optical mammography [3].

This thesis extends research on a relatively new Optical Tomography (OT) approach for imaging through highly scattering media known as Angular Domain Imaging (ADI). The

use of an Angular Filter Array (AFA), known as the Silicon Micromachined Collimating Array (SMCA) in prior ADI research, is explored [4], [5], [6], [7], [8], [9], along with Spatial Filtering ADI with the use of an aperture.

This introductory chapter presents background and theory relating to Optical Tomography and various OT methods currently in use. In addition, the research objectives and purpose for this thesis document are outlined and an overview of its structure is given.

1.1 Optical Tomography and current methods

Optical Tomography is a technique for observing the structure of a highly scattering medium under illumination by extracting an image from the light that emerges from the medium. One major application of imaging through highly scattering media is in the area of diagnostic and routine medical imaging of tissues. The challenge presented to OT is due to the overwhelming proportion of light that is scattered along a random trajectory in a highly scattering medium. Because this scattered light traverses a random path through the medium and can exit the medium at any given position or angle, it produces a blurry image with the contents of the medium obscured from view. Thus, OT techniques must resolve an intelligible image of the scattering medium amidst extremely high levels of randomly scattered light.

The following subsections describe the transmission and scattering theory for light traveling through a scattering medium, along with current OT methods in use by researchers.

1.1.1 Photon transmission and scattering theory

When light enters a scattering medium, its trajectory can be affected in many ways, several of which are illustrated in Figure 1-1.

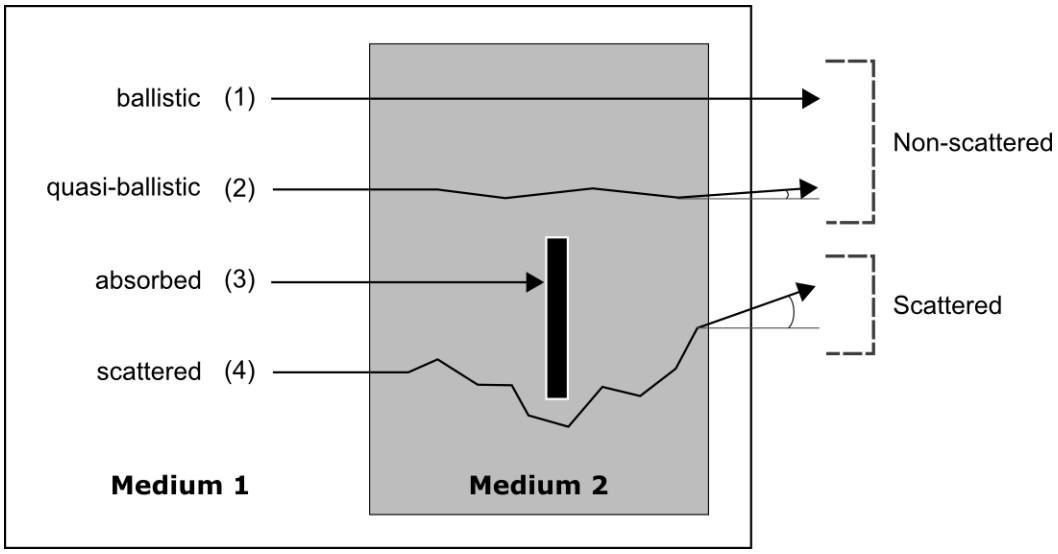

Figure 1-1 Photon transmission from one medium through another scattering medium.

Figure 1-1 presents four significant cases for a photon entering and traveling through a scattering medium. The first case describes a photon that travels through the medium with absolutely no scattering. This photon is termed a *ballistic photon* (1) because it travels straight through the medium along its original trajectory. The second case is similar to the ballistic case, except the photon undergoes a minimal amount of scattering that does not significantly alter the photon's path through the medium nor its exit angle. This photon is termed *quasi-ballistic* (2) because of its similar characteristics to the ballistic photon. Both ballistic and quasi-ballistic photons are useful in OT imaging methods because they contain information about the internal structure of the scattering medium. Thus, an intelligible image can be resolved from the ballistic and quasi-ballistic light that is projected through the medium. In this thesis, both ballistic and quasi-ballistic light are referred to as non-scattered light.

A third case that is described is a photon that is absorbed by some constituent of the scattering medium. This *absorbed photon* (3) ceases to travel through the medium and is never detected by the image sensor. Finally, the fourth case describes a photon that is scattered along a random, walk-like path through the medium. This *scattered photon* (4) is not useful for most OT imaging methods (except for Diffuse Optical Tomography,

introduced in *Section 1.2.4*) because it does not follow an easily determined path through the medium, and can exit the medium at any location and with any angle.

Most OT methods extract an image from the non-scattered light that emerges from a scattering medium, while rejecting the scattered light. Ballistic and quasi-ballistic photons bear useful imaging information because they travel through a straight and known path through the medium, with opaque structures casting a shadow. Thus, if an entire area of a scattering medium is illuminated with collimated light, a two-dimensional projection image of the medium can be resolved from the ballistic and quasi-ballistic light that is collected (see Figure 1-2). Scattered light must be rejected in this technique because they traverse the medium along a random path, and thus constitute noise that interferes with the projected image signal.

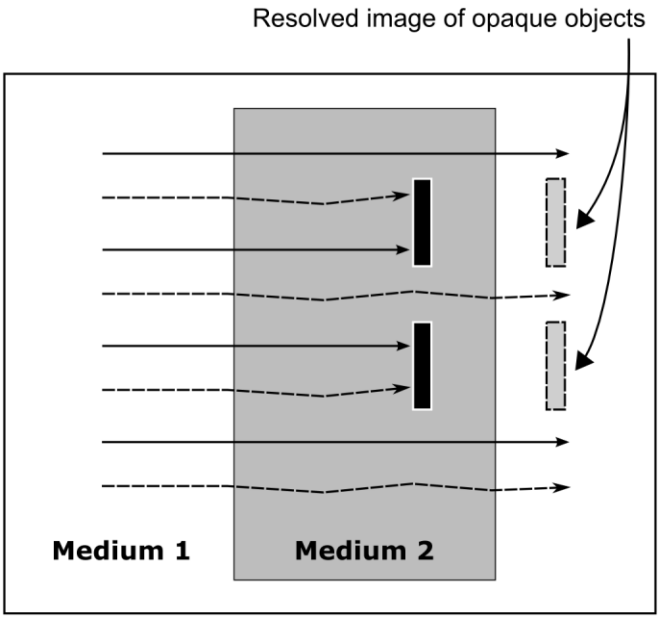

Figure 1-2 Extracting a 2-D projection image using ballistic, quasi-ballistic, and absorbed light photons.

Highly scattering media are characterized by extremely high levels of scattered light photons in comparison to the non-scattered (ballistic and quasi-ballistic) photons. In this thesis, this ratio is referred to as the Scattering Ratio (SR) of the scattering medium. The difficulty in imaging such highly scattering media is that scattered photons typically experience a high number of scattering events and traverse a random walk-like trajectory through the medium [10]. In OT techniques where scattered light must be rejected in

favor of non-scattered light, the former can be considered imaging noise with the latter being the signal. Thus, for highly scattering media, successful OT techniques must overcome extremely low signal-to-noise ratios in order to resolve an intelligible image.

1.1.2 Optical scattering mathematics

The behavior of photons that travel through a scattering medium can be modeled mathematically. As a simple approximation, the Beer-Lambert law shows that the intensity of a collimated beam of light I_{in} traversing a scattering medium is reduced to an intensity I_{out} for a given longitudinal depth d according to the following expression,

$$I_{out} = I_{in} \cdot e^{-(\mu_a + \mu_s)d}, \qquad \textbf{Equation 1-1}$$

where μ_a is the absorption coefficient and μ_s is the scattering coefficient for the medium [3]. Because the Beer-Lambert law is an exponential function, then if the absorption coefficient is much smaller than the scattering coefficient, the scattering effect will significantly dominate. In many biological tissues and media, such as human breast tissue or dilute milk solutions [3], the scattering coefficient, μ_s, is over 100 times higher than the absorption coefficient μ_a. Furthermore, any differences in magnitude between the scattering and absorption coefficients will be exponentially amplified as the depth of the scattering medium, L, is increased.

1.1.2.1 Anisotropic scattering in a medium

When light scatters in a medium, the scattered photons can either be distributed uniformly across all angles (isotropically) or non-uniformly (anisotropically). The anisotropy factor, g, is a dimensionless value that gives a measure of the degree to which scattering in a medium is "forward-directed". For a single scattering event, photons are scattered at an angle θ relative to the original photon path, and φ rotated about that path. It is defined as the mean of the cosine of the scattering angle, θ, which is illustrated in Figure 1-3 and described by the following expression,

$$g = \langle \cos\theta \rangle = \int_0^{\pi} p(\theta)\cos(\theta)2\pi\sin(\theta)d\theta, \qquad \textbf{Equation 1-2}$$

where $p(\theta)$ is the phase function distribution representing scattering angle probability with the rotational angle φ held constant.

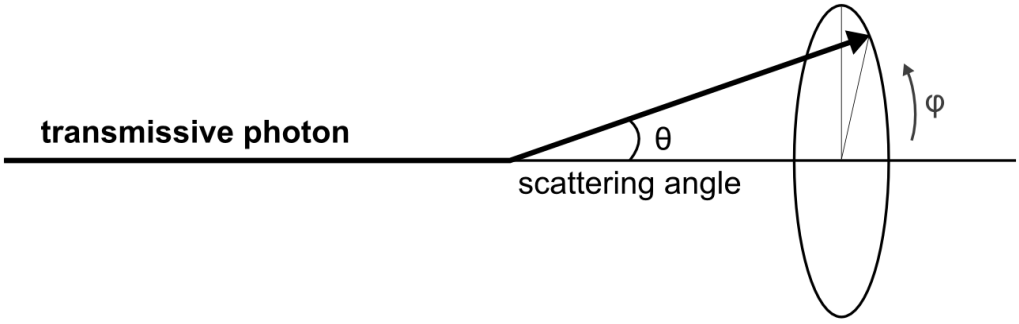

Figure 1-3 Illustration of the scattering angle for a photon in a scattering medium.

For fully forward scattering (i.e. θ = 0°), g = 1, which means that photons do not scatter in angle at all, but travel perfectly straight through the medium. For g slightly less than 1, photons that encounter a scattering event will change trajectory by, on average, a small angle θ slightly greater than 0°. Thus, scattering media with g values close to 1 are referred to as highly forward scattering media.

For fully backwards scattering/reflection (i.e. θ = 180°), g = -1, which indicates that all photons that encounter a scattering event reflect backwards along its original trajectory. For the isotropic, or uniformly distributed scattering case, g = 0 (i.e. mean θ = 90°). In such a scattering medium, scattered photons have an equal chance of scattering from 0° to 180°, and thus, the mean scattering angle, θ, is 90°.

In many scattering media, such as biological tissue, light does not scatter uniformly but is highly anisotropic. For light in the red and near-infrared (NIR) wavelengths, tissue is highly forward scattering, with typical anisotropy values of g = 0.8 to 0.95 [11]. For example, both healthy and diseased breast tissue samples have been measured to have anisotropy values of g = 0.945 to 0.985 [12].

Jacques showed that scattering in many materials (including biological tissue) follows the Henyey-Greenstein function which describes a scattering probability phase function as follows [13],

$$p(\theta) = \frac{1}{4\pi} \frac{1-g^2}{\left[1+g^2-2g\cos(\theta)\right]^{3/2}}. \qquad \textbf{Equation 1-3}$$

The following figure illustrates the effect that the anisotropy factor *g* has on the scattering angle distribution *p(θ)*.

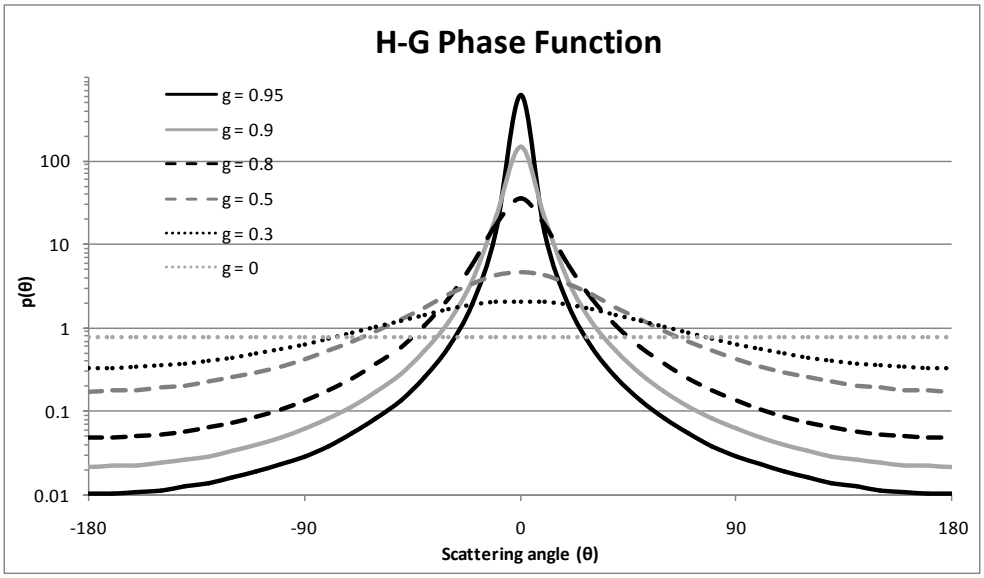

Figure 1-4 Henyey-Greenstein scattering phase distribution for various *g* factors.

As is clearly evident from Figure 1-4, high *g* factors close to 1 lead to a very pronounced forward scattering behviour, and thus, much lower effective scattering levels.

1.1.2.2 Reduced scattering coefficient

As a first approximation, the anisotropy factor of a scattering medium can be taken into account to yield a reduced scattering coefficient, μ_s', that can be expressed as follows [14]:

$$\mu_s' = \mu_s(1-g)[\mathrm{cm}^{-1}]. \qquad \textbf{Equation 1-4}$$

With typical anisotropy values ranging from 0.8 to as high as 0.985, the reduced scattering coefficient can be one to two orders of magnitude smaller than the original scattering coefficient. Another related measure of scattering is the Mean Free Path (MFP) of a medium, which describes the average path length that a photon travels in the medium before encountering a scattering event. Short MFP values correspond to highly scattering media, while a non-scattering medium will have a MFP approaching infinity. MFP is equivalent to the inverse of the scattering coefficient (as shown in Equation 1-5), and thus is increased significantly as the scattering coefficient of a medium is reduced.

$$MFP = \frac{1}{\mu_s'} \text{ [cm]} \qquad \textbf{Equation 1-5}$$

Human breast tissue has been measured in one study [15] to have a μ_s' value of approx. 4.2 cm^{-1} for a thickness of 5 cm with 670nm light, though μ_s' was found to scale with thickness. Ensemble averages over several subjects yielded values of μ_a = 0.041 cm^{-1} and μ_s' = 11.7 cm^{-1} at 670 nm. It should be noted that reduced scattering coefficients are known to depend inversely linearly with wavelength, so for wavelengths shorter than 670 nm for example, the μ_s' value will be greater [15].

From the Beer-Lambert Law given previously (see Equation 1-1), we can derive the probability of a photon traveling through a medium of thickness, *d*, without being absorbed (T_a) or scattered (T_s), to be

$$T_a = e^{-\mu_a d} \text{ and } T_s = e^{-\mu_s' d}, \qquad \textbf{Equations 1-6, 1-7}$$

respectively. Thus, the total scattering probability, *TSP*, is given by the expression,

$$TSP = 1 - T_s. \qquad \textbf{Equation 1-8}$$

A metric used in this thesis to describe the scattering level of a medium is termed the Scattering Ratio, *SR*, which is defined as the number of photons that are scattered for every non-scattered photon that passes through the medium. For a given T_s value of a specific scattering medium, the SR value is given as,

$$SR = \frac{\text{proportion of scattered photons}}{\text{proportion of non-scattered photons}} = \frac{1 - T_s}{T_s}, \qquad \textbf{Equation 1-9}$$

where "non-scattered" photons are defined to include both ballistic and quasi-ballistic photons. When T_s is $< \frac{1}{20}$, SR is approximately equal to $\frac{1}{T_s}$.

For OT in a scattering media, uniform levels of absorption generally do not hinder imaging, because they do not act as random noise in the image and are typically orders of magnitude lower than scattering levels. Thus, the SR value, not the level of absorption, serves as the metric of interest when evaluating the imaging performance of an OT technique for a scattering medium.

For the previously given mammography example, a μ_s' value of 4.2 cm^{-1} with d = 5 cm would correspond to a scattering ratio of $SR = 1.3 \times 10^9$:1, which corresponds to the ratio between scattered photons for every one ballistic or *quasi-ballistic* photon. Quasi-ballistic photons, which are those photons scattered forward off its original trajectory by a very small angle, are included in this measure because the reduced scattering coefficient is used in calculating the *SR*.

For higher depth or μ_s' samples, the *SR* will increase exponentially. *SR* values on the order of 10^{11}:1 have been mentioned in the literature as a significant target for Optical Tomography research [3].

1.2 Current methods in OT

Several OT techniques are being explored for extracting an image from a highly scattering medium. Time Domain (TD) and Optical Coherence Tomography (OCT) both discriminate between scattered and non-scattered photons based on their path length through the medium. Diffuse Optical Tomography (DOT) gathers light data from various points around the medium and then uses a mathematical model to transform that data into

an intelligible image of the medium's contents. Angular Domain Imaging (ADI) discriminates between scattered and non-scattered photons based on their trajectory and exit angle from the medium. These techniques are introduced and discussed in the following subsections.

1.2.1 Time Domain OT

Time Domain Optical (TD OT) Tomography differentiates between scattered and non-scattered light by assuming that ballistic and quasi-ballistic photons travel straight through the medium and are detected first, while scattered light takes a longer path and is delayed. In TD OT, the scattering sample is illuminated by a very short pulse of light (e.g. a few picoseconds) [16] and a very fast detector or shutter is required to collect photons arriving within a short time interval (e.g. 200 ps) when exiting the medium. As photons pass through the medium, non-scattered and scattered light are separated in time (see Figure 1-5) [17]. Ballistic photons do not encounter any scattering, and are the first to arrive at the detector after traveling through the medium along the shortest, straight path. Quasi-ballistic photons encounter some scattering, but still traverse the medium along a fairly straight path with minimal delay in time. Scattered photons travel with a random walk path through the medium, and thus exit the medium after being significantly delayed in time.

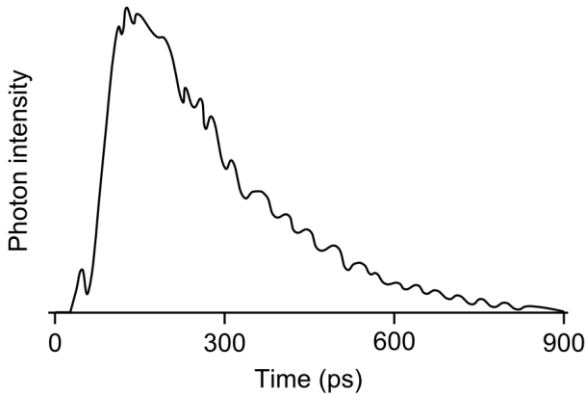

Figure 1-5 Typical photon propagation time course through a scattering medium (after Das et al.) [17].

Ballistic and quasi-ballistic photons are of interest because they bear information regarding the trajectories they have traversed. Scattered photons, however, have an

unknown trajectory through the medium. Thus, TD imaging systems collect the ballistic and quasi-ballistic photons that arrive within a certain delay of the initial illumination pulse in order to construct an image of the medium contents, while scattered photons arriving after that cut-off time are rejected.

TD imaging has several drawbacks, including the requirement for ultrashort pulse sources and time-gated camera detectors (on the order of picoseconds) [17]. These requirements can make TD imaging an expensive endeavour, requiring sensitive and high-performance equipment. In addition, the use of ultrashort laser pulses requires lower optical exposure, as acoustic shockwaves and tissue damage can result even at low energies from such short pulse durations. For safety reasons, the U.S. Food and Drug Administration has not approved any diagnostic TD system using ultrashort laser pulses for commercial use.

TD techniques are currently being explored in areas such as optical mammography (breast tissue) while providing inferior image resolution to x-ray imaging [18]. An example of the performance limitations of TD imaging is given in [10], which specifies a lateral resolution limit of 1 mm in images.

1.2.2 Optical Coherence Tomography

OCT operates by utilizing interference effects to detect ballistic light returned from a sample, which is in phase with a reference beam, versus scattered light that is out of phase with the reference beam. The standard OCT scheme operates by illuminating a sample with light and comparing the back-reflected light from the sample with a reference beam using a Michelson interferometer to produce a depth-resolved image (see Figure 1-6) [11]. Ballistic and quasi-ballistic photons are back-reflected from a certain depth in the sample with zero or little delay, and these add coherently with the reference beam. However, scattered photons from the sample are delayed in time and phase, and thus are incoherent with the reference beam. OCT is similar to acoustic ultrasound imaging and TD imaging techniques in that path length and delay are of primary importance.

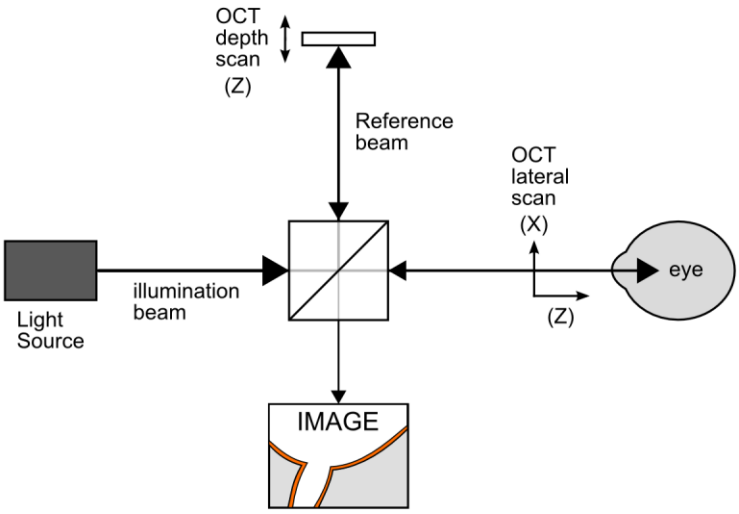

Figure 1-6 Simple illustration of the standard OCT scheme (after Fercher et al.) [11].

OCT can provide very high axial (depth) and transverse (lateral) imaging resolution that is independent of one another [19]. Other advantages of OCT include non-contact and non-invasive imaging of biological tissues. As a result, ophthalmology is a dominant field of application for OCT, while OCT biopsy and functional imaging are also in use [11]. For example, ultra-high resolution ophthalmologic OCT can produce images in the eye with axial and transverse resolutions up to 1 µm and 3 µm, respectively, at depths on the order of 0.5 mm [19]. OCT is capable of imaging at depths of 1 to 2 mm in most tissues (other than the eye) [10] [19]. While capable of providing high-resolution imaging of biological tissues, OCT is limited by its relatively short penetration depth into human tissues.

Ultra-high resolution OCT ophthalmology makes use of ultrafast, ultrabroad-bandwidth, low-coherence light such as a femtosecond Titanium-sapphire pulse laser [19], though such a source is expensive. These source requirements are necessary to provide high resolution and high speed necessary for this kind of OCT imaging.

1.2.3 Confocal Microscopy

Confocal microscopy captures images from within a sample by detecting light originating from a specific focal plane depth in the sample [20]. This light is focussed using an

objective lens through a pinhole aperture located so as to pass light from a desired focal plane (or planes) while rejecting out-of-focus light. In a fluorescent sample, light fluorescing from within the sample can be used to form the image, with out-of-focus "flare" rejected. In direct illumination, focussed beams of light, often from a laser, are used to scan across and illuminate the sample.

Confocal microscopy offers better imaging performance over conventional optical microscopy because of its shallow depth of field, ability to reject out-of-focus glare, and generate three-dimensional images. Because confocal microscopy uses spatial filtering to eliminate out-of-focus light or flare, scattered light will also be rejected.

1.2.4 Diffuse Optical Tomography

DOT operates by using the fact that scattered light still has a small amount of information which can be recovered when multiple source and detector points are used. First, multiple light sources and detectors are used to gather light propagation data from various positions on the sample medium surface. The internal structure is then reconstructed using the light propagation data from the sample under examination to solve for the inverse of a mathematical model constructed for that sample (known as solving the *inverse problem*). This model is tailored specifically for the particular sample, but is based from general mathematical theory for light transport through tissue [16]. DOT is a computationally intensive process and provides limited accuracy and resolution performance.

Areas of exploration for DOT include functional brain imaging, mammography, muscle imaging, imaging of joint inflammation, and molecular or fluorescence imaging [10], [16]. In general, DOT allows for imaging at relatively greater depths in tissue (e.g. 1.5 cm), although spatial resolution is still a challenge (10 mm down to 1 mm) [10]. Thus, imaging depth, spatial resolution, and equipment cost (depending on whether time domain or coherence domain techniques are used) are factors that limit DOT's appeal.

1.2.5 Angular Domain Imaging

Angular Domain Imaging is an OT method that discriminates between scattered light and non-scattered light based on the angle at which light emerges from the scattering medium. Prior research involving Monte Carlo simulation of scattering angle distribution in a highly scattering medium (SR = 10^5:1) demonstrates that photons which emerge from the medium with very small angular deviations also have very small path lengths (see Figure 1-7) [3]. Figure 1-7 indicates that photons with exit angles less than 0.5° have path lengths virtually identical to the minimal path length of ballistic photons. Path length increases significantly as photon exit angle increases. Note that the sharp change in the graph is due to a change in the bin size used in generating the two sets of simulation data presented together in Figure 1-7. Monte Carlo simulations are a computationally intensive process and expand with the scattering level. Thus, a factor of 10 increase in the SR value requires 10 times more scattering calculations. At the same time, because the number of ballistic photons is reduced by a factor of 10, approx. 10 times more photons must be launched to give statistically significant results. Thus, in practice, SR values of 10^4 to 10^5:1 are the current computational limits for a single computer, which is well below the experimental limits of this thesis.

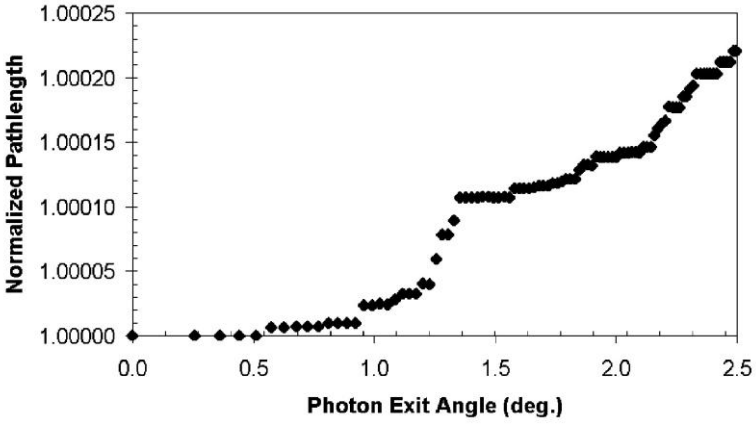

Figure 1-7 Monte Carlo simulation of photon scattering angle distribution in a highly scattering medium (taken with permission from Chapman et al.) [3].

By setting an appropriate and small acceptance angle, ballistic and quasi-ballistic light can be collected at a detector while scattered photons with exit angles outside the acceptance angle are rejected. An image of the scattering medium contents can then be

constructed using the isolated ballistic and quasi-ballistic light. Thus, the key requirement for ADI is to create an angular filter for small detection angles.

Further description of the ADI OT method is given in *Chapter 2* of this thesis.

1.3 Research objectives and scope

This thesis explores research employing an Angular Filter Array device for trans-illumination and deep-illumination ADI. Previous work has utilized a full-frame Argon ion laser for trans-illumination ADI of dilute milk samples. This thesis will introduce new research utilizing a longer wavelength (670 nm) diode laser source for trans-illumination ADI of both dilute milk samples and biological tissue samples. Deep-illumination ADI utilizing the Argon ion laser source is also introduced in this thesis. Finally, a new angular filter, the aperture-based Spatial Filter, is introduced for use with trans-illumination ADI and the Argon laser.

This thesis extends the use of an Angular Filter Array in ADI of highly scattering media, with a goal of improving imaging performance. The effect of changing the illumination source in ADI from an Argon ion (488-514 nm) full-frame laser to a 670 nm laser diode is examined, with a discussion on the multispectral capabilities for ADI. Results and limitations with imaging at the new wavelength for calibrated milk-based scattering solutions and true biological (chicken breast) tissues are discussed.

Modifications to the AFA setup are tested in an effort to enhance imaging results through reducing the AFA tunnel dimensions and scanning step sizes used, in addition to altering the tunnel surface to reduce internal reflections. Spatial filtering is also explored as an alternate ADI method, with results and analysis presented.

1.4 Organisation of thesis content

This first chapter contains an overview of the thesis topic and previous research. It also introduces Optical Tomography scattering theory and current methods for OT imaging.

Chapter two further describes ADI theory, including various ways of employing the AFA to image a scattering medium as well as the spatial filtering method. A discussion on the characteristics and capabilities of ADI is also provided.

Chapter three outlines the experimental apparatus and setup used in the ADI research.

Chapter four outlines the experimental method and procedures undertaken in conducting this research. Special mention to the software programming work required for utilizing a new motion controller and vertical stage is given.

Chapter five summarizes previous AFA ADI research with the Argon ion laser for milk-based scattering solutions. Results at varying Scattering Ratio values and test object depths are presented for both the spherical beam expander and Cylindrical-Spherical-Cylindrical lens beam shaping systems.

Chapter six presents imaging results using the 670nm laser diode for calibrated milk-based scattering solutions and biological chicken breast tissues. Imaging performance and limitations are discussed.

Chapter seven presents ADI results with various modifications to the experiment setup, including modifications to the tunnel walls to reduce reflection and changes to the AFA tunnel dimensions and vertical step sizes used in scanning.

Chapter eight presents aperture-based Spatial Filtering ADI results for calibrated milk-based scattering solutions and compares them with theory. An analysis of imaging performance and trade-offs is given.

Chapter nine contains conclusions and ideas for future work on this research topic.

Chapter 2

Angular Domain Imaging

Angular Domain Imaging (ADI) is a methodology for optical imaging that is based on the angular trajectory of light as it passes through a medium. Other techniques for OT in a scattering medium either operate based on changes in delay or phase through the medium (i.e. path length) or by utilizing mathematical light transport models to reconstruct an image. ADI operates by discriminating between scattered and non-scattered light emerging from a scattering medium based on angle and resolving an image from the non-scattered light that is collected.

This chapter introduces and explains trans-illumination and deep illumination ADI. In addition, the theory and technical background behind the Angular Filter Array (AFA) and Spatial Filter (SF) ADI techniques for discriminating between scattered and non-scattered photons are presented. Finally, illumination source requirements for ADI are discussed, and a summary of the chapter is given.

2.1 ADI theory

Angular Domain Imaging can be categorized into trans-illumination techniques and deep illumination techniques, depending on the location of the source and detector. These two categories are described as follows in the section.

2.1.1 Trans-illumination ADI

In trans-illumination ADI, the scattering sample is illuminated by collimated light from one side. As was noted in chapter one, most of this light is randomly scattered within the medium. Then on the exit side, an angular filter aligned to that collimated source rejects the scattered light and allows ballistic and quasi-ballistic photons that emerge from the sample to be collected by a camera to form an image of the sample and internal structures (see Figure 2-1).

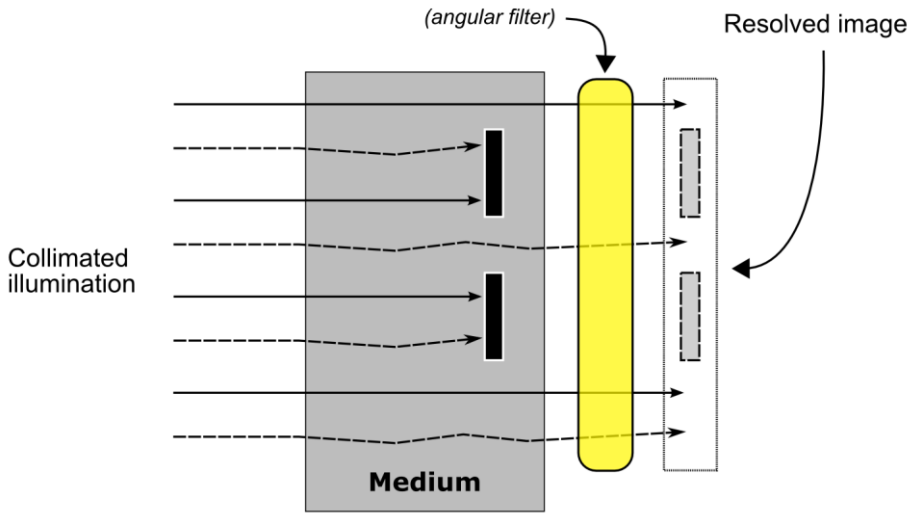

Figure 2-1 Illustration of trans-illumination ADI.

The essence of trans-illumination is that the collimated source and angular filter (shown in Figure 2-1) must be carefully aligned. Previous work in ADI has utilized the trans-illumination technique for imaging a scattering medium [3], [4], [5], [6], [7], [8], [9]. Sub-millimetre resolution has been achieved using collimated flood illumination and an AFA device at SR ~ 10^6:1, while SR = 10^8:1 can be reached using a thin horizontal line of light for illuminating the sample [9]. SR = 10^9:1 can be reached with the addition of a 1 mm-wide slit to restrict the horizontal field of illumination. Further work is presented in this thesis in the area of trans-illumination ADI with an AFA device or via Spatial Filtering.

2.1.2 Deep illumination ADI

Unlike trans-illumination ADI, the deep illumination ADI technique does not attempt to capture photons traveling directly from the illumination source. Instead, a light source is generated within the scattering medium, such as by scattered light from a directed beam into the medium or by using a short wavelength source to stimulate a fluorescent material within the medium to create a light source of a separate wavelength. As a result, deep illumination ADI can operate with an illumination source located off to the lateral side of the sample, or even on the same side of the sample as the detector (see Figure 2-2).

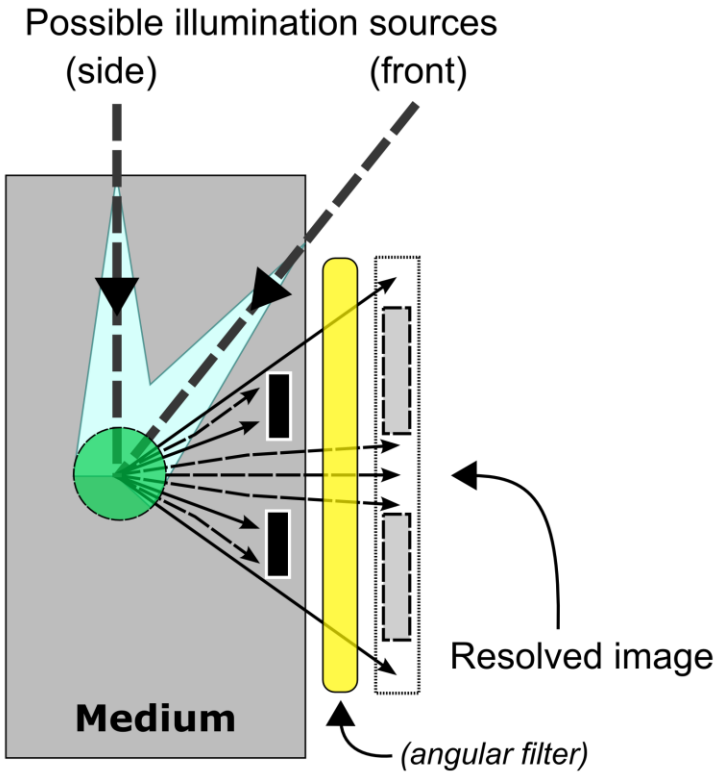

Figure 2-2 Illustration of deep illumination ADI.

As shown in Figure 2-2, a typical deep illumination ADI configuration utilizes a beam of illumination to penetrate the sample and generate a secondary source of illumination within the medium. After many scatterings in the highly scattering medium, the injected light will tend towards emitting light uniformly in all directions, forming what can be termed a "glow ball" [10], shown enlarged as follows in Figure 2-3. A small acceptance angle angular filter is placed at the medium's surface and aligned to a digital imager.

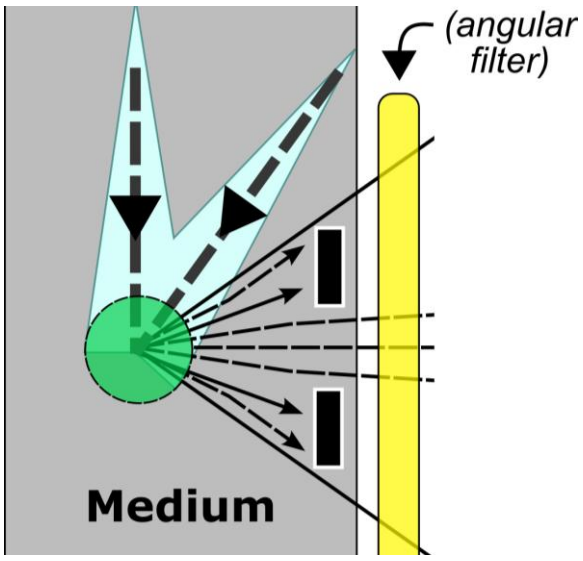

Figure 2-3 Generation of embedded "glow ball" illumination source for deep illumination ADI.

By using a simple collimated illumination beam, the glow ball can be formed up to several centimeters deep within the scattering medium. Because the light emitted by the glow ball is distributed along all angles, a proportion of the emitted light will fall within the ADI acceptance angle and act as a new source of "ballistic" and "quasi-ballistic" photons that pass from the glow ball to the detector. These photons carry information regarding the scattering medium structure between the embedded glow ball and the detector, and thus can be used to resolve an image of that entire region as shown in Figure 2-2 (see "resolved image"). Light that is scattered after leaving the glow ball will be directed into angles that are rejected by the angular filter. Because of the broad angular distribution of emitted light, a far greater proportion of scattered to ballistic light exists for deep illumination ADI, as compared to using a collimated illumination source in trans-illumination. Thus, the much lower initial signal-to-scattered ratio means that deep illumination ADI must image objects at much shallower depths compared to trans-illumination ADI.

Recent work conducted by Fartash Vasefi and the author in deep illumination ADI has introduced and demonstrated this technique for imaging highly scattering media [10], [21]. Sub-millimetre resolution (0.2 mm or better) has been demonstrated at SR = 1.6×10^{10}:1 and 3.7×10^{12}:1 at depths of 3 mm and 2 mm, respectively, and digital

image processing techniques prove effective in enhancing detectability and contrast in such images [10]. However, the focus of this thesis is on trans-illumination ADI techniques and AFA imaging modifications, and thus deep illumination is not discussed in-depth.

2.2 Angular Filter Array ADI

One way to implement angular filtration in ADI is to utilize micro-tunnels (collimators) to physically filter the light (see Figure 2-4). Light that arrives within the acceptance angle of the tunnels will be allowed to pass through unattenuated and reach a detector placed immediately after the AFA. However, scattered light with angles beyond the acceptance angle will strike the sidewalls of the tunnels and become attenuated before reaching the detector. As a result, an image can be produced using the collected ballistic and quasi-ballistic light, while scattered light outside the acceptance angle is rejected by the AFA.

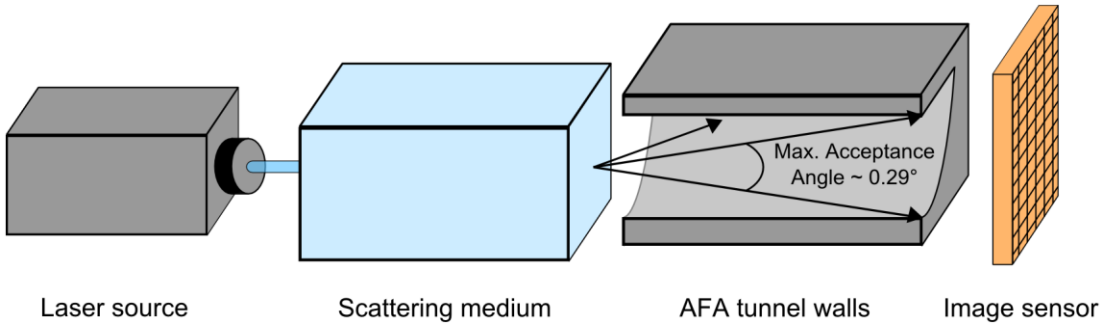

Figure 2-4 Maximum acceptance angle diagram for a single AFA tunnel.

The following subsections describe the design, fabrication, and challenges associated with the AFA device.

2.2.1 AFA design

The Angular Filter Array (AFA) consists of a linear, parallel array of channels micromachined into a flat silicon substrate, illustrated as follows in Figure 2-5.

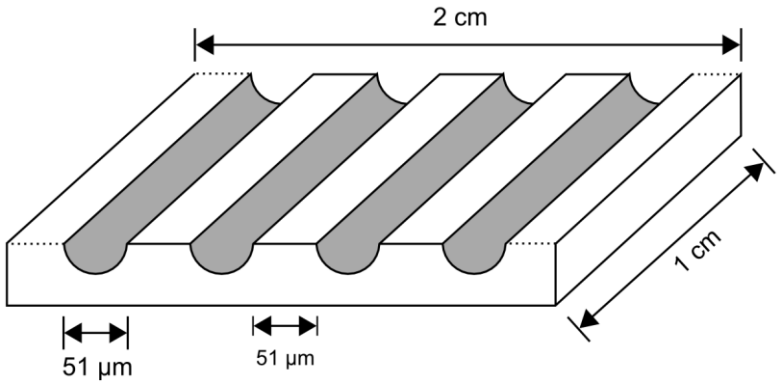

Figure 2-5 Diagram of the Angular Filter Array.

As designed in previous work at Simon Fraser University (SFU), each tunnel is semi-circular in shape with 51 µm width and 1 cm length, spaced 102 µm apart, yielding an aspect ratio of 196:1 [3]. In fabrication, the height of the tunnel is approximately 15 µm. This gives each tunnel a maximum acceptance angle of 0.29º along the horizontal axis, and approximately one third that along the vertical axis (see Figure 2-4).

2.2.2 AFA fabrication

The AFA device is produced using bulk micromachining techniques on a silicon wafer. Several AFA devices have been produced by the author at SFU in a Class 100 clean room (School of Engineering Science). The microfabrication process is illustrated as follows in Figure 2-4.

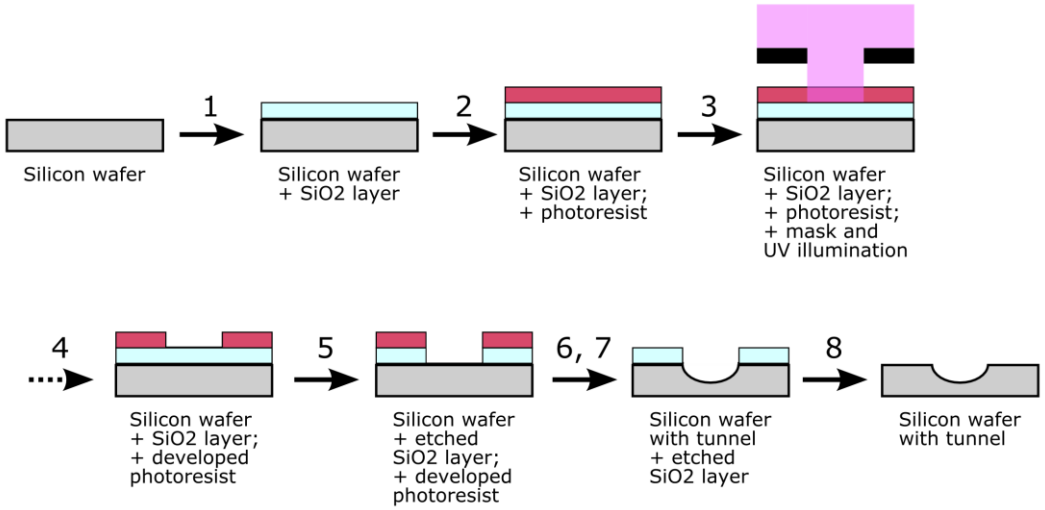

Figure 2-6 Illustration of Angular Filter Array microfabrication process.

In this process, a thin oxide (SiO_2) layer is first grown on the silicon wafer in a high temperature furnace (1), and a thin organic photoresist layer is then spun onto the wafer (2). Using a chrome mask bearing a design pattern that roughly resembles the tunnel structures in the AFA (see Figure 2-7), that pattern is transferred from the chrome mask onto the photoresist layer using an ultraviolet light exposure system (3) and a chemical developer solution (4). The photoresist layer that has been patterned is then used as a mask to chemically etch the underlying oxide (5), thus transferring the pattern into the oxide layer. In turn, after stripping the photoresist layer (6), the patterned oxide can be used as a mask for chemically etching the underlying silicon (7), thus transferring the pattern into the silicon wafer. The oxide layer can then be stripped from the wafer (8). The final result is a pattern produced in the silicon comprised of semi-circular tunnels in linear arrays, as illustrated in Figure 2-7. The silicon wafer can then be diced and sectioned to produce individual AFA sections. A flat top piece, from an unetched silicon wafer (unpolished), then covers the etched bottom section creating semi-circular tunnels.

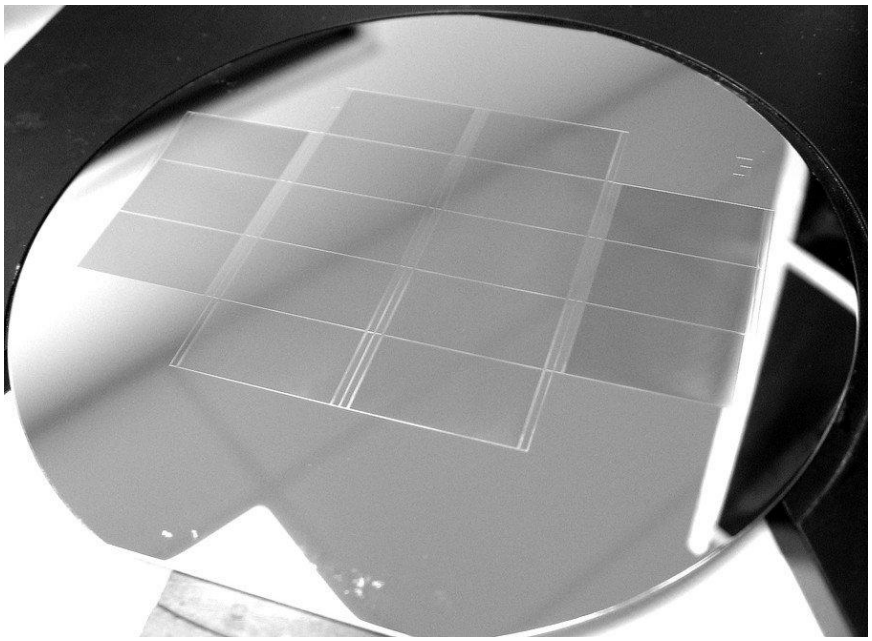

Figure 2-7 Silicon wafer with etched AFA device patterns for photolithography.

More detailed descriptions of the micromachining process are given by Tank [4] and Trinh [6].

2.2.3 AFA ADI challenges

Challenges with the AFA ADI technique exist. One such challenge results from the one-dimensional linear nature of the AFA, which only allows for one horizontal section to be imaged at a given time by the sensor (as illustrated in Figure 2-8). Typically, this horizontal section captured by the sensor is 10 pixels (i.e. 52 µm) tall, and so the sample must be raised incrementally and scanned at different positions before the entire sample can be imaged. By taking each of the captured line images and stacking them one on top of another, a full 2-D image of the sample can be assembled. Because of this process, instead of being able to capture a full image in one quick exposure, the image capture time with the AFA is the total of all exposure times for each line image. Slow image capture times are a liability when imaging living tissues, because they can lead to blurring due to movement or a failure to capture an accurate image of the sample due to changing conditions within the sample. A potential solution to the acquisition time challenge is the construction of a fully two-dimensional AFA that allows for a full 2-D region to be imaged with one exposure, instead of only one line at a time.

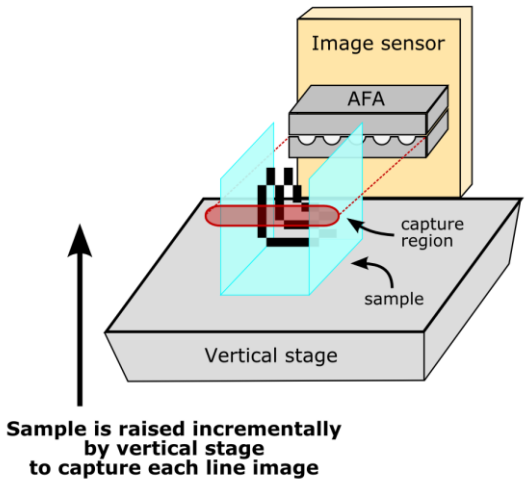

Figure 2-8 Illustration of line-by-line scanning procedure for AFA ADI.

Another challenge with the AFA is due to the partially reflective nature of the silicon tunnel sidewalls. Ideally, scattered light that collides with tunnel sidewalls would be fully absorbed and prevented from passing through the tunnel and reaching the detector. However, silicon (index of refraction, n = 1.5) can be up to 40% reflective to

perpendicular light, and much more so at shallower angles. Using the Fresnel reflection formulae for reflection of angled light, the reflectances R_p (for parallel polarized light) and R_s (perpendicular) are given by,

$$R_p = \left[\frac{\tan(\theta_1 - \theta_2)}{\tan(\theta_1 + \theta_2)}\right]^2 \text{ and } R_s = \left[\frac{\sin(\theta_1 - \theta_2)}{\sin(\theta_1 + \theta_2)}\right]^2, \qquad \textbf{Equation 2-1}$$

where θ_1 is the incoming angle of the ray of light and θ_2 is the angle at which the ray would be refracted if it entered the silicon (with respect to the normal vector). For light rays shallow to the tunnel walls, θ_1 is close to 90°. Since the *sine* and *tangent* functions are symmetric, then for shallow light rays, reflectance approaches unity. For example, light that arrives at the acceptance angle of 0.29° (i.e. 89.71° relative to the normal) gives reflectance values of 92.5% - 99.4% for silicon, depending on polarization and the wavelength of light.

Thus, instead of being fully attenuated, scattered light that collides with the tunnel sidewall can be reflected within the tunnel and reach the detector, where it combines with non-scattered light in forming the image. This scattered light acts as a source of noise in the image, and various techniques can be employed to modify the tunnel sidewall surface in order to suppress it. These techniques will be introduced in *Section 7.1 – Surface-Roughened Angular Filter Arrays*.

A third challenge resulting from the AFA tunnels is due to their small dimensions. While smaller tunnel widths produce stricter acceptance angles and can improve the theoretical spatial resolution of the AFA, a side-effect of small tunnel dimensions is the diffraction of light that passes near the edges of the tunnel. Diffraction occurs when light passes near to edges, and results in the angular spreading of light. Thus, light can be redirected off its original path by diffraction and be imaged by the detector in other regions, which can blur or confuse parts of the image.

The scattered light proportion during imaging is dependent on the field of illumination of the sample. That is, higher scattered background levels are observed during imaging

when the entire sample is being imaged, versus when the illumination region is restricted to a line of light that encompasses the AFA region only. Figure 2-9, shown as follows, illustrates how scattered light can be generated unnecessarily in the sample.

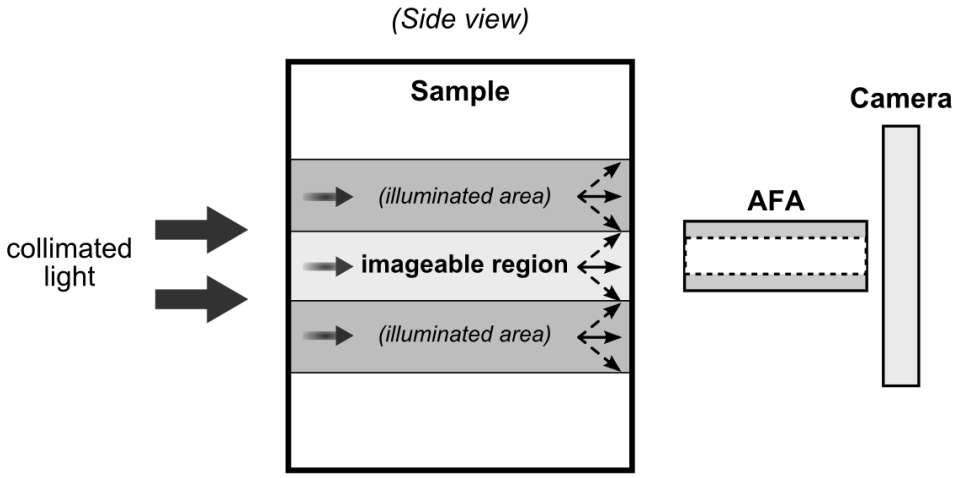

Figure 2-9 Illustration of the generation of scattered light in non-imageable regions of the sample.

As shown above, light from regions of the sample that are not being imaged can still generate scattered light that will reach the AFA and sensor as background scattered light. Thus, by reducing the amount of unnecessary illumination of the sample, the scattered noise level can be decreased during imaging. This principle can be applied to AFA ADI and also to Spatial Filter ADI, which is introduced in the following subsection.

2.3 Aperture-based Spatial Filter ADI

As an alternative to utilizing a collimating microtunnel array, an angular filter can be implemented using a converging lens and aperture to limit the acceptance angle. This produces a spatiofrequency angular filtration device – or more simply described, a Spatial Filter (SF) [22] – composed of only passive optical elements, and also has the advantage of being a full-frame ADI technique capable of capturing an entire 2-D image at once.

The optical physics derivation for operating a Spatial Filter using ADI methodology was derived by Nick Pfeiffer (in a previous paper) with the formulae and theory summarized

in the following subsections [22]. The focus of this thesis will be on the experimental validation of this predicted SF ADI theory.

2.3.1 Spatial Filter ADI design and geometry

When illuminating a scattering sample with collimated light, a converging lens can be placed after the sample to focus ballistic and quasi-ballistic photons through a pinhole aperture located at the back focal point. A camera detector can then be placed a specific image distance away from the aperture to capture an image, as shown in Figure 2-10.

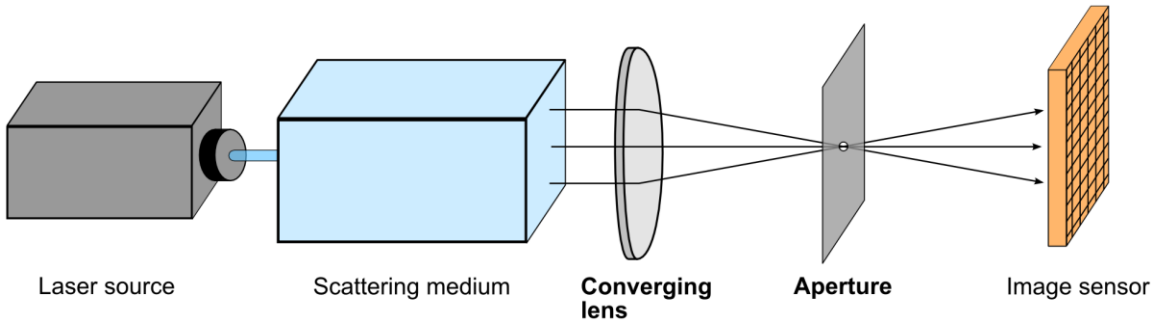

Figure 2-10 Aperture-based Spatial Filter ADI setup.

When a baffle with an aperture of diameter d_a is placed at the back focal point of a converging lens, light arriving at the lens parallel to the optical axis will be focussed through the aperture at the focal point, while light with a slight angular deviation will arrive at the aperture at a given distance away from the optical axis [22]. First, thin lens and small angle approximations will be assumed in this discussion of simple geometric optics formulations.

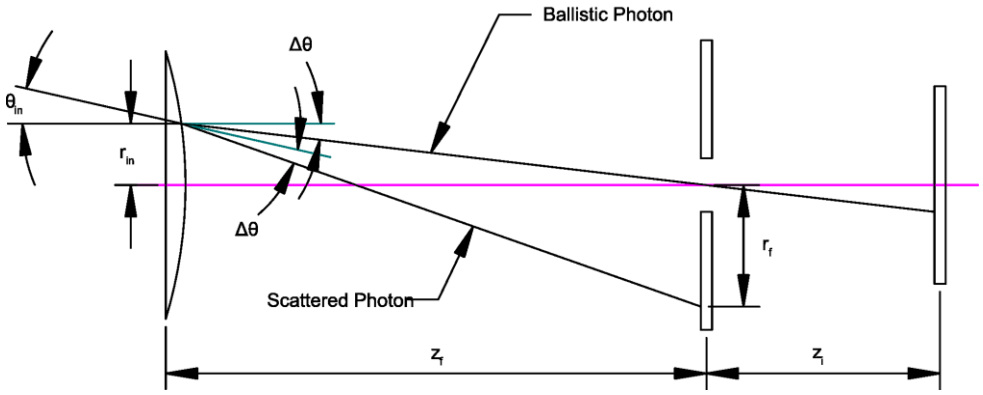

Figure 2-11 Angular redirection of photons towards an aperture by a converging thin lens.

As illustrated in Figure 2-11, a converging thin lens with focal length z_f will cause an input ray to the lens arriving at a distance r_{in} from the optical axis and with angular trajectory θ_{in} to bend by an amount $\Delta\theta$ when exiting the lens, where

$$\Delta\theta = \frac{r_{in}}{z_f}. \qquad \textbf{Equation 2-2}$$

A ray that is passing through the converging lens will cross the focal plane at a radial distance r_f from the optical axis, as expressed by

$$r_f = r_{in} + z_f\left(\theta_{in} - \Delta\theta\right) = \theta_{in} z_f. \qquad \textbf{Equation 2-3}$$

From Equation 2-3, we can see that all rays that arrive at the lens with the same small angle θ_{in} will be mapped to the same radial distance r_f at the aperture. Now consider a scattering medium illuminated with a collimated light source (as in Figure 2-10). All ballistic photons (i.e. rays with $\theta_{in} = 0$) will be focused through the center of the aperture at the back focal point of the converging lens (i.e. $r_f = 0$), while quasi-ballistic and scattered photons with a non-zero θ_{in} will be mapped a certain radial distance r_f away from the focal point. For an aperture with given radius d_a, then all photons mapped to a radial distance r_f that is greater than $d_a/2$ will be blocked and fail to pass through the aperture. Thus, a maximum acceptance angle θ_a is formed by the spatial filter with a relationship between the converging lens and the fixed aperture, and can be determined as follows,

$$\theta_a = \frac{2r_f}{z_f} = \frac{d_a}{z_f}. \qquad \textbf{Equation 2-4}$$

A cross-sectional view of the angular acceptance angle cone formed by the SF is shown as follows in Figure 2-12. Under small angle approximations, the acceptance angle θ_a is constant across all input locations r_{in} for a thin lens [22].

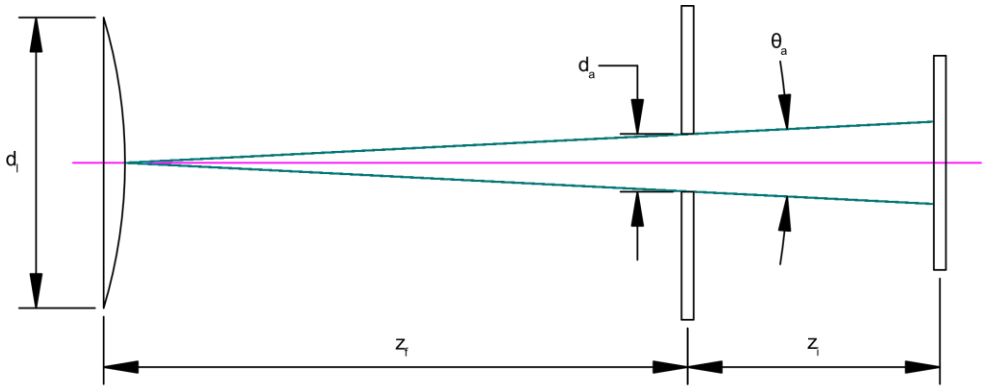

Figure 2-12 Acceptance angle of the aperture-based Spatial Filter.

The final element in the SF is the image sensor, which is placed at an image distance z_i from the aperture (see Figure 2-12). This gives a magnification M of the original image (inverted), as described by

$$M = \left| -\frac{z_i}{z_f} \right| . \qquad \textbf{Equation 2-5}$$

The light intensity I_i of the image is amplified for $M < 1$ (shrinking) or attenuated for $M > 1$ (enlargement) in accordance with the squared relation

$$I_i = \frac{I_{in}}{M^2} . \qquad \textbf{Equation 2-6}$$

The equations in this section describe two desirable characteristics of the SF ADI setup. The first, and most important, is the angular filtration provided by the SF, which allows for the rejection of scattered photons with trajectory angles greater than θ_a. The second is the ability to increase the image intensity at the image plane by bringing the camera closer to the aperture (i.e. reducing the magnification).

2.3.2 Fourier optics

Now consider the application of Fourier optics to this system [23]. Fourier optics applies Fourier spectral analysis to the wave nature of light in optical systems to estimate the effect on the final image of the system. Assuming linear and shift invariance, the aperture-based SF ADI system forms a spatiofrequency filter according to Fourier optics

principles [22]. At the converging lens, the image input wave undergoes a two-dimensional spatial Fourier transform with high spatial frequency components mapped far away from the optical axis at the back focal plane, and low spatial frequencies mapped close to the optical axis. For an image comprised of line pairs with spatial period p, the spatial frequency f is related to the spatial resolution Δr of the image according to the relation

$$\Delta r = \frac{p}{2} = \frac{1}{2f}. \qquad \textbf{Equation 2-7}$$

With the aperture centered on the optical axis at the back focal plane, spatial frequencies higher than a particular cutoff frequency f_0 will be blocked by the aperture, while spatial frequencies less than f_0 will be allowed to pass through the aperture. As a result, the lens and aperture act as a low-pass filter that imposes a limit to the minimum resolution (i.e. highest frequency) feature that can be resolved.

2.3.3 Limiting factors to resolution

There are four factors that limit image resolution in the SF ADI system: the converging lens, the image sensor, the aperture, and the trajectory filtering (acceptance angle) of the system.

2.3.3.1 Resolution limit due to lens

Because the converging lens has a finite diameter, it acts as an aperture which creates a point spread function in the image plane due to diffraction. Using the Rayleigh criterion for diffraction-limited resolution, the imageable resolution of an object $\Delta r_{o,j}$ due to the lens can be estimated to be

$$\Delta r_{o,j} = \frac{1.22\lambda\left(z_f + z_i\right)}{d_l}. \qquad \textbf{Equation 2-8}$$

However, for a typical converging lens with a diameter (d_l) of 25 mm, focal length (z_f) of 50 mm, an image distance (z_i) of 50 mm (i.e. magnification of 1), and a wavelength (λ) of 514 nm, the minimum diffraction-limited resolution is < 3 μm [22].

2.3.3.2 Resolution limit due to image sensor

For a Charge-Coupled Device (CCD) or Complimentary Metal-Oxide-Semiconductor (CMOS) image sensor, the Nyquist theorem indicates that the image must be sampled at at least twice the maximum spatial frequency in the original image in order to resolve the smallest feature. As a result, the pixel pitch of the image sensor must be half the size or smaller than that feature. The CMOS image sensor used in this thesis research has square pixel dimensions of 5.2 µm x 5.2 µm, resulting in a minimum detectable object size of 2 × 5.2 µm = 10.4 µm according to the Nyquist theorem.

2.3.3.3 Resolution limit due to aperture

As explained previously in *Section 2.3.2* on Fourier optics, the aperture acts as a spatiofrequency low-pass filter, which places a limit on the smallest resolvable feature in the image. For a circular aperture with diameter d_a located at the focal length z_f of the lens, the cutoff frequency f_0 is defined as [22]

$$f_0 = \frac{d_a}{2\lambda z_f}. \qquad \textbf{Equation 2-9}$$

Thus, using the relation from Equation 2-7, the minimum resolution error in the object due to the aperture is given by

$$\Delta r_{o,a} = \frac{\lambda z_f}{d_a}, \qquad \textbf{Equation 2-10}$$

which predicts that the object resolution worsens (i.e. the smallest detectable object size increases) due to the aperture and lens as the focal length z_f increases or the aperture diameter d_a decreases.

2.3.3.4 Resolution limit due to trajectory filtering

The first three resolution limits outlined apply for the ballistic photon case. However, the resolution limit imposed by the trajectory filtering of scattered and quasi-ballistic photons from the acceptance angle of the SF must also be considered. For a point lying on the optical axis where it intersects with the image plane, a trajectory can be projected backwards through the aperture and onto the exit face of the scattering sample. For a

photon originating from the exit face on the optical axis, the error in position at the image plane is zero. However, there exists an entire circular region on the exit face that can be seen through the aperture from the point lying on the optical axis at the image plane. The maximum spatial error at the exit plane is defined to be the object resolution error due to trajectory filtering $\Delta r_{o,t}$ according to

$$\Delta r_{o,t} \approx \frac{\theta_a}{2}\left(z_f + z_i\right) = \frac{d_a}{2}\left(\frac{1}{M} + 1\right), \qquad \textbf{Equation 2-11}$$

assuming a uniform distribution of quasi-ballistic and scattered photons across the acceptance angle θ_a [22].

Equation 2-11 indicates that the resolution error due to trajectory filtering of quasi-ballistic and scattered light improves (decreases) either as the aperture diameter d_a is decreased or the magnification M (or image distance z_i) is increased.

2.3.4 Optimizing resolution limited trade-offs

As a first approximation, the best achievable object resolution Δr_o is the worst (largest) of the four calculated resolution limits. *Section 2.3.3* specifies resolution limits due to the lens (~ 3 μm) and the image sensor (~10.4 μm) that are minimal for typical ADI values in comparison to the limits due to the aperture and trajectory filtering. Thus, under highly scattering conditions, an ideal ADI system is designed such that the resolution limits due to aperture and trajectory filtering are minimized. However, there exists a trade-off between the resolution limit due to the aperture, which is directly proportional to z_f and inversely proportional to d_a, and trajectory filtering, which has the opposite relationship to those variables.

Imaging performance predictions derived from the theory discussed thus far will be confirmed with actual imaging experiments (see *Chapter 8*). In particular, image resolution and contrast will be observed for varying aperture diameters, image magnifications, and converging lens focal lengths. Observed performance trade-offs will also be discussed.

2.4 ADI illumination source requirements

Angular Domain Imaging has several distinctive advantages over other OT imaging techniques. Because ADI operates on the principle of angular discrimination, it has flexible illumination source requirements. Multi-spectral imaging can be performed because ADI can operate largely independently of wavelength, though some systems such as the Spatial Filter may have some wavelength dependence. A single AFA ADI configuration can operate within a wide range of wavelengths simultaneously, provided λ is several times smaller than the microtunnel cross-sectional dimensions (i.e. to avoid diffraction effects). Similarly, SF ADI can operate across many wavelengths, although lens behavior (i.e. index of refraction) has a slight dependency on λ.

In addition, either coherent and incoherent sources can be utilized because the phase of photons is not important in angular domain imaging. Full-frame and diode lasers, and even non-laser illumination sources, can be employed because the beam characteristic requirements are quite lax. Diode lasers typically introduce poor beam characteristics, such as poor collimation and short Rayleigh range, though this thesis demonstrates successful ADI imaging with a diode laser source.

ADI's flexible source requirements open up the possibilities for Optical Tomography applications. Sources can be low-power and low-footprint, which enables portable applications. Simultaneous imaging at multiple wavelengths can yield additional information not possible at only one wavelength. In summary, because ADI is based solely on discriminating between photons based on trajectory angle, it allows for large degree of flexibility on how the imaging is performed.

2.5 Chapter summary

Angular Domain Imaging is an optical imaging method that rejects scattered light and accepts non-scattered light based on angle. ADI theory and background were introduced in this chapter, including discussion on Angular Filter Array and aperture-based Spatial Filter design and operation.

Trans-illumination is an ADI method where a collimated light source illuminates the scattering sample, with a carefully aligned angular filter on the opposite side. Deep illumination ADI instead uses a light source generated within the scattering medium, and does not require the angular filter to be aligned to a collimated source.

Angular Filter Array operation, design, and fabrication processes were outlined. AFA tunnels form an acceptance angle that restricts scattered light from reaching the image sensor. The AFA consists of parallel channels micromachined into silicon with an unpolished cover plate.

ADI using Spatial Filtering with a converging lens and aperture was introduced. A thorough description and analysis involving geometric and Fourier optics, as derived by Nick Pfeiffer, was presented. Limiting factors and trade-offs for imaging resolution and performance due to aperture diameter, image distance, and focal length were discussed.

Angular Domain Imaging with the AFA or SF have flexible source requirements. ADI operation is largely wavelength independent, which allows for multi-spectral imaging.

The following chapter describes the experimental setup and apparatus used in the ADI research for this thesis.

Chapter 3

Experimental Apparatus and Setup

This chapter describes the experimental setup for trans-illumination ADI with an Angular Filter Array (AFA) and trans-illumination ADI using aperture-based Spatial Filtering (SF). The Argon ion laser and 670 nm laser diode sources are described, along with the beam shaping systems used by each. The Angular Filter Array and SF converging lens and aperture setups are outlined. Also introduced are the scattering sample apparatuses for both milk-based scattering solutions and biological tissue samples, which are used in conjunction with small resolution test structures. Finally, the image sensors and capture software are described.

3.1 General trans-illumination ADI setup

Trans-illumination ADI involves illuminating a scattering sample from one direction and imaging its contents at the exact opposite end. In this configuration, a light source is required to provide collimated illumination to the scattering sample. A beam shaping system can then be used to transform the source beam into a shape more suitable for illuminating the sample, such as a circle or thin line of light. Scattering samples and test objects are utilized in the experiment to test the imaging performance (e.g. contrast and resolution) of the particular AFA or SF ADI system. Finally, an image sensor connected to a computer is used to capture the resultant images. A functional outline of the ADI setup (see Figure 3-1) consists of the following.

1. **Illumination source** – *Argon ion (488-514 nm) laser* or *670 nm laser diode*
2. **Beam expander/shaping system** – *multiple types*
3. Sample container, scattering medium, and test objects
4. Vertical-axis computer-controlled stage and controller *(AFA ADI only)*
5. **Angular filtration system** – *AFA with alignment jig* or *SF system*
6. CMOS image sensor
7. Imaging and capture software (PC)

The following section details the light sources and beam shaping setups employed for the AFA ADI and SF ADI systems.

3.2 Light source and beam shaping ADI setups

Three illumination configurations are employed in the experiments in this thesis. The first two are AFA ADI systems using either an Argon ion laser or 670 nm laser diode, while the third is a SF ADI system based off the Argon ion laser.

3.2.1 Argon ion laser AFA ADI

The general Argon ion laser setup for AFA ADI, as shown in Figure 3-1, consists of the following.

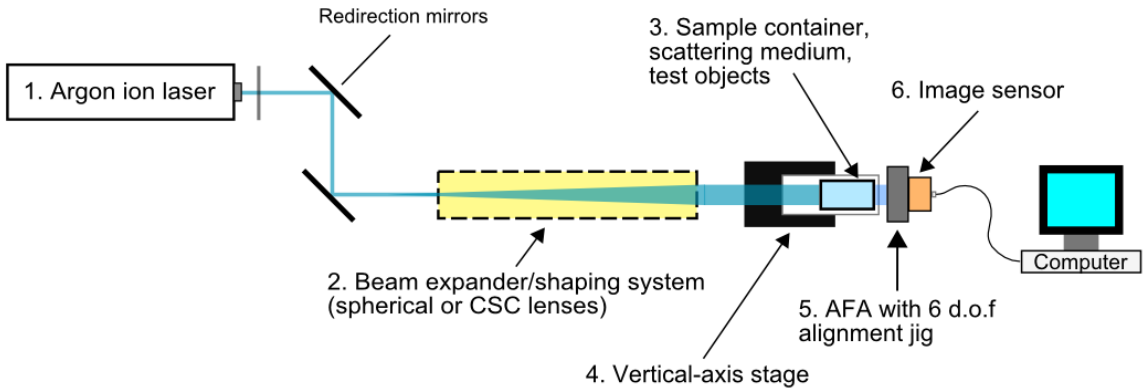

Figure 3-1 Argon ion trans-illumination AFA experiment setup.

3.2.1.1 Argon ion laser

As with most previous ADI work, the first light source used is an Argon ion laser (*Coherent Innova 300 series*) with maximum power output of approximately 5 W (see Figure 3-2). It emits continuous wave light with mainlines of 488 nm and 514 nm, and produces a circular beam of coherent, collimated light with an approx. 2.3 mm beam diameter ($1/e^2$) [21]. The Argon laser provides a beam that is very stable in power and quality with a small angular divergence. However, its short wavelength makes it less than ideal for biological tissue imaging due to increased scattering levels compared to longer wavelengths.

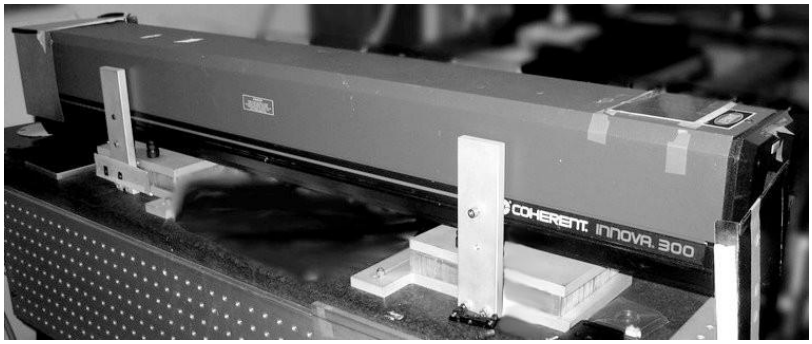

Figure 3-2 Full-frame Argon ion laser.

3.2.1.2 Beam expander/shaping systems

Two different beam expander or shaping systems have been employed with the Argon ion laser AFA setup. The first is a spherical lens Galilean beam expander, which was chosen because it produces a circular, nearly uniform beam that envelops the entire region to be imaged. Expanding the initial beam serves to spread out the Gaussian distribution of the beam, which in turn improves the uniformity of the beam across imageable region of the sample.

The Galilean beam expander was implemented using one diverging lens (f_1 = -25 mm) followed by a converging lens (f_2 = 200 mm) to enlarge the 2.3 mm diameter beam by 8 times, as determined by the focal lengths chosen (see Figure 3-3) [9]. The separation between the two lenses is equal to the sum of the focal lengths, $f_1 + f_2$ = 200 mm. The beam expander produces an expanded beam 2.3 cm in diameter that is used to illuminate the scattering sample.

Figure 3-3 illustrates how the lenses are positioned in a Galilean beam expander.

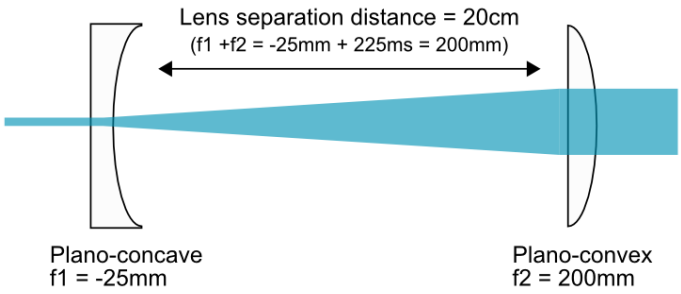

Figure 3-3 Lateral view of the Galilean beam expander lens configuration (8× magnification shown).

As was noted in *Chapter 2*, a thin beam profile is desired to limit the illuminated area of the sample to only the region encompassed by the AFA device, thus reducing the amount of scattered light generated in the sample. By reducing scattered light levels in imaging, the signal-to-noise ratio increases, which improves image contrast. This was achieved using a second beam shaping system: the Cylindrical-Spherical-Cylindrical (CSC) lens beam expander. This beam expander differs from the spherical beam expander in that instead of enlarging the beam equally in both axes, it shapes the beam into a thin light of light that is wider than it is tall.

The CSC beam expander utilizes two cylindrical lenses (f_1 = -19 mm and f_3 = -12.7 mm), with one spherical lens (f_2 = 200 mm) in the middle, to shape the original beam asymmetrically along the horizontal and vertical axes. This produces a thin, lateral beam of illumination as shown in Figure 3-4 and Figure 3-5 [2]. In a typical configuration, this beam shaping system will widen the beam horizontally by 10.53× and then thin the beam by 15.7× vertically, depending on the focal lengths chosen (Figure 3-4). This produces a thin beam approx. 21 mm wide × 0.13 mm tall as depicted in Figure 3-5.

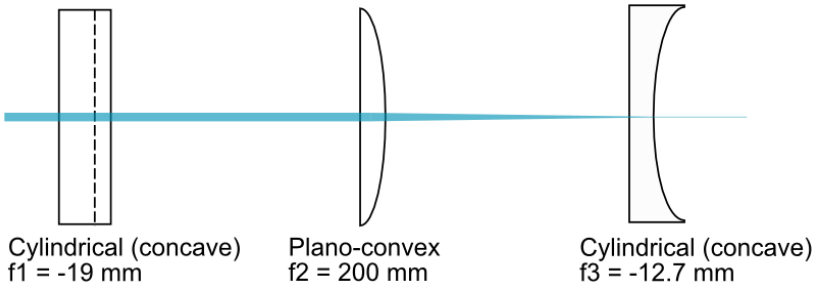

Figure 3-4 Lateral view of an example CSC expander lens configuration.

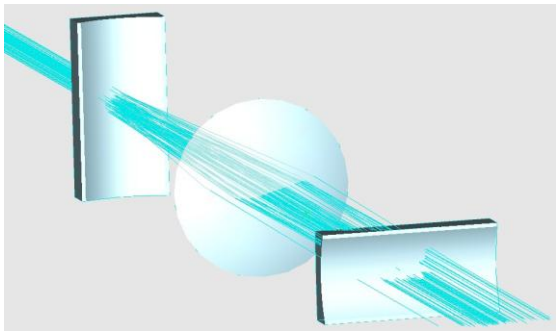

Figure 3-5 Three-dimensional illustration of the CSC beam expander in operation.

One limitation preventing the thinnest possible beam from being produced by the CSC beam expander is described by the Rayleigh range, z_r. A beam's Rayleigh range is a measure of collimation over distance, with a short Rayleigh range corresponding to a beam that diverges at a rapid rate from its origin. Rayleigh range is related to the square of the beam radius in a given axis, and thus, is very sensitive to narrowing of the beam. For a thin beam with 0.13 mm height, $z_r \approx 10.9$ cm, which easily encompasses the working range of our ADI setup (from the end of the beam expander to the image sensor). However, if a beam that is twice as thin is used, then $z_r \approx 2.7$ cm, which is shorter than the length of the sample container alone. Thus, the beam should not be narrowed much further than 0.13 mm in height in order to prevent the illumination beam from diverging in angle.

The CSC beam expander system has been used in previous research and has yielded improved imaging performance under highly scattering conditions because it restricts illumination of the scattering sample to only the imageable region immediately in front of the AFA [2], [9], [24], [25].

3.2.2 Laser diode (670 nm) AFA ADI setup

The 670 nm diode laser AFA setup is very similar to that of the Argon ion laser-based setups, but with a different illumination source and beam shaping system. The 670 nm diode laser AFA setup is outlined as follows, with changes emphasized in italics.

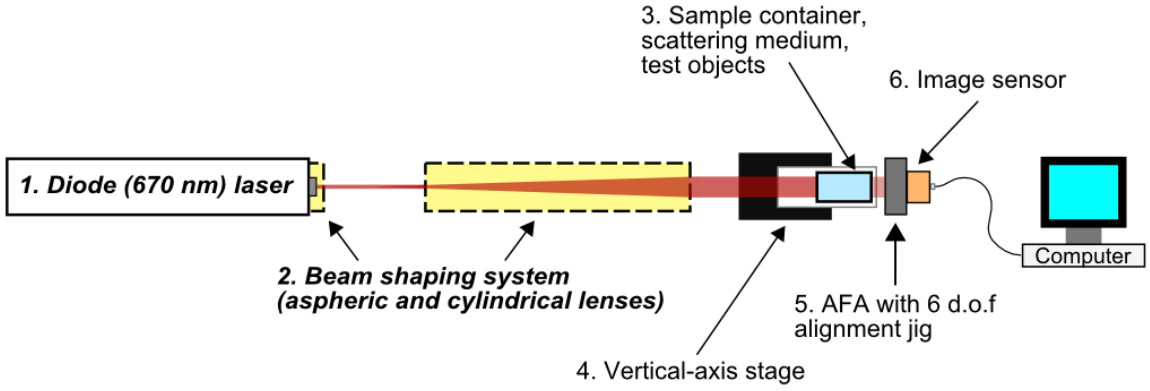

Figure 3-6 Laser diode (670 nm) trans-illumination AFA experiment setup.

3.2.2.1 Laser diode (670 nm)

The 670 nm laser diode utilized in AFA ADI experiments is a Sony SLD 1332V laser diode capable of emitting 500 mW of light at a wavelength of 670 nm and is housed in a 9 mm package [26]. The emission area of this diode laser is 100 µm wide and approximately 2 microns tall. Thus, it has asymmetric and high angular divergence along both axes, with a rated angular divergence of 8° horizontally and 24° vertically.

Laser diodes are very prone to thermal runaway because small increases in temperature cause significant decreases in resistance in a positive feedback system. Thus, these diodes must be cooled. The 670 nm laser diode was installed in a Thorlabs TCLDM9 temperature-controlled TEC laser diode cooling mount. This was controlled by a Thorlabs TED8040 temperature controller module and a Thorlabs LCD8040 laser diode current controller. The two controller modules are housed in a PRO800 2-slot modular benchtop chassis that allows for temperature and laser diode power/current control. The TEC laser diode mount is also mounted on a kinematic stage that allows for pitch and roll adjustment. Figure 3-7 is a photograph of the 670 nm laser diode and TEC cooling mount, along with two connection cables for the temperature and laser diode current controller modules.

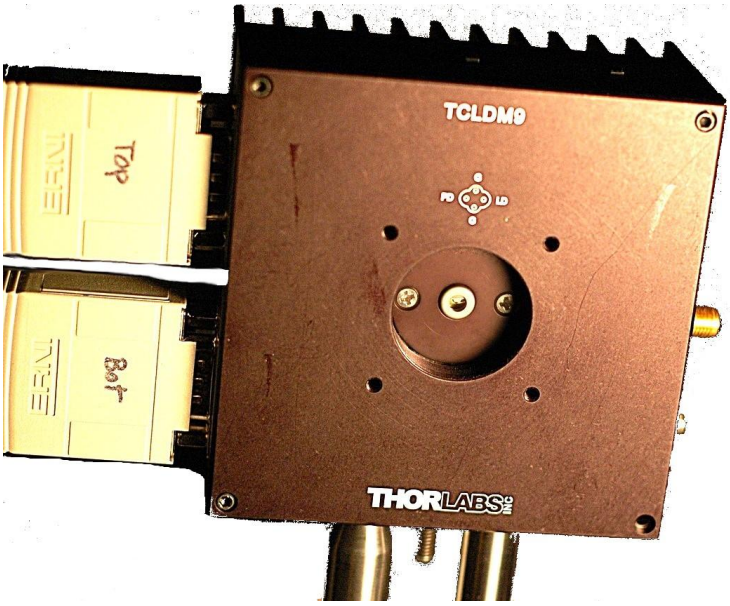

Figure 3-7 Laser diode (670 nm) and TEC cooling mount.

3.2.2.2 Beam shaping system

As mentioned in the previous section, the 670 nm laser diode produces a highly divergent beam in both axes. Therefore, in order to transform this beam into collimated light, a beam shaping system with the ability to strongly correct this divergence is required. In addition, the beam shaper must be able to correct the beam divergence independently in the vertical and horizontal axes.

The beam shaping system implemented in the laser diode AFA setup is similar to the CSC beam expander described previously (in *Section 3.2.1.2*), but with several key differences. The laser diode beam shaping system is illustrated in Figure 3-8.

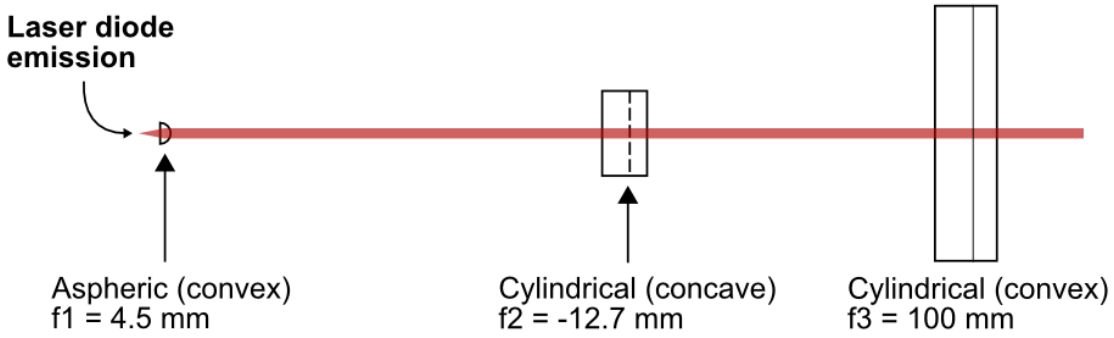

Figure 3-8 Lateral view of the laser diode beam shaping system.

A converging aspheric lens with a focal length of 4.5 mm is placed in the TEC mount and adjusted until it is one focal length away from the laser diode to collimate the beam along the vertical axis. Proper vertical collimation was determined by adjusting the lens position until the vertical height of the beam projected onto a wall approx. 2 metres away was found to be as close to the diameter of the f_1 = 4.5 mm lens. However, due to the asymmetric divergence of the beam, the lens corrects the vertical axis but converges the beam in the horizontal axis. Thus, a diverging cylindrical lens with f_2 = -12.7 mm can be used to amplify the horizontal divergence of the beam, before a converging cylindrical lens with f_3 = -100 mm corrects the horizontal divergence and collimates the beam. The relative placement of the cylindrical lenses results in an estimated 5 cm wide × 3.5 mm tall beam (i.e. an approx. 14× horizontal expansion of the beam), which was measured by eye with a ruler after projecting the beam onto a white card at various distances between

the beam expander and the AFA [25]. The beam is further restricted in width to approx. 2.3 cm using an adjustable iris placed before the sample. Cylindrical lenses are employed so that the horizontal divergence of the beam can be corrected, while keeping the beam collimated in the vertical axis. The full 5 cm wide beam (without the adjustable iris) is shown in Figure 3-9 as it illuminates a paper card and ruler.

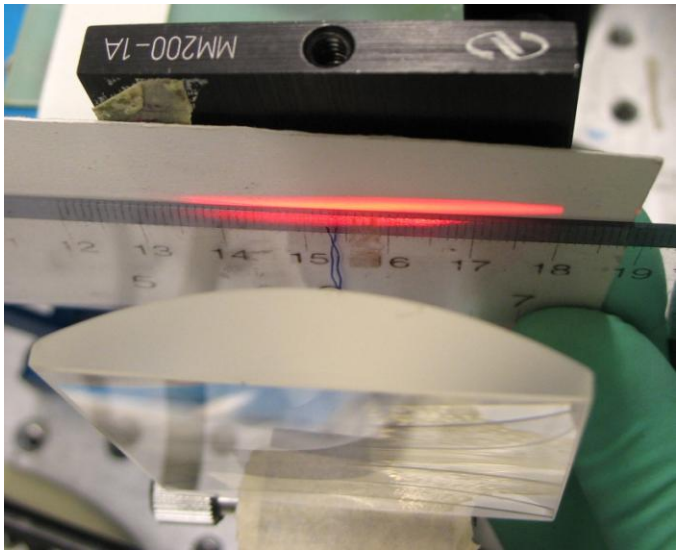

Figure 3-9 Full 5 cm wide line of 670 nm light as projected onto a paper card and transparent ruler.

3.2.3 Argon ion laser Spatial Filter ADI setup

The Argon ion laser SF setup (see Figure 3-10) is similar to the two AFA setups described previously, with several important differences. Firstly, a modified Keplerian spherical beam expander system is employed in the SF ADI setup. Secondly, the microcollimator AFA system is replaced with the converging lens and aperture-based SF system, which allows for full field imaging of the sample. Thus, the vertical-axis stage and controller are no longer necessary for raising the sample during imaging. It should also be noted that a different image sensor was utilized in this setup. Figure 3-10 shows the SF setup with major changes highlighted in italics.

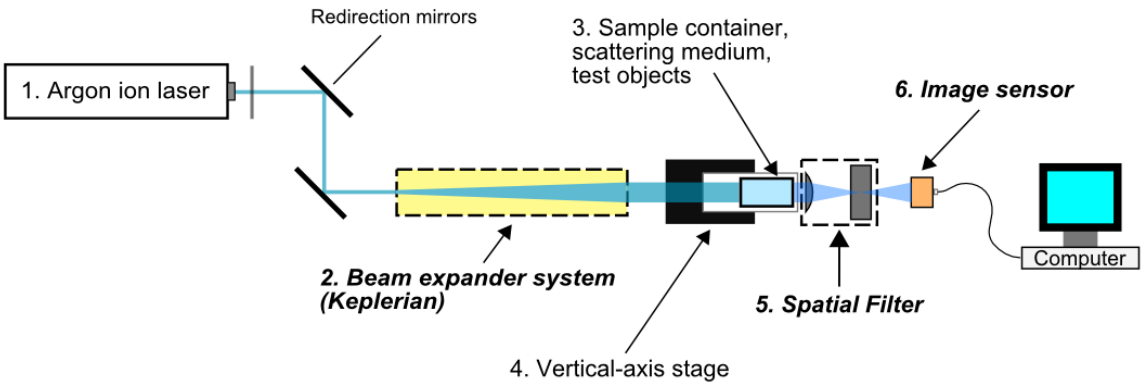

Figure 3-10 Argon ion trans-illuimation SF experiment setup.

3.2.3.1 Beam expander setup

The beam expander utilized for the SF ADI experiments is a Keplerian spherical beam expander. The Keplerian beam expander is functionally similar to the Galilean beam expander, except that it produces a crossover point in the beam where light is focussed down to a point before diverging. This beam expander configuration was chosen for the SF ADI setup because interference patterns were visible in the expanded beam produced by the Galilean beam expander. Thus, by placing an aperture (referred to in this thesis as the *pre-aperture*) at the beam crossover point, this acts as another Fourier optics filter removing high frequency patterns so that the beam can be cleaned up by removing artefacts from the beam.

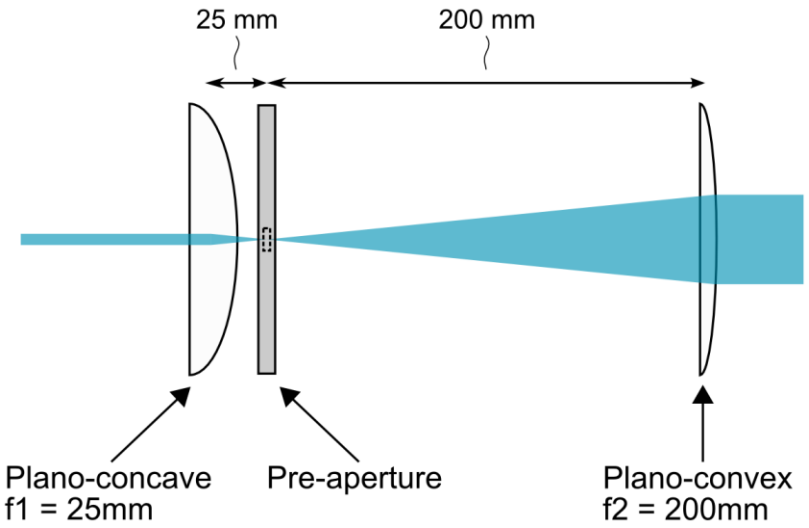

Figure 3-11 Lateral view of the Keplerian beam expander with pre-aperture.

The Keplerian beam expander utilized in the SF ADI experiments consists of a 25 mm focal length converging lens, followed by a 200 mm focal length converging lens, separated by the sum of the two focal lengths (i.e. 225 mm). The first converging lens focuses the original beam down to a point at the back focal plane of the lens, which is 25 mm from the lens. A 500 µm diameter pre-aperture is placed at the focal point to clean up the beam.

3.3 Angular filtration systems

The major distinction between trans-illumination ADI setups relates to the mechanism for discriminating between scattered and non-scattered light. Trans-illumination AFA ADI utilizes an Angular Filter Array mounted on an alignment jig to filter scattered light, whereas trans-illumination SF ADI employs a converging lens with an aperture to produce a Spatial Filter. The following subsections describe the setup of each system.

3.3.1 AFA with 6 degree-of-freedom jig

In it very important to carefully align the microcollimator AFA to the laser source in trans-illumination. The Angular Filter Array is housed in a 6 degree-of-freedom jig designed by Trinh [6]. Because the AFA microtunnels need to be in precise alignment with the collimated illumination source, the AFA is held in place and aligned by the jig, before being brought into as close contact as possible with the image sensor. The 6 degree-of-freedom jig allows for X-, Y-, and Z- translation of the AFA relative to the table, in addition to providing yaw, pitch, and roll control. An image of the AFA with 6 degree-of-freedom jig is shown in Figure 3-12. The AFA and 6 degree-of-freedom jig alignment procedure will be detailed in *Section 4.2.2*.

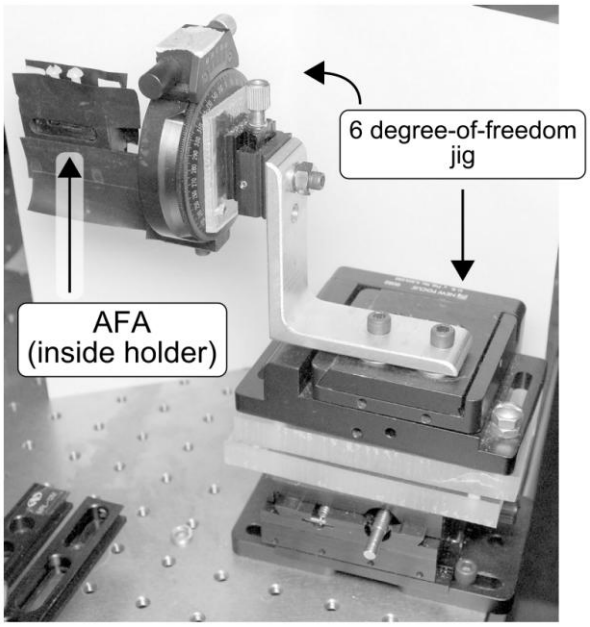

Figure 3-12 AFA with 6 degree-of-freedom jig.

Further, in-depth details on the AFA device can be found previously described in *Section 2.2* of this thesis.

3.3.1.1 Vertical-axis computer-controlled stage and controller

For the Argon ion laser experiments utilizing the AFA, a vertical-axis stage is required to incrementally raise the sample as one line is captured by the AFA and image sensor at a time. The vertical axis stage used is a Newport vertical stage (part no. PMV10172; now discontinued) controlled by a Newport PM500-C Precision Motion Controller, which receives commands from a PC through serial (RS232) communications. Together, they are able to produce micron-level precision motion. A second setup uses an alternative stage and motion controller, the GTS30V High-Precision Vertical Linear Stage and the XPS Universal High-Performance Motion Controller/Driver, respectively.

Both of these setups incrementally raise the scattering sample during AFA imaging by steps of 52 µm or smaller, with a typical scan total of 100-200 steps or rows. For example, a default step size of 52 µm and 100 rows produces an image 5.2 mm tall. Regions several times that height are capable of being imaged using these stages.

While the experiments presented in this thesis do not make use of the new vertical stage and motion controller, the most recent setup for AFA ADI experiments makes use of the GTS30V and XPS motion controller. The image capture software, *CtrlGui*, was modified by the author to be compatible with the new hardware, which communicates with the PC via the Ethernet network protocol.

3.3.2 Aperture-based Spatial Filter system

The basic operating principles of the aperture-based SF system have been previously described in *Section 2.3.1 – Spatial Filter ADI design and geometry*. The SF system (see Figure 3-13) consists of a converging lens which focuses ballistic and quasi-ballistic light through an aperture placed at the focal plane, with an image sensor placed at a certain image distance past the aperture.

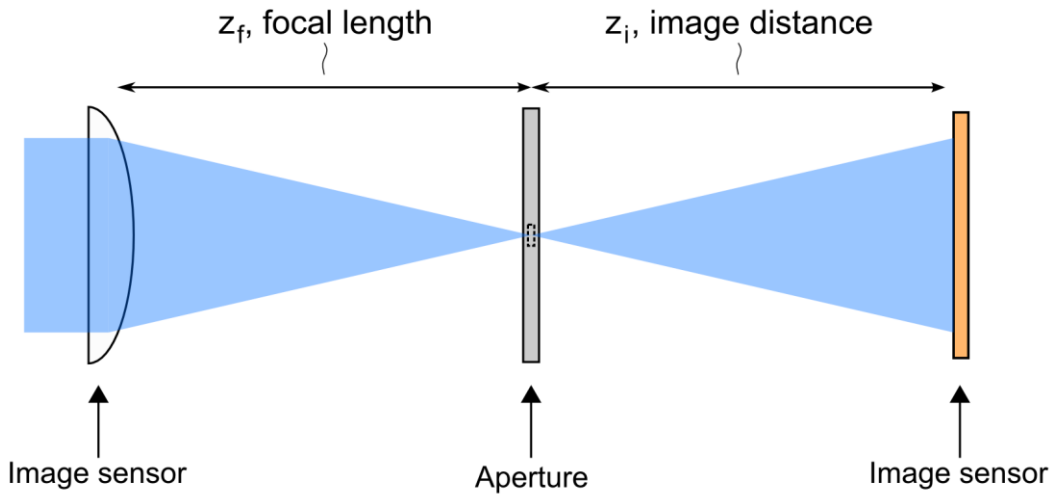

Figure 3-13 Diagram of the SF system.

3.3.2.1 Converging lens

As part of the spatial filter experiments, the following lenses with varying focal lengths were used:

1. **35 mm focal length** (Edmund Optics, TECHSPEC® Near Infrared Achromat, NT45-800)
2. **50 mm focal length** (Newport, BK 7 Plano-Convex lens, 430-700 nm anti-reflection coated, KPX082AR.14)
3. **100 mm focal length** (Edmund Optics, TECHSPEC® Near Infrared Achromat, NT45-806).

Multiple lens focal lengths were employed to verify the focal length relations predicted in SF theory (see Equation 2-4 and Equation 2-8).

3.3.2.2 Aperture

The SF formulae in *Section 2.3* show that spatial filter acceptance angle and resolution depend on the aperture diameter d_a. The aperture diameters used for spatio-frequency filtering in this work range in size from 100 µm, approx. 161 µm, approx. 214 µm, and 300 µm. The 300 µm and 100 µm apertures were purchased from Edmund Optics as mounted precision pinholes (NT56-285 and NT56-283, respectively). The apertures are mounted either on a Multi-Axis Lens Positioner (LP series) from Newport (see Figure 3-14), or a custom assembled aperture mount (using standard mirror mounts, optical posts, and micropositioners). These aperture mounts provided precision positioning of the aperture (estimated tens of microns) in all three axes.

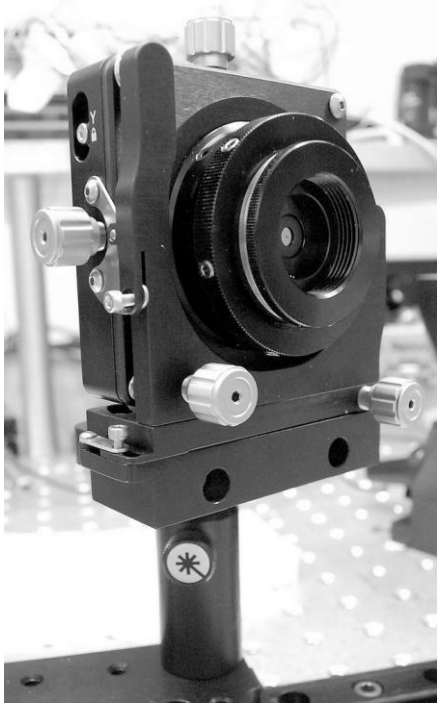

Figure 3-14 Photograph of the aperture mount (Multi-Axis Lens Positioner).

The 161 µm and 261 µm diameter apertures were created in the School of Engineering Science (Simon Fraser University) cleanroom by another member of Dr. Glenn Chapman's research laboratory, using a laser direct-write bimetallic grayscale photomask technology [27]. In this process, a circular aperture pattern is written onto a bimetallic film using a focussed laser beam, which produces a binary photomask of the aperture. 0.2 The aperture pattern was fabricated for this thesis using sputter deposited aluminum (approx. 0.2 mm thick) on glass slides and patterned using photolithography from the photomask. Thus, the 161 µm and 261 µm diameter apertures are actually circular openings in an aluminum thin film on glass.

3.4 Scattering sample apparatus and setup

This section describes the scattering test sample apparatus and setup for different ADI experiment configurations.

3.4.1.1 Milk-based scattering solution samples

Milk-based scattering solution experiments were conducted using a 5 cm long sample container which holds the scattering medium (milk solution) and a glass slide with test object patterns. The sample container is 5 cm long, with the front and back faces formed by glass microscope slides approx. 2 cm × 2 cm in area (Figure 3-15). The sample container is illuminated from the front by the light source, with the angular filter and camera capturing an image from the back. Between the back and front positions, there exist four additional positions (P1-P4) marked by notches in the container. These positions are 0.8 cm (P1), 1.8 cm (P2), 2.7 cm (P3), and 3.8 cm (P4) in distance from the back face. The back and front positions correspond to distances of 0 cm and 5 cm from the back, respectively.

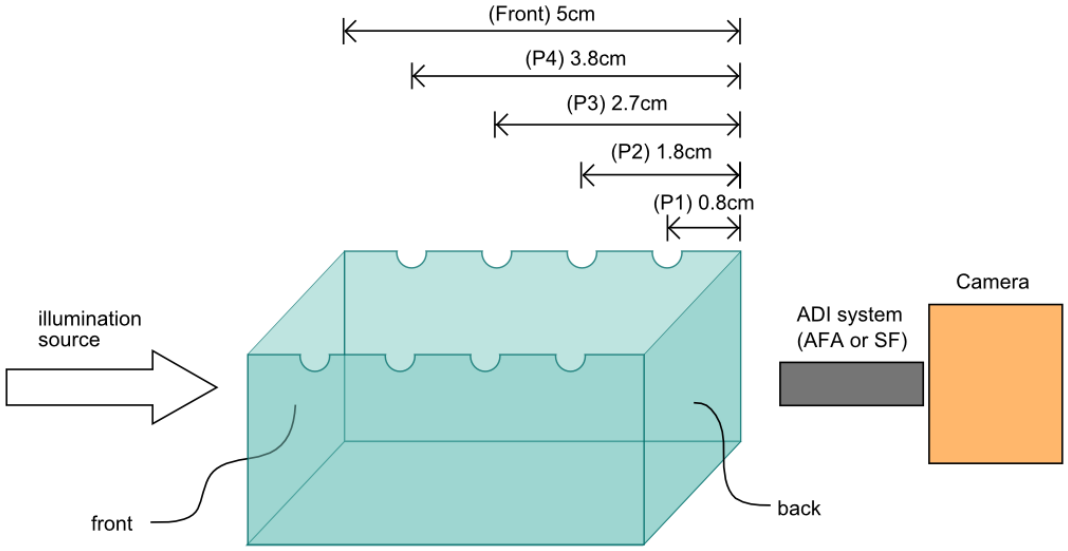

Figure 3-15 Diagram of the sample container.

Previous research [9] has shown that test objects close to the back of the scattering solution are imaged with higher contrast and definition. Thus, multiple positions in the sample container allow the test objects to be placed at varying longitudinal depths, as desired.

The scattering medium used in the Argon ion ADI experiments is a calibrated milk solution. DI water is mixed with specific volumes of 2% milk fat dairy milk to produce a

scattering solution with a desired scattering ratio. Further details on the preparation and calibration of the milk scattering solution is given in *Section 4.1*, as well as in previous literature [3], [9].

3.4.1.2 Small resolution test structures

The test objects used in imaging consist of aluminum L-shaped line and space structures patterned onto a glass slide (see Figure 3-16). Each test structure is comprised of aluminum lines or gaps with the same, fixed width. These lines and gaps are put together to form a distinctive L-shaped pattern for imaging. The smallest four test structures, found on the small test structures slide, are the 51 µm, 102 µm, 153 µm, and 204 µm objects, as defined by the fixed width of their lines and spaces (Figure 3-16a). The largest four test structures, found on the large test structures slide, are the 204 µm, 255 µm, 306 µm, and 357 µm objects (Figure 3-16b).

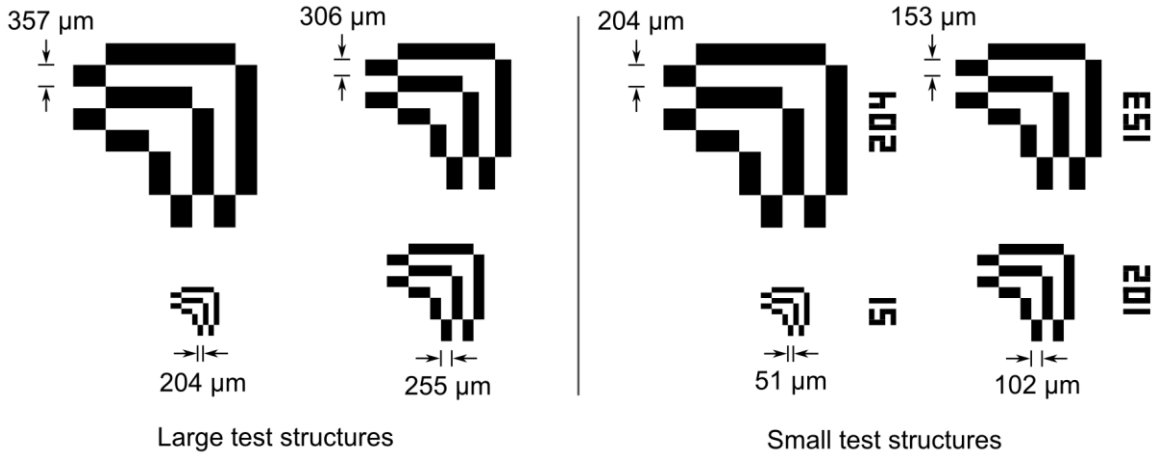

Figure 3-16 Large and small test structure slides.

The large test structures slide was produced by other members of Dr. Glenn Chapman's research laboratory using a direct-write grayscale photomask technology. As such, it exhibits higher edge roughness (~2 µm roughness) as compared to the small test structures slide, which were patterned photolithographically from a chrome mask (< 0.5 µm roughness). Research in this thesis deals primarily with the small test structures for imaging experiments.

3.5 Image sensor and capture software

Two different image sensors, both with nearly identical specifications, are used in this thesis research. All AFA ADI experiments were conducted using the same image sensor and associated software, while another image sensor was used for all SF ADI experiments.

3.5.1 Image sensor and capture software for AFA ADI experiments

The current CMOS image sensor used for all AFA ADI experiments was chosen in 2005 to replace an older CCD image sensor [25] [28]. An Electrim 3000D camera (see Figure 3-17) was chosen, which is based on a Micron MT9M001 active-pixel CMOS sensor with 10-bit resolution. The sensor has a 5.2 µm × 5.2 µm pixel size and sensor dimensions of 6.66 mm (H) × 5.32 mm (V) or 1280 (H) × 1024 (V) pixels. The sensor is connected to a host PC via USB. Further details on this detector are described by Dudas [28].

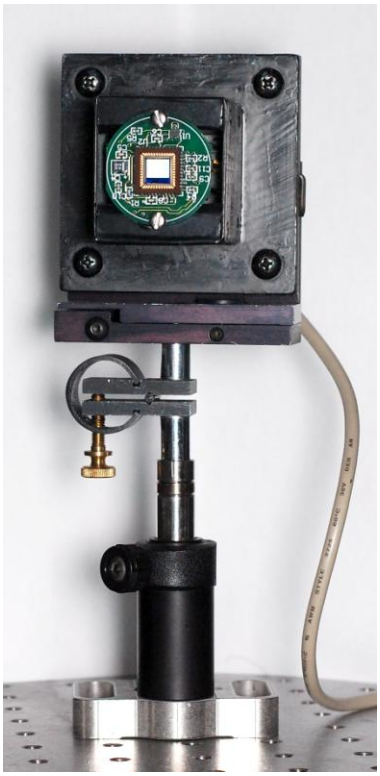

Figure 3-17 Electrim 3000D camera.

Custom software, known as *CtrlGUI*, was written for the Electrim 3000D camera by Dudas [28]. *CtrlGUI* features a graphical user interface and was developed in C++. The program allows for image capture and many settings to be adjusted, including exposure times and sensor gain. *CtrlGUI* also handles motion control of the Newport vertical stage via serial port (RS232) communications with the Newport PM500-C Precision Motion Controller. The program coordinates vertical stepping of the stage and sample container with image capture, and produces a full two-dimensional image from each line image that is captured at different positions of the sample container. Figure 3-18 shows a screenshot of the *CtrlGui* program.

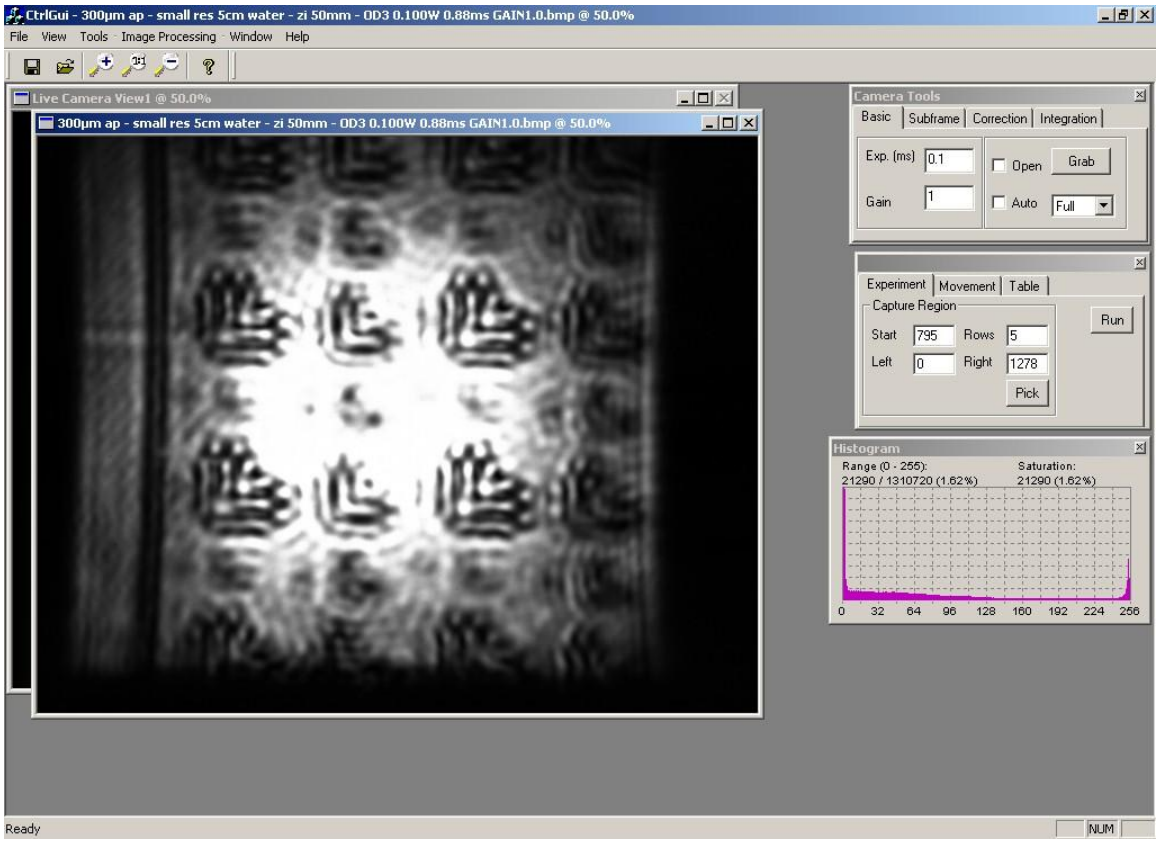

Figure 3-18 Screenshot of the *CtrlGui* image capture program.

3.5.2 Image sensor and capture software for SF ADI experiments

The CMOS image sensor was changed for Argon ion trans-illumination SF ADI experiments. This change was made because a separate setup from the AFA ADI experiments was being used. The Sumix Corporation SMX-M81M camera (see Figure

3-19) was chosen as a replacement camera, as it shares the same sensor element and specifications as the previous camera with a 5.2 µm × 5.2 µm pixel size, a sensor dimension of 1280 pixels (H) × 1024 pixels (V), USB connectivity, and 10-bit resolution. This camera was procured through ViewBits, a division of Computer Modules, Inc., and is sold as the Gemini - Ultra Compact Monochrome 1.3 Megapixel CMOS camera.

Figure 3-19 Photograph of the SMX-M81M camera.

The software used with the SMX-M81M is provided by the Sumix Corporation for the SMX-M8x series of cameras. Similarly to the *CtrlGui* software developed for the previous camera, it allows for exposure and gain control. It is used primarily to capture full-frame images in SF ADI experiments, and does not operate in conjunction with a vertical stage and motion controller because no motion of the sample container is required with SF experiments. One limitation of this software is that a maximum exposure of only 131.40 ms was possible with this camera and software. Figure 3-20 shows a screenshot of the SMX-M8x series image capture software.

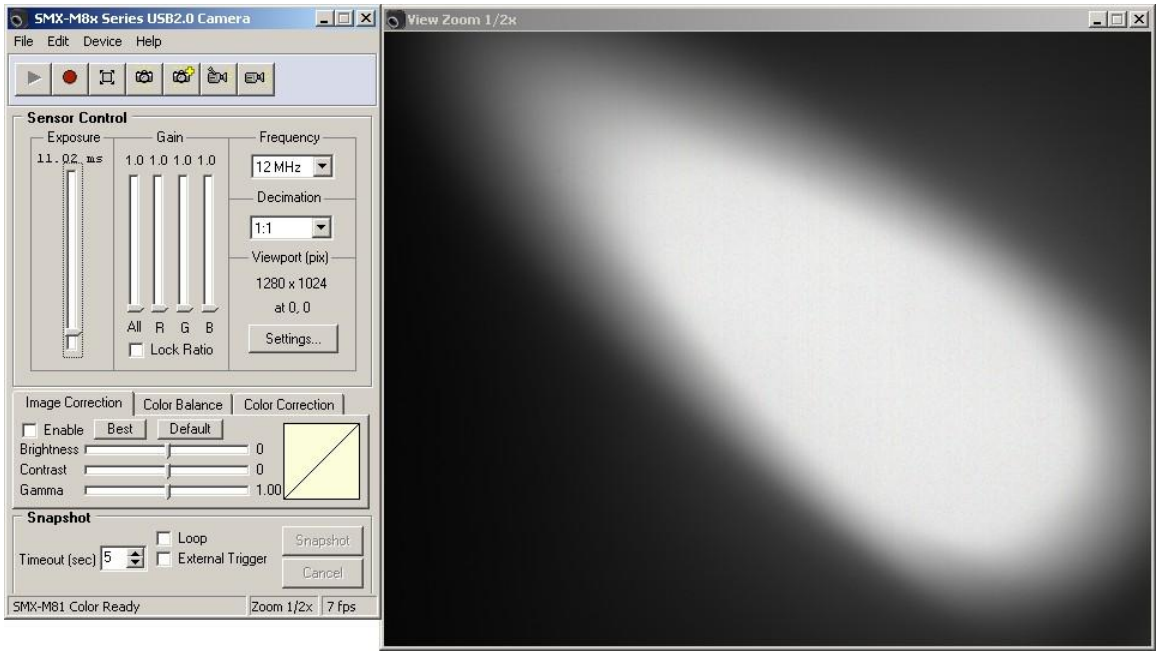

Figure 3-20 Screenshot of SMX-M8x series software.

3.6 Chapter summary

In this chapter, the experimental apparatus and setup for Argon laser AFA, 670 nm laser diode AFA, and Argon laser SF ADI setups were described. The first utilizes an Argon ion laser source with a Galilean spherical beam expander system to produce a 2.3 cm circular beam. An alternate Cylindrical-Spherical-Cylindrical lens beam shaping system can also be implemented, which produces a thin line of light approx. 21 mm wide × 0.13 mm tall. The second AFA setup employs a 670 nm laser diode with cooling mount and a beam shaping system similar to the CSC beam expander to produce a line of light estimated to be 5 cm wide × 3.5 mm tall. The SF ADI setup also utilizes the Argon ion laser, but with a Keplerian spherical beam expander with pre-aperture to produce a 2.3 cm circular beam. The two angular filtration systems in use are the Angular Filter Array with 6 degree-of-freedom jig and the aperture-based Spatial Filter system. In addition, the milk-based scattering solution, biological tissue samples, and small resolution test structures used in imaging experiments were described. The vertical axis stage, image sensor, and image capture software were also discussed. Finally, the apparatus and setup used for scattering medium calibration was outlined.

The following chapter outlines the experiment procedure and method for the ADI research in this thesis.

Chapter 4

Experimental Method

In this section, experimental overviews are given for the following four categories: scattering sample preparation and calibration (both milk-based scattering solution and biological tissue), Argon laser AFA ADI, 670 nm laser diode AFA ADI, and Argon laser SF ADI.

Preparation and measurement procedures for both milk-based scattering solutions and biological tissue samples are described in this chapter, along with the theory involved in calculating the Scattering Ratio for a sample. Observations on the behavior of milk-based scattering solutions are also discussed. For all three ADI setups, the laser source setup, beam shaper setup and alignment, angular discrimination system (AFA or SF) setup and alignment, and image capture procedures are described. It should be noted that all optical experimental results are taken with ambient illumination in the room brought to a minimum. The overall methodology for preparing and imaging a scattering sample using the Argon or 670 nm laser ADI setups is similar to the methodology described in previous work by the author [9].

4.1 Scattering sample preparation and calibration

For precise experimentation, it is highly important to obtain the test medium's Scattering Ratio value.

4.1.1 Preparation of milk-based scattering solutions

Milk-based scattering solutions are prepared by injecting specific volumes of 2% Milk Fat (M.F.) dairy milk into 20 mL of deionized (DI) water. The type and quantity of milk that is mixed in with the water will determine the Scattering Ratio of the resulting solution. The SR value of the milk-based solution also varies depending on the batch of milk used, the exact quantities of milk or water used, and the age of the solution, so it is

important to test each solution after preparation and near to the time of the imaging experiments.

To create the milk solution, 20 mL quantities of DI water are measured out using a small graduated cylinder before being poured into a plastic container or glass vial. Milk is then injected into the 20 mL sample of water using a 1 mL hypodermic syringe (with 0.01 mL minor markings). The milk-water mixture is then stirred to form the solution and stored in a plastic container or glass vial, as previously mentioned.

4.1.2 Scattering measurement of milk solution and biological tissue samples

It is important to calibrate the scattering sample to determine their Scattering Ratio for each experiment. Milk solutions are transferred into a 1 cm thick glass container (pictured in Figure 4-1) using an eyedropper and placed onto an adjustable vertical stage where it is illuminated by the Argon or 670 nm laser beam. An initial power measurement through a water-filled 1 cm container is taken as a baseline under zero scattering conditions before the *SR* is calculated for milk solution samples. Biological tissue samples are introduced directly into the beam path at the same location as milk solution samples and held in place (e.g. by tape onto a mirror mount). The Scattering Ratio of the milk solution or biological tissue sample can then be determined by illuminating the sample and measuring the fraction of transmitted light power through the solution.

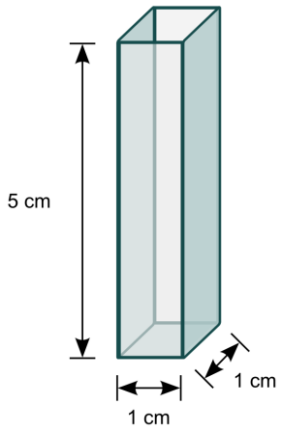

Figure 4-1 Illustration of the 1 cm scattering sample container.

Figure 4-2 illustrates the general setup used in measuring the Scattering Ratio of either a milk-based scattering solution or biological tissue sample of variable thickness.

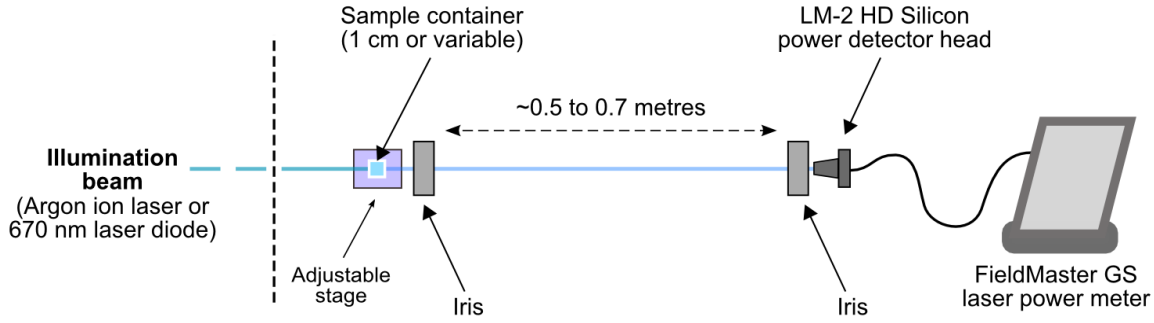

Figure 4-2 Scattering medium calibration setup.

The scattering sample and laser power meter are separated by a relatively large distance (approx. 50 to 70 cm), with one 2 mm diameter iris placed immediately after the scattering sample, and another placed immediately before the laser power meter. These irises form an acceptance angle (approx. 2.3° to 1.6°) that allows only ballistic photons and some portion of the quasi-ballistic photons that have passed through the sample with little or no deviation in angle to reach the detector. It should be noted that in scattering measurements using the 670 nm laser diode, an additional iris is first placed at the output of the beam shaping system which restricts the line of light to a 2 mm diameter circular beam before the sample container is illuminated.

Either the Argon ion laser or the 670 nm laser diode can be used as the illumination source to calibrate the scattering solution. Note that the scattering ratio varies with the wavelength as should be expected. A neutral density filter, which reduces the illumination intensity by a fixed amount across a broad range of wavelengths, is often used with the Argon ion laser to reduce the beam intensity to an intensity of approx. 100 µW (primarily for safety reasons). When the 670 nm laser diode is used in calibration measurements, the shaped beam is further restricted by an aperture to produce a 2 mm diameter beam, which is then used to illuminate the sample container.

The transmitted light power through the illuminated sample is measured using a Fieldmaster GS laser power meter, with an attached LM-2 HD Silicon power detector head, produced by Coherent Inc. For milk-based scattering solutions, the 1 cm sample container is placed on a stage and separated from the laser power detector by a typical distance of approximately 0.5 to 0.7 metres [9], [25]. For biological tissues, the sample can be mounted on a kinematic mirror mount which provides tilt and yaw adjustment. An iris is placed in front of the power detector and another is placed immediately behind the sample in order to restrict the transmitted illumination seen by the detector to a small and defined solid angle.

Figure 4-3 shows a photograph of an example scattering measurement setup. It should be noted that the configuration and distances shown in the photograph are slightly different from those used in the thesis work.

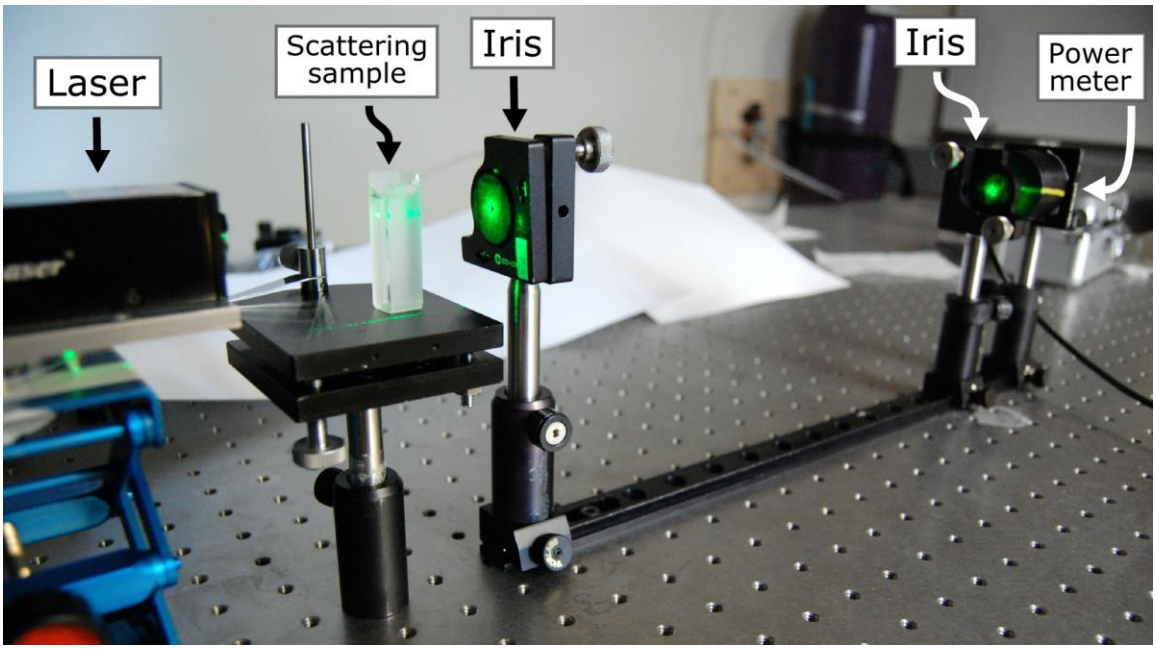

Figure 4-3 Photograph of an example scattering measurement setup.

4.1.3 Calculating the SR value for the scattering medium

The Scattering Ratio formula (Equation 1-9) states that the SR value is the ratio between the scattered light and the ballistic or quasi-ballistic light. When SR is very high,

scattered light heavily dominates non-scattered light, and thus virtually all the light that illuminates the sample is converted into scattered light. Using the setup of *Section 4.1.3*, the SR can be calculated by,

$$SR = \frac{P_i}{P_o} - 1, \qquad \textbf{Equation 4-1}$$

where P_i is the intensity of light transmitted through a DI water solution, P_o equal is the output light power that is transmitted through the scattering sample (within the irises) and detected by the laser power meter. This calculation assumes that the effect of absorption is negligible, which is typically the case.

To extrapolate the SR from a 1 cm thick medium to a scattering medium of different thickness, the Beer-Lambert law (Equation 1-1) indicates an exponential relationship as follows,

$$SR = \left(\frac{P_i}{P_o} - 1\right)^{d/l} \approx \left(\frac{P_i}{P_o}\right)^{d/l} \text{ for very large } \frac{P_i}{P_o}, \qquad \textbf{Equation 4-2}$$

where d is the new thickness of the scattering medium, and l is the original thickness of the test scattering cell (1 cm for milk-based solutions). Thus, to find the equivalent 5 cm SR for a scattering medium that has been tested at a thickness of 1 cm, the original SR must be raised to the 5^{th} power.

4.1.4 Observations on milk-based scattering solutions

From previous research, the scattering level in milk-based scattering solutions is approximately exponentially related to the concentration of milk [9]. This exponential relationship indicates that increasing the volume of milk in a solution has the direct effect of increasing the scattering coefficient μ_s of the solution. Figure 4-4 gives a measured example of the exponential relationship between the SR of a 5 cm thick medium (plotted in logarithmic scale) and the volume of milk mixed into 20 mL of DI water (linear scale) for a batch of milk solutions.

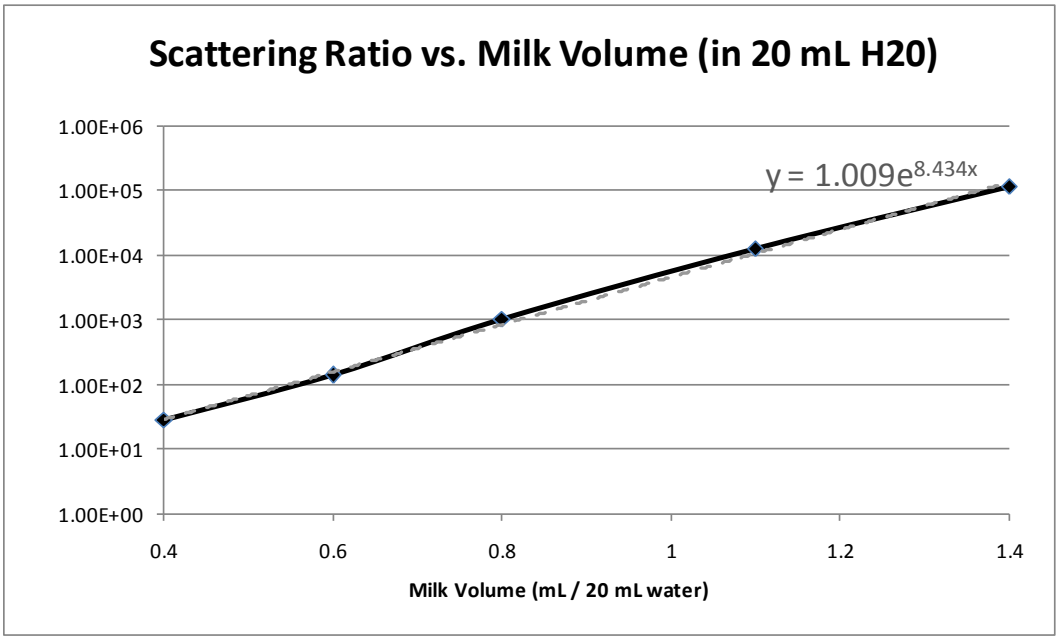

Figure 4-4 Exponential relationship between SR and milk volume (in 20 mL of DI water).

The above graph confirms the exponential relationship between the amount of milk present in a 20 mL sample of water and the measured Scattering Ratio of the solution. A fitted exponential trendline gives a formula with a linear coefficient of 1.009, which represents the estimated SR value for a pure water solution. Although an SR of 0:1 would be expected for water (no scattering), the Scattering Ratio values calculated for Figure 4-4 did not use the exact formula,

$$SR = \frac{1 - T_s}{T_s}, \qquad \text{(from Equation 1-9)}$$

but instead uses the simpler formula,

$$SR \approx \frac{1}{T_s}.$$

This formula is only valid for very small T_s (where T_s represents the probability of a photon encountering no scattering), whereas in the non-scattering case, T_s is large (i.e. equal to 1). Therefore, instead of SR = 0:1, the approximate formula yields $SR \approx \frac{1}{T_s} = 1{:}1$, which matches with the fitted coefficient of 1.009.

The fitted line also gives an exponential coefficient of 8.434, which represents the scattering coefficient of milk (diluted by 20 times) times the depth of the sample (i.e. $\mu_s \times d$) as indicated by the Beer-Lambert law (Equation 1-1), assuming absorption is negligible. Thus, by dividing by the sample thickness d = 5 cm, the estimated scattering coefficient becomes $\mu_s' = 1.67\ \text{cm}^{-1} \times 20 = 33.4\ \text{cm}^{-1}$ for milk (2% milk fat).

Milk-based scattering solutions have been observed to change in scattering level over time. Figure 4-5 presents SR measurements for four different milk solutions as measured at their time of preparation (0 hours) and at several points (up to 147 hours, or 6.125 days) after preparation. These samples were kept refrigerated for a large portion of their lifetime when not in use. Refrigeration was not observed to have a consistent, predictable effect on Scattering Ratio change over time, though further in-depth experimentation in this area can be conducted.

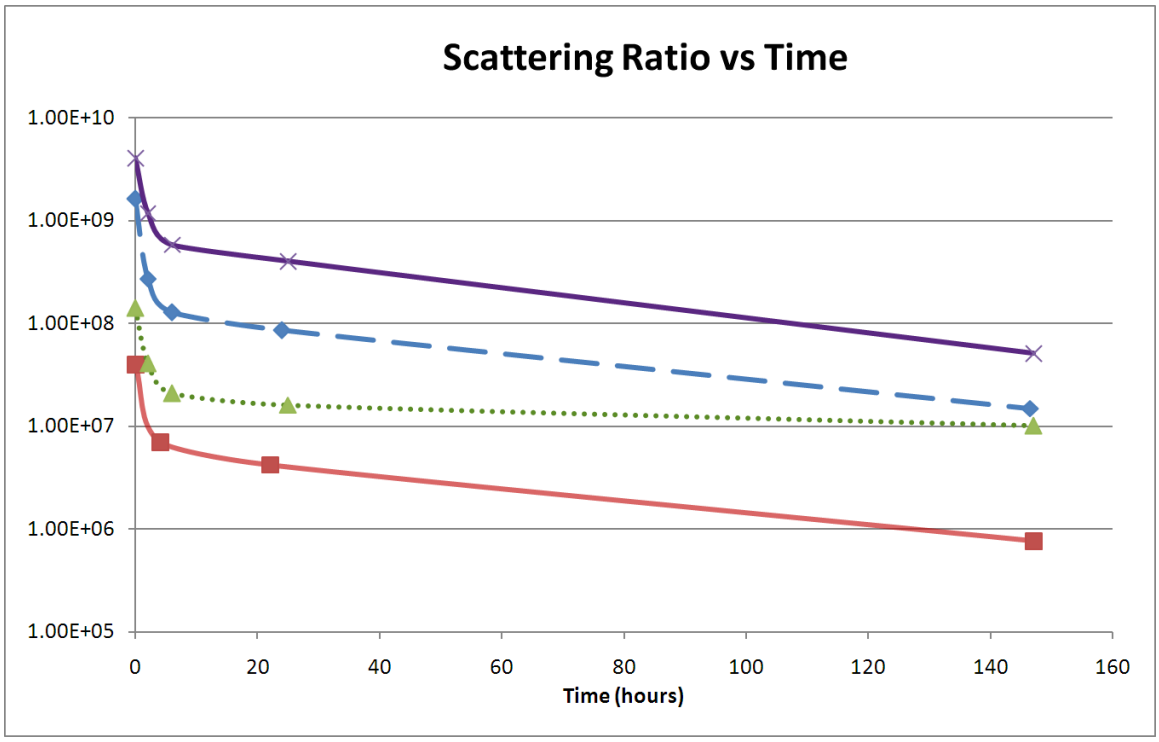

Figure 4-5 Change in Scattering Ratio over time for milk-based scattering solutions.

The mechanism for this change is as of yet unknown to the author. One reason that the solution is unstable over time may be due to the biological nature of the milk solution in

addition to bacteria in the environment. Another reason may be related to the physical properties of the milk solution and how the milk constituents are held in suspension or solution in the mixture.

The variance in Scattering Ratio over time is not consistent, and changes depending on the particular batch of milk solution that has been prepared. However, some general trends that can be observed are that a rapid decrease in SR occurs in the early hours after sample preparation (approx. 6 to 12 hours) such that approximately one order of magnitude is lost in the SR value. Further experimentation and characterization of milk-based scattering solutions should be undertaken in order to help ensure that their scattering properties can be accurately predicted for imaging, even over longer periods of time. After this behaviour was better understood, SR was measured more often for the milk-based scattering solutions, not only before the imaging experiments but also in between and/or after the experiments were conducted.

4.2 Argon laser AFA experimental overview

The Argon laser AFA setup is virtually identical to that used in previous research as described in the undergraduate theses written by the author [9] and Trinh [6]. The setup, diagrammed previously in Figure 3-1, is shown photographed from overhead in Figure 4-6.

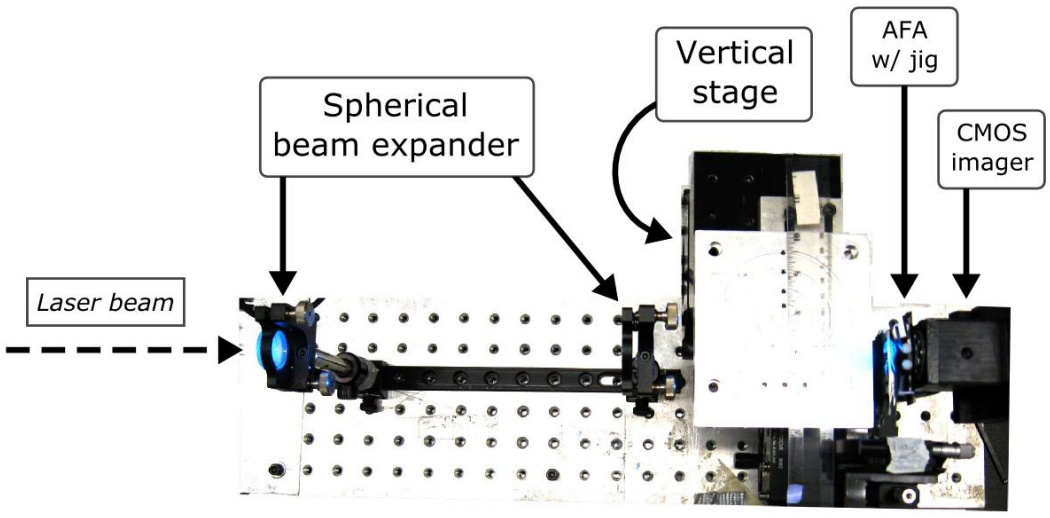

Figure 4-6 Photograph (overhead view) of Argon laser AFA ADI experiment setup.

The Argon laser AFA ADI setup is used to conduct trans-illumination scans of calibrated milk-based scattering samples in this thesis. The following description outlines the procedures required to prepare and run the Argon ion laser source and perform imaging experiments on the milk solution samples.

Firstly, the water cooling and safety warning light bulb must be engaged before the power supply and laser can be activated. Milk-based scattering solutions must be prepared and calibrated as described previously. The beam expander/shaping optics must be carefully aligned (see *Section 4.2.1*), along with the AFA with 6 degree-of-freedom jig and image sensor to the incoming light (*Section 4.2.2*). The scattering sample can then be imaged using the capture hardware and software (*Section 4.2.3*).

4.2.1 Beam expander/shaping optics

Both the Galilean beam expander and the CSC beam expander have been employed in previous research with the Argon laser AFA setup. Further details regarding alignment procedures are contained in *0* [9]. The Galilean beam expander was the only beam shaping system employed for Argon laser AFA experiments in this thesis.

Aligning the Galilean beam shaper consists of the following main procedures.

1. Autocollimate the back lens (200 mm converging lens).
2. Autocollimate the front lens (-25 mm diverging lens).
3. Adjust the separation between the two lenses until beam is collimated.

Autocollimation of a lens is the procedure whereby a beam illuminates a lens with some portion of the beam reflected backwards, and the lens is adjusted until the reflected beam passes along the same path as the original, incoming beam. The separation between the two lenses was adjusted by hand on an optics rail with sliders, and collimation was determined as when the beam diameter as projected onto a card immediately in front of the expander output most closely matched the diameter as projected at a far distance

(e.g. 2 metres away). In general, the beam expander remains stable during experiments once adjusted.

4.2.2 Alignment of AFA, 6 degree-of-freedom jig, and image sensor

The alignment procedures for the AFA, 6 degree-of-freedom jig, and the image sensor have been explained in detail previously by the author (see 0) [9]. The AFA alignment procedure requires the image sensor to first be centered on the illumination beam. Secondly, the AFA must be placed in its cradle within the 6 degree-of-freedom jig and then aligned to the incoming beam of illumination such that illuminated tunnels are visible by the image sensor. Finally, the AFA must be brought into as close contact with the image sensor as possible to minimize spreading from the tunnels.

4.2.3 Image capture procedure

The image capture procedure consists to two main parts: introducing the sample to the system and imaging the sample. The 5 cm thick sample container is first filled with the milk-based scattering solution, with the test structure slide suspended in the container at a specific position. The sample container is then placed on the vertical axis stage, directly in front of the AFA.

Imaging the sample is done via the *CtrlGui* program. Because only a horizontal section of the sample is being imaged at one time during the scan, the appropriate section of the image sensor must be selected using *CtrlGui*. The program can then image horizontal slices of the scattering sample while the sample is incrementally raised using the motorized vertical stage, all according to the exposure, gain, and movement parameters set in *CtrlGui*. Finally, the horizontal slices are put together to form a 2-D image of the sample that can be saved as an image file. The vertical stage step size and starting position can be set in the software, along with exposure time and gain. The exposure and gain must be carefully set so that the image is not saturated (where a significant portion of pixels are at the maximum intensity).

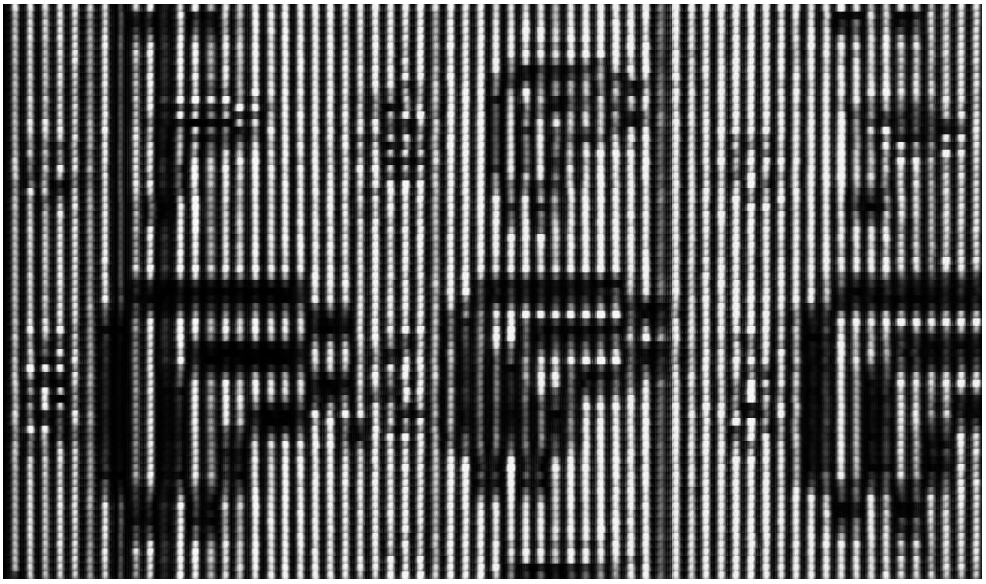

Figure 4-7 Sample image captured using the *CtrlGui* program.

4.3 670 nm laser diode AFA experimental overview

The 670 nm laser diode AFA setup is used to conduct trans-illumination scans of both calibrated milk-based scattering solutions and biological tissue samples in this thesis. This setup is similar to the Argon laser AFA setup, with the main differences pertaining to the illumination source, beam shaping optics, and the kinds of samples being imaged. Figure 4-8 gives a photograph of the 670 nm laser diode AFA setup.

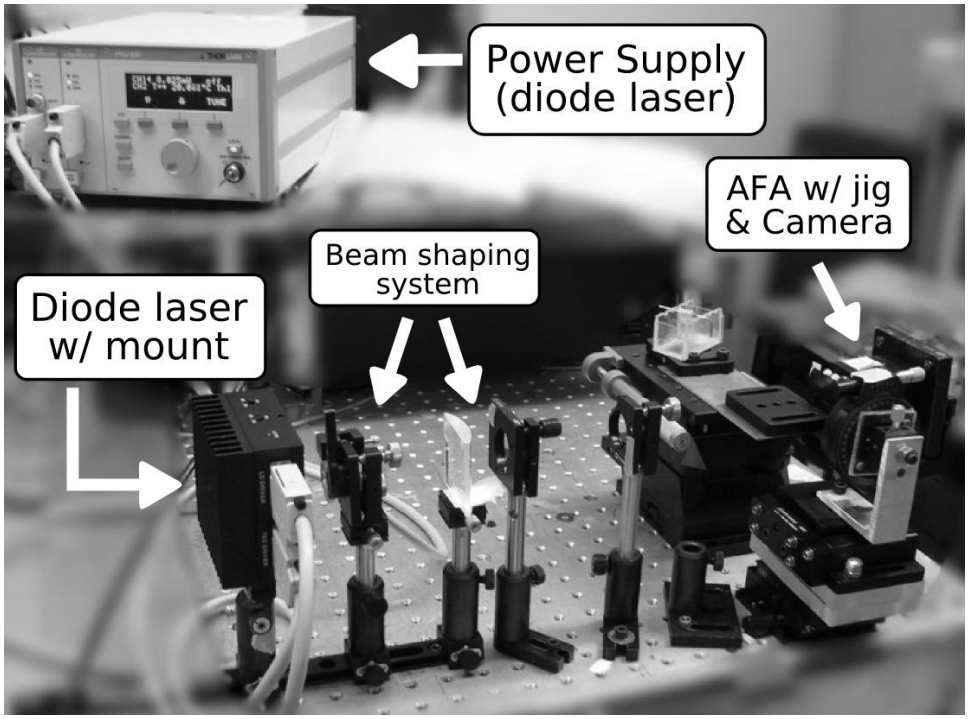

Figure 4-8 Photograph of 670 nm laser AFA ADI experiment setup.

The basic procedure for imaging with the 670 nm laser diode AFA setup begins first by engaging the laser diode temperature controller module to bring the laser diode to a specific temperature, at which point the laser diode current controller module can be powered on. The beam shaping optics must be properly set up and aligned, along with the AFA and image sensor as described previously. Finally, milk solutions or biological tissue samples can be imaged using the capture hardware and software.

The beam shaping system for the 670 nm laser diode AFA system consists of a 4.5 mm converging aspheric lens, a -12.7 mm diverging cylindrical lens, and a 100 mm converging cylindrical lens.

First, in order to collimate the diode laser output, the 4.5 mm aspheric converging lens is brought into correct position a few millimetres from the laser diode by screwing its mount into a socket on the TEC laser diode cooling mount. The separation distance between the laser diode and the aspheric lens can be controlled by screwing or unscrewing the aspheric lens mount until the vertical divergence of the beam is corrected

by the lens. While the beam is collimated vertically by the converging aspheric lens, it is overcorrected horizontally and quickly converges to a point before diverging in the horizontal axis. Thus, the -12.7 mm diverging cylindrical lens is placed at a particular distance (approx. 3 cm) from the aspheric lens to amplify this horizontal divergence. The 100 mm converging cylindrical lens is then placed approx. six cm after the diverging cylindrical lens such that the diverging beam is collimated in the horizontal axis. This configuration produces a collimated beam at some fixed width and height.

To produce a 5 mm x 3.5 mm wide beam, the exact separation distances between the three lenses can be adjusted experimentally by trial and error. This is done by modifying the location of the first cylindrical lens, followed by adjusting the second cylindrical lens to re-collimate the beam, until the desired beam dimensions are created. The beam produced by the beam shaper is pictured in Figure 3-9. Finally, an adjustable iris is placed after the beam shaper to limit the width of the beam to approx. 2.3 cm.

4.4 Experimental overview for the SF ADI setup

The Spatial Filter ADI setup is used to capture trans-illumination images of calibrated milk-based scattering solutions, similarly to the Argon laser AFA setup. Two major differences in experimental procedure for the SF setup arise from the setup and alignment requirements of using a Keplerian beam expander with pre-aperture in place of the original Galilean beam expander, and the introduction of the SF system in place of the AFA and alignment jig. In addition, a different camera and image capture software were used for the SF ADI experiments for logistical reasons. Figure 4-9 shows a photograph of the Argon laser SF ADI setup.

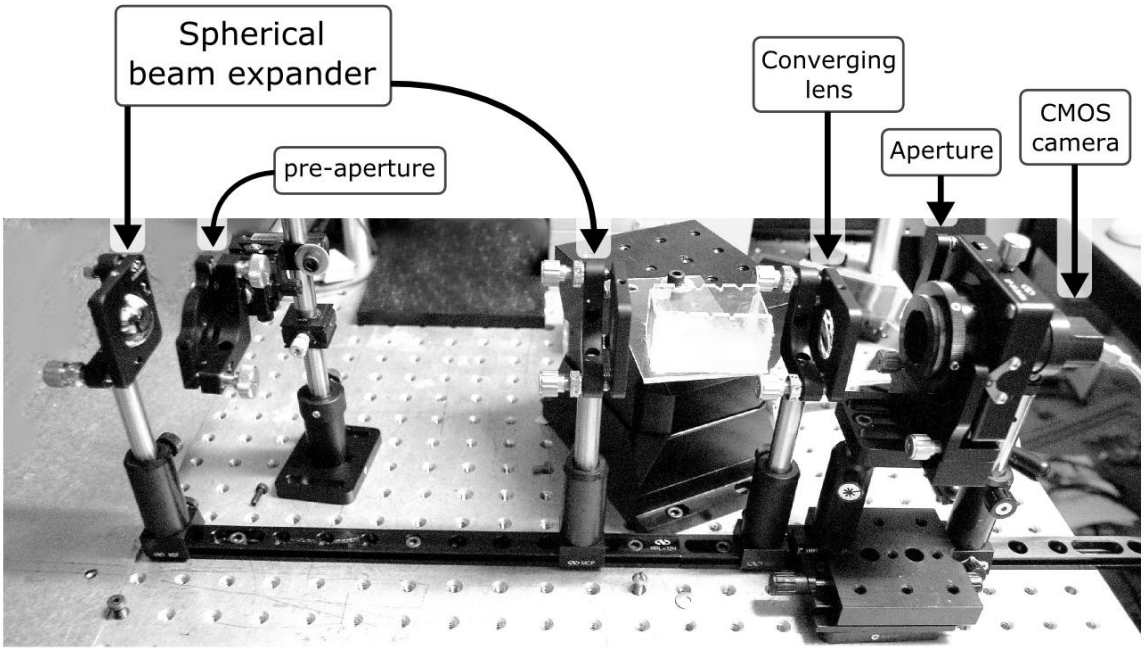

Figure 4-9 Photograph of Argon laser SF ADI experiment setup.

The SF ADI experimental procedure is similar to the previous ADI setups described in this chapter. First, the water cooling and safety warning light bulb must be engaged, and milk-based scattering solutions must be prepared and calibrated. The Keplerian beam expander optics must be carefully aligned (see *Section 4.4.1*), followed by the Spatial Filter converging lens and aperture (*Section 4.4.2*). The scattering sample can then be imaged using the capture hardware and software (*Section 4.4.3*).

4.4.1 Beam expander optics

The Keplerian beam expander with pre-aperture is very similar in setup to the Galilean beam expander introduced previously for the AFA setups. The lens alignment procedures are identical for both. However, the pre-aperture is introduced at the beam cross-over point and must be carefully adjusted along all three axes to ensure that the aperture is positioned accurately.

First, the longitudinal position is adjusted so that the beam appears as small as possible on the surface of the aperture disc, and then the horizontal and vertical positions are adjusted so that the beam passes through the aperture. The correct positioning of the

aperture can be verified by observing the projected beam in real-time using the image sensor. Finally, the longitudinal position can be adjusted again to find the ideal position for the aperture. All of these adjustments are made while viewing the beam output from the beam expander on the live image from the image sensor.

4.4.2 Spatial Filter optics

The converging lens is first placed as near as feasible (approx. 2 cm) to where the exit face of the scattering sample will be during experiments. The converging lens must be autocollimated when both the scattering sample and the Keplerian beam expander with pre-aperture are not in place, so that the unexpanded beam is not interefered with. Once the converging lens is autocollimated, the beam expander can be installed, and the aperture can be positioned at the focal point of the converging lens, where the incoming collimated beam of light is focused down to a point. The procedure for accurately positioning the aperture is the same as that for positioning the pre-aperture in the Keplerian beam expander. The use of the image sensor to provide a live-image of the Spatial Filter output is invaluable in determining accurate aperture positioning.

4.4.3 Image capture procedures

In imaging with the SF system, a full 2-D image is captured at one time, unlike the AFA systems which require one row to be scanned at a time. In addition, the SF setup uses a different camera with a different software package (*SMX-M8x series* software). This software allows the exposure and gain of the image to be chosen and displays a live image from the image sensor, which can then be captured with a single command. The live image view also allows for the scattering sample to be correctly positioned before an image is captured. As with all imaging procedures, the exposure and gain must be set so as to prevent saturation.

4.5 Chapter summary

This section described the experimental procedures required for imaging experiments using the Argon laser AFA, 670 nm laser diode AFA, and Argon laser SF ADI systems.

First, the scattering sample preparation and calibration procedures for milk solution and biological tissue samples were discussed, followed by a discussion on the equations involved in calculating Scattering Ratio and observations on the time-sensitive nature of milk-based scattering solutions. Experimental overviews were given for each ADI setup, including descriptions of how the laser source, beam expander optics system, AFA with alignment jig or Spatial Filter, and image capture process are setup and utilized during imaging.

The following chapter presents prior work in AFA ADI for milk-based scattering solutions with the Argon ion laser.

Chapter 5

AFA ADI using an Argon Ion Laser

Argon laser AFA ADI experiments were conducted for milk-based scattering solutions using the Galilean spherical beam expander with resolution test objects at varying depths in the scattering medium [9]. This chapter reviews the Argon laser AFA setup using the standard Galilean beam expander and CSC thin line beam expander system. setups

5.1 Experimental results for Argon laser AFA ADI

The experiment setup for these results is identical to the setup used for the Argon laser AFA ADI work present in this thesis, except with a different image sensor. This older sensor (Texas Instruments – TC245) features a larger 8.5 µm (H) × 19.75 µm (V) pixel pitch and a smaller resolution of 751 (H) × 242 (V) pixels [28]. Because the pixels are not symmetrically square, images captured with this sensor were re-scaled to correct for distortion. The results presented in this section are taken from the author's undergraduate thesis work [9].

5.1.1 AFA ADI with Galilean spherical beam expander results

Figure 5-1 presents AFA ADI scans of the small (204 µm – 51 µm) resolution test objects placed at the front of 5 cm thick samples of deionized water and milk-based scattering solutions, ranging from SR = 0:1(water) to 2.2×10^6:1. The beam shaper employed for these results was a Galilean spherical beam expander (see Figure 3-3) which provided broad, circular illumination (approx. 2 cm in diameter) of the sample.

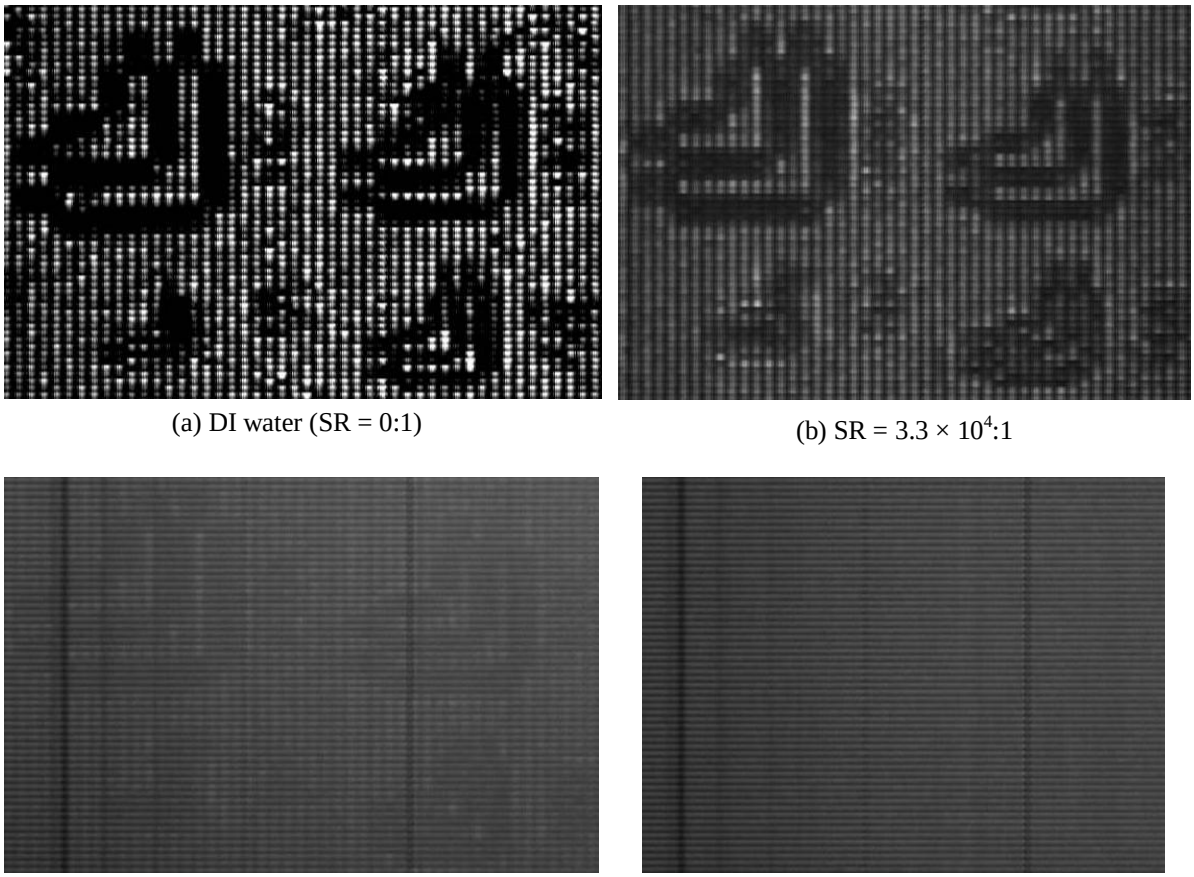

(a) DI water (SR = 0:1)

(b) SR = 3.3×10^4:1

(c) SR = 5.7×10^5:1

(d) SR = 2.2×10^6:1

Figure 5-1 Small test structures (204 µm – 51 µm) in the 5 cm (Front) position at λ = 488-514 nm from SR ~ 0:1 to 10^6:1.

Because the scans in the previous figure are underexposed, Figure 5-2 presents the same scans as the previous figure, but with *stretch contrast* enhancement automatically performed on the images using the open source image editing program, *GIMP*, to improve brightness and visibility.

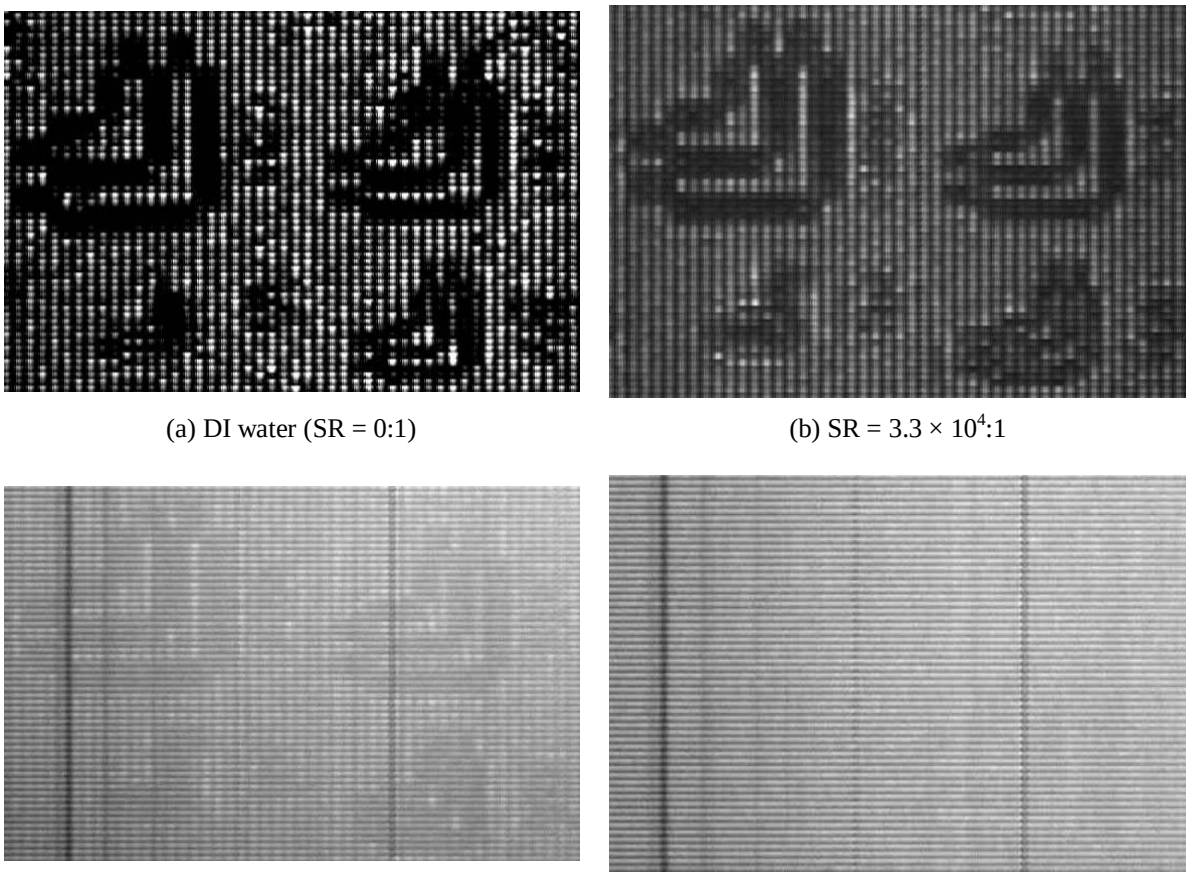

(a) DI water (SR = 0:1)

(b) SR = 3.3×10^4:1

(c) SR = 5.7×10^5:1

(d) SR = 2.2×10^6:1

Figure 5-2 Small test structures (204 µm – 51 µm) in the 5 cm (Front) position at λ = 488-514 nm from SR ~ 0:1 to 10^6:1 with *stretch contrast* enhancement.

Under no scattering conditions (Figure 5-2a), features as small as 102 µm are clearly resolvable in the second smallest test structure (bottom right of image), with high image contrast between the object and water. As the SR value is increased, contrast degrades and the smallest discernable feature size begins to increase. At SR = 3.3×10^4:1 and 5.7×10^5:1, the 102 µm lines and spaces are barely distinguishable, while the 153 µm-sized lines and spaces of the second largest test structure (top right) remain resolvable. At SR = 2.2×10^6:1, contrast degrades such that the test structures are no longer visible in the image. Thus, a Scattering Ratio of approximately 5:7 × 10^5 to 10^6:1 can be considered the scattering limit for this Argon laser AFA ADI setup, which utilizes a Galilean spherical beam expander for broad sample illumination.

Experimental results also showed that image contrast improves as test structures are moved further from the back of the scattering sample (i.e. closer to the AFA and sensor). A simple intensity measurement was conducted to measure the brightness of a dark area of a large test structure line (approx. 0.3 mm wide), with an ideal value of 0 out of 255 (i.e. black). These results were plotted on a graph with large test structures (357 µm – 204 µm) placed in five different depths in the scattering medium, and for four different scattering media, as shown in Figure 5-3.

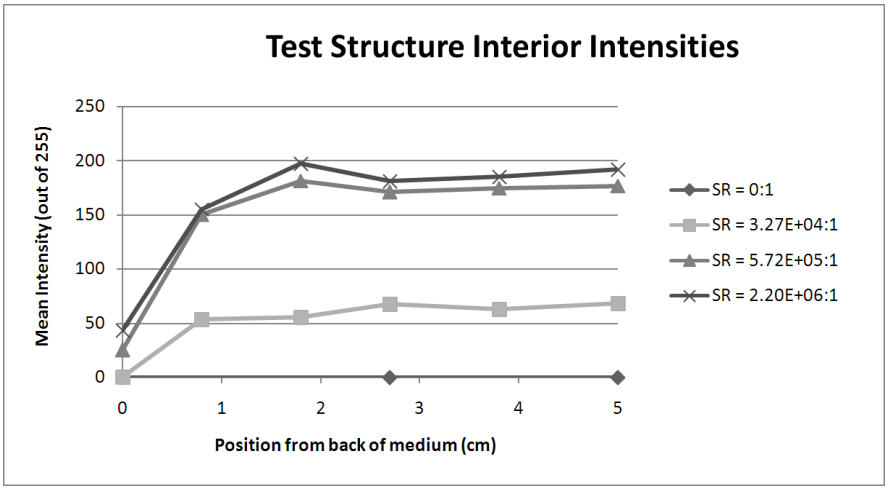

Figure 5-3 Measured large test structure line intensity vs. depth in the scattering medium.

These results show that test objects appear dark and opaque (high contrast) when placed at the very back of the scattering sample, but as test objects are moved forward in the sample, test structures lighten in the image (contrast degrades). This occurs because when test objects are placed at the back of the sample, no ballistic and quasi-ballistic light that reaches the center. However, as the test objects are moved further towards the front of the sample, ballistic and quasi-ballistic light passing the test object must travel through a certain thickness of scattering medium before reaching the AFA, and thus, a greater portion of that non-scattered light will become scattered. This trend can be observed until the test objects are moved approximately 36% of the distance (1.8 cm) towards the front of the sample, after which the contrast of the test objects appear to stay constant. Scans of large test structures placed 0 cm, 0.8 cm, 1.8cm, and 5 cm from the back of an SR = 2.2×10^6:1 sample are shown in Figure 5-4.

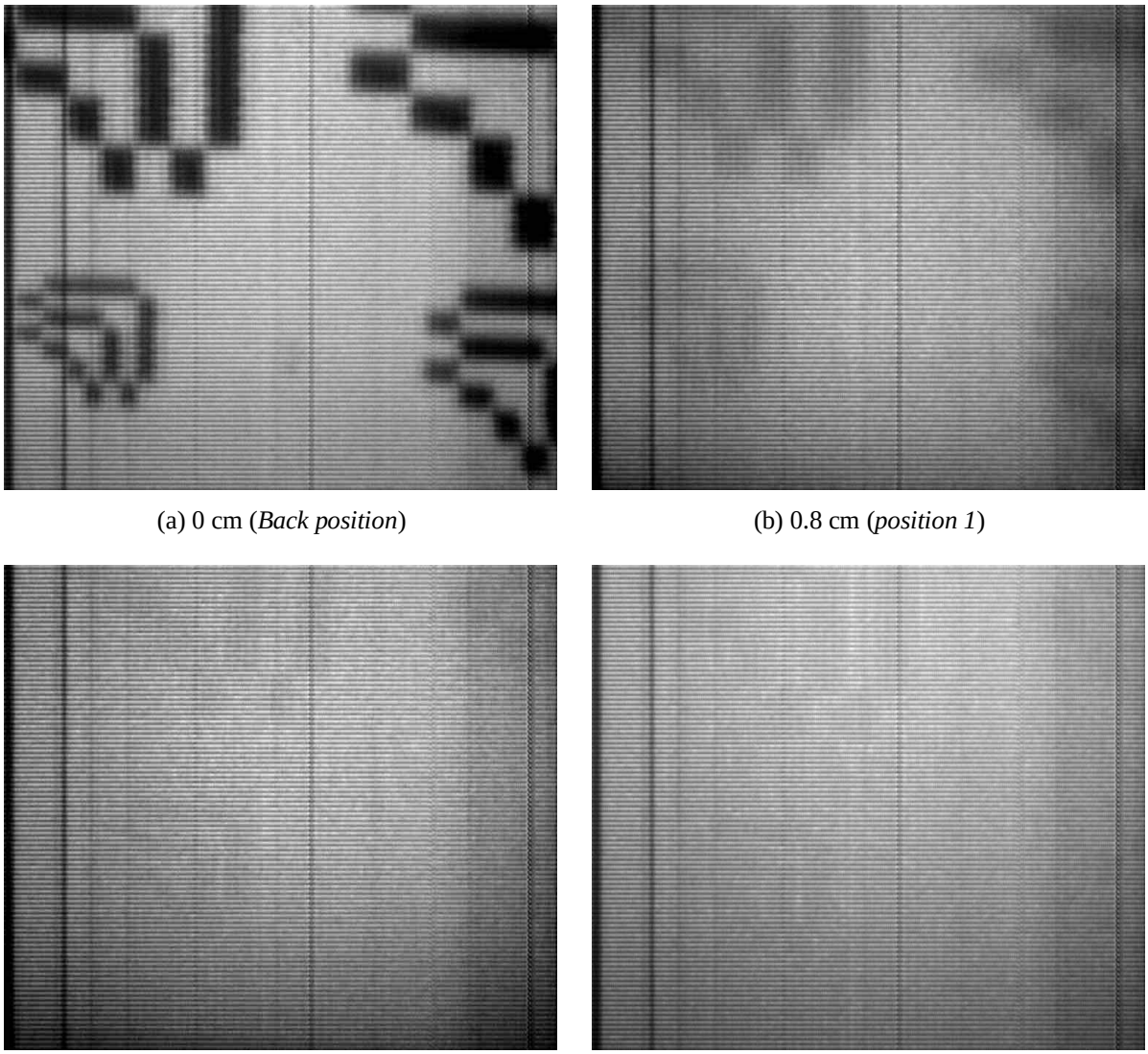

(a) 0 cm (*Back position*) (b) 0.8 cm (*position 1*)

(c) 1.8 cm (*position 2*) (d) 5 cm (*front position*)

Figure 5-4 Large test structures (357 µm – 204 µm) in varying positions at λ = 488-514 nm and SR = 2.2×10^6:1 *(stretch contrast enhanced)*.

As shown above, all the large (357 µm – 204 µm) test structures placed at the back position (i.e. 0 cm) display the highest contrast, with 204 µm wide lines and spaces resolvable (bottom left). As the distance is increased to 0.8 cm, the test structures lose contrast until 1.8 cm (and greater), where the test structures can barely be seen.

5.1.2 AFA ADI with CSC beam expander results

As was noted, confining the light to a narrow line near the microcollimator AFA has been shown to improve imaging. In this work, we first used a Cylindrical-Spherical-Cylindrical lens beam expander (see Figure 3-4), which shapes the beam into a thin line of light before illuminating the sample.

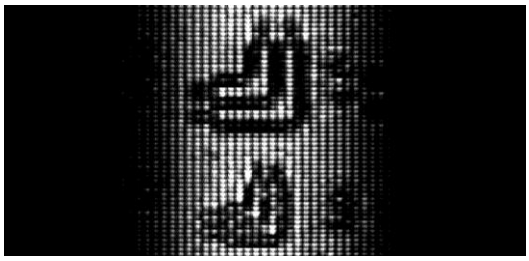

(a) DI water (SR = 0:1)

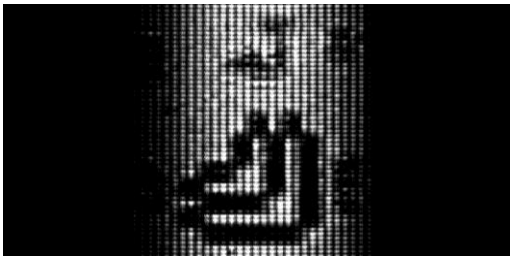

(b) DI water (SR = 0:1)

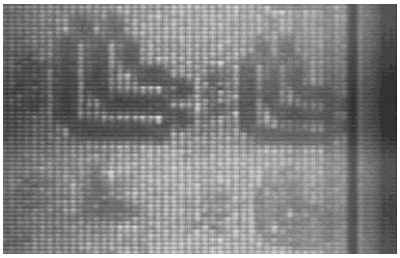

(c) SR = 4.8×10^6:1

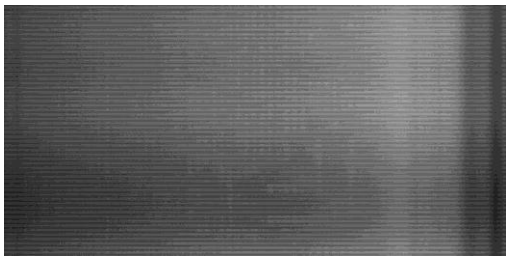

(d) SR = 1.7×10^8:1

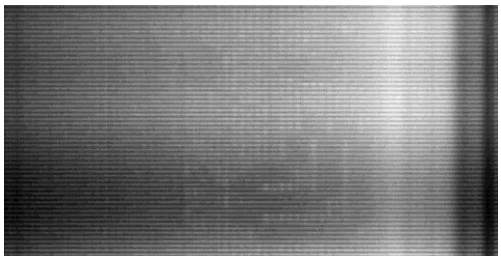

(e) *stretch contrast enh. version of (c)*

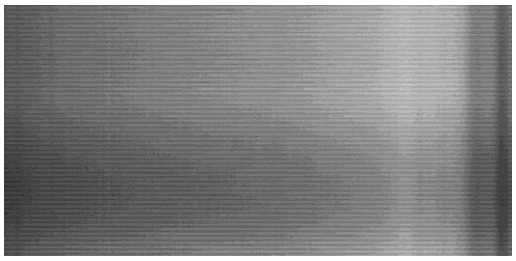

(f) SR = 1.0×10^9:1

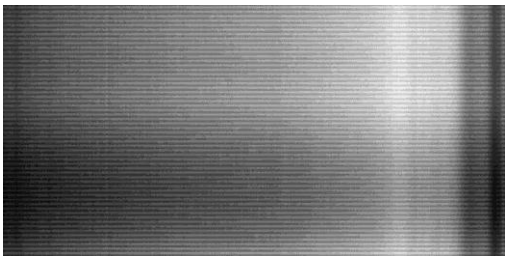

(g) *stretch contrast enh. version of (d)*

Figure 5-5 Small test structures (204 μm – 51 μm) in the 5 cm (Front) position at λ = 488-514 nm from SR ~ 0:1 to 10^9:1 using the CSC beam expander.

As shown by Figure 5-5, by reducing the illumination beam area from a circle approximately 2 cm in diameter (as in the case of the Galilean beam expander) down to a thin line of light approximately 0.13 mm in height, scattering media at SR values up to 10^8:1 can be imaged, which is approximately two orders of magnitude higher than the scattering limit with the Galilean spherical beam expander. When the entire scattering sample is illuminated, a large amount of scattered light is generated in all parts of the medium, with a small portion of that scattered light emerging with similar exit angles as non-scattered light in front of the AFA. This background scattered light will be collected by the sensor and contribute to imaging noise. Thus, by restricting the illumination area to only the small capture region directly in front of the AFA (see Figure 2-8), the background scattered light generated within the sample can be significantly reduced, resulting in a higher image signal-to-noise ratio.

For example, all the test objects can be detected at SR = 4.8×10^6:1, with individual 153 µm features resolvable (Figure 5-5c). This is an improvement over the Galilean beam expander setup which failed to show any test objects at the smaller SR of 2.2×10^6:1. At SR = 1.7×10^8:1, object features 204 µm in size can be faintly detected (bottom right, in Figure 5-5d and e) using the CSC thin line of light, whereas 10^6:1 appeared to be the scattering limit for the Galilean beam expander setup. At SR = 1.0×10^9:1 (Figure 5-5f and g), test objects are no longer clearly visible, and thus a Scattering Ratio of approximately 10^9:1 appears to be the limit for the CSC beam expander setup alone. Illumination can be further restricted by placing a vertical slit 1 mm in width in front of the sample to narrow the illumination area, as illustrated in Figure 5-6.

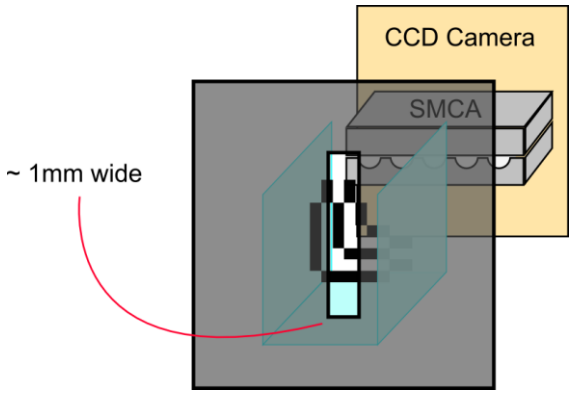

Figure 5-6 Illustration of a 1 mm-wide vertical slit.

Blocking off illumination to the left and right using the vertical slit further reduces background scattered light, but at the cost of a much narrower field of view during imaging, as demonstrated in Figure 5-7, which presents AFA scans taken using vertical slits of varying width [24].

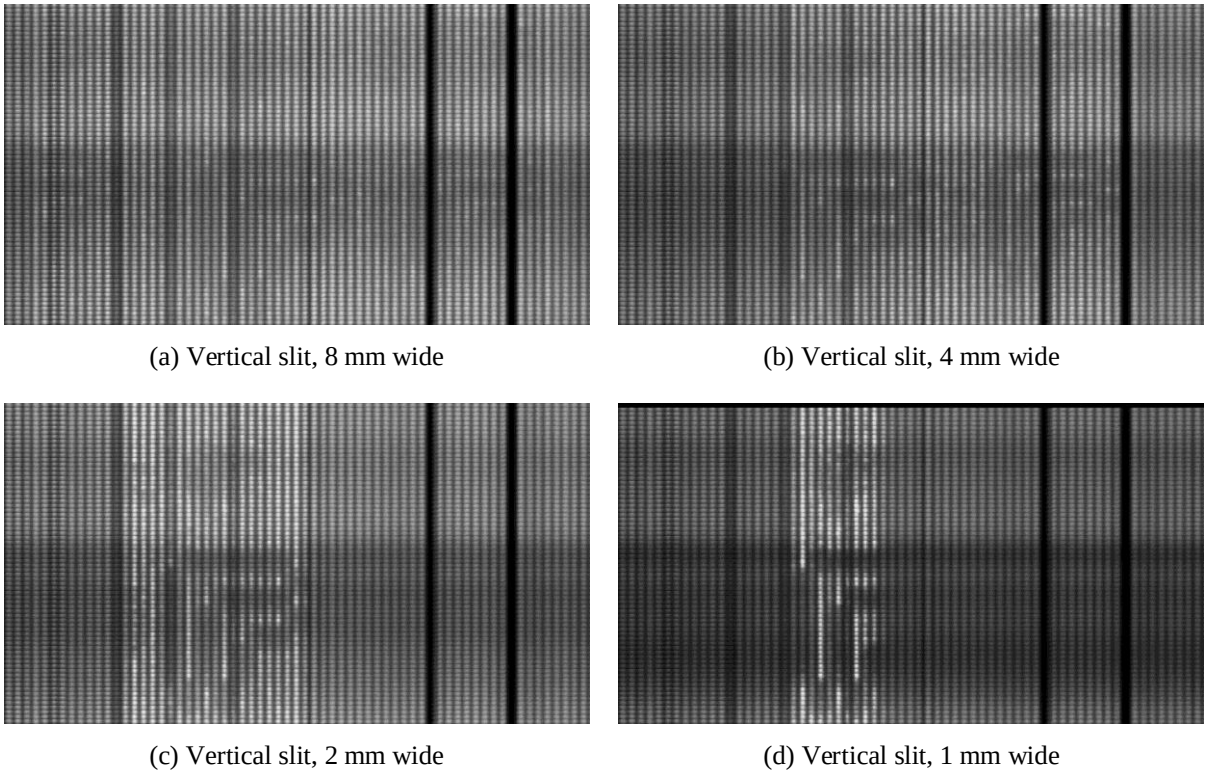

(a) Vertical slit, 8 mm wide

(b) Vertical slit, 4 mm wide

(c) Vertical slit, 2 mm wide

(d) Vertical slit, 1 mm wide

Figure 5-7 Small test structures (204 µm – 51 µm) in the 5 cm (front) position at λ = 488-514 nm at SR = 2.4×10^9:1 using the CSC beam expander and vertical slits of varying width.

As shown above, at a high SR value of 2.4×10^9:1, contrast improves steadily as the illumination beam is restricted to a narrow beam from 8 mm wide (Figure 5-7a) down to 1 mm wide (Figure 5-7d). This is clearly evident from the darkness of the 204 µm test structure lines, which are individually resolvable with the 1 mm wide slit. In addition, the smallest 52 µm test structure above the large test structure is detectable, although its lines and spaces are not individually resolvable. These results demonstrate an improvement in contrast from using the vertical slit over the previous SR = 1.0×10^9:1 scan with no vertical slit (Figure 5-5f and g), where no test structures were resolvable. It should also be noted that by taking multiple images using the narrow vertical slit (e.g. 1 mm wide) at different positions across the sample, a composite picture can be formed that allows for

the full width of the sample to be imaged, while still providing the contrast improvement gained from using a narrow slit [24].

Banding effects, where an entire row of the image is darkened in line with a large test structure line (especially visible in Figure 5-7d), occur with the use of a narrow vertical slit because of the thinness of the CSC-shaped beam. Because the beam is a thin line of light, when a large test structure line appears behind the vertical slit at the front of the sample, it blocks the illumination beam before it can enter the sample and become scattered throughout the medium. As a result, very little light enters the medium when that horizontal section is being scanned, and thus the background scattered light levels detected by the AFA and image sensor is low for that section.

5.2 Chapter summary

This chapter presented prior results from Argon laser AFA ADI experiments using the Galilean spherical beam expander and the CSC thin line beam expander systems. Image contrast was shown to degrade for both spherical and thin line beam expander setups as the Scattering Ratio of the sample was increased, with scattering limits of approx. 10^6:1 and 10^8:1, respectively, for detecting small test objects (204 µm – 51 µm). Experiments with the spherical beam expander setup demonstrated that test object image contrast decreases as they are brought from the back of the sample and away from the AFA and image sensor. At approximately 1.8 cm away from the back of the sample and further, image contrast appears to stabilize. Finally, restricting the illumination beam to a thin line of light has been demonstrated to reduce background scattered light and allow for higher SR media to be imaged. Further restricting illumination area with a 1 mm-wide vertical slit allows for the detection of 204 µm to 51 µm test structures at SR = 1.0×10^9:1 using the CSC beam expander.

The following chapter introduces trans-illumination ADI experiment results with the 670 nm laser diode AFA ADI system for milk-based scattering solutions and biological tissue samples.

Chapter 6

Angular Filter Array ADI with a 670 nm Laser Diode

This section presents imaging results for milk-based scattering samples with the 670 nm laser diode over a range of Scattering Ratios and object depths, and compares them to previous research conducted with the Argon laser. A discussion on the effects of diffraction on image resolution and performance is included. Biological tissue (chicken breast) samples are also imaged at several thicknesses (on the order of a few millimeters), with discussion and analysis of the results provided. Surface scattering effects between the tissue and glass interface are also investigated. The 670 nm laser diode experiment results presented in this chapter were carried out in joint collaboration with fellow researcher and PhD candidate Fartash Vasefi.

The Argon ion laser source provides good beam characteristics, such as high beam collimation and maximum peak power, which are useful for AFA ADI experiments with milk-based scattering solutions. However, biological tissues and organic materials exhibit high scattering at Argon ion wavelengths (488 – 514 nm) which makes imaging at those wavelengths challenging for biological samples. This is because biological samples (including milk and chicken tissue) exhibit lower scattering coefficients at longer wavelengths in the visible and near-infrared spectrum [15]. As a result, imaging at longer wavelengths makes it easier for biological tissue samples of moderate thicknesses (e.g. several millimeters or more) to be imaged, and eventually allow for applications in small animal and medical imaging.

Experiments with biological tissues at wavelengths of 670 nm are beneficial in moving from calibrated milk solution experiments at λ = 488-514 nm to ultimately medical or small animal imaging at red or near-IR wavelengths. To this end, a 670 nm laser diode has unique advantages over an Argon ion laser. In addition to lower μ_s in tissues at longer wavelengths towards the near-IR, the 670 nm laser diode also has the advantage of being small and low-power, which gives it greater portability and flexibility in the field. It is also a much lower cost system than a full-frame Argon laser (e.g. from tens of thousands

of dollars down to on the order of a thousand dollars). However, the 670 nm laser diode does have some drawbacks, specifically regarding its beam characteristics. In particular, it exhibits very high divergence that is asymmetric in character, and is also very difficult to shape into a thin, collimated beam.

The first trans-illumination Angular Filter Array ADI experiments using the 670 nm laser diode setup were conducted on milk-based scattering samples. Milk-based scattering samples are a consistent scattering medium, and thus allow for results from the 670 nm laser diode setup to be compared to the Argon laser (488-514 nm) scans from previous research. Biological tissue (chicken breast) imaging experiments were also conducted using the 670 nm laser diode source.

6.1 Milk-based scattering solution imaging with the 670 nm laser diode

6.1.1 Scattering Ratio changes at 670 nm

The absorption coefficient μ_a for biological samples such as milk-based scattering solutions is dependent on the wavelength of the illuminating light, with lower μ_a values for near-infrared and red wavelengths (e.g. eight times lower) when compared to the rest of the visible spectrum [29]. The reduced scattering coefficient μ_s' behaves similarly, and hence milk solutions were tested both at 670 nm and Argon laser (488-514 nm) wavelengths. Figure 6-1 and Figure 6-2 presents scattering measurements made for two batches of milk solutions with varying concentrations, one tested at Argon laser (488-514 nm) wavelengths and the other at the 670 nm wavelength.

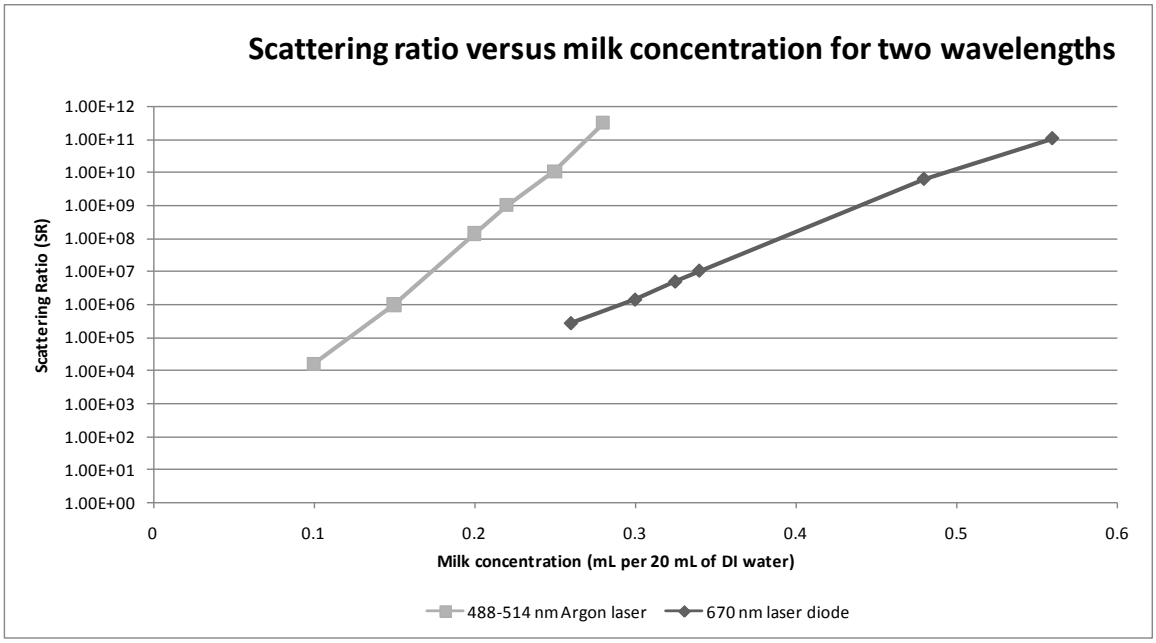

Figure 6-1 Scattering Ratio values for milk scattering solutions at Argon and 670 nm laser wavelengths.

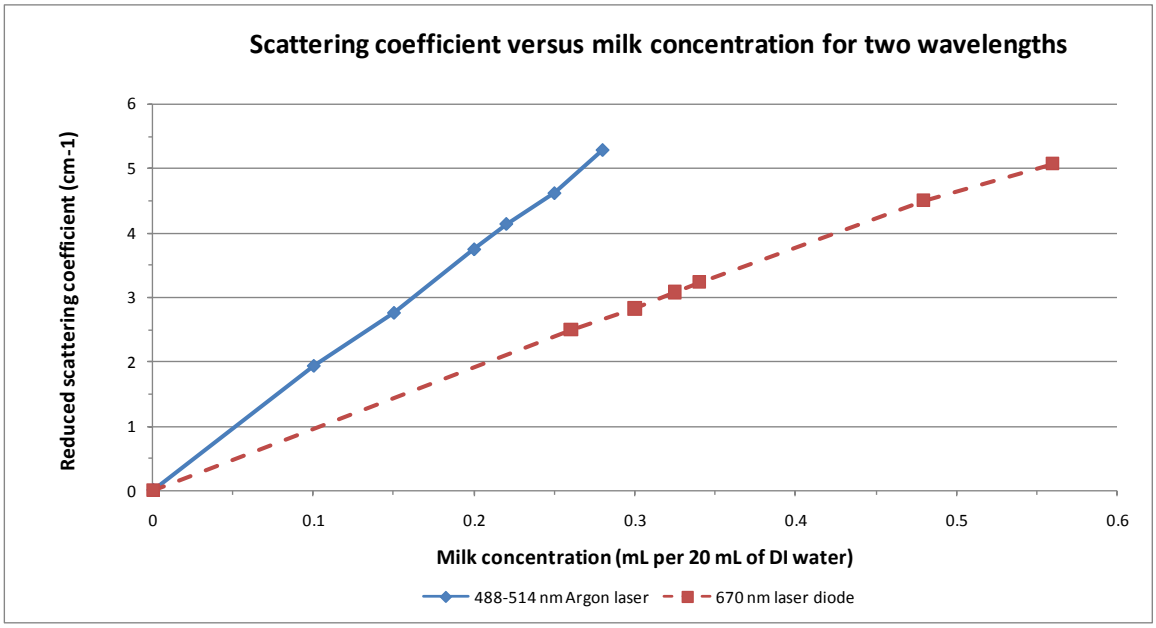

Figure 6-2 Scattering coefficients for milk scattering solutions at Argon and 670 nm laser wavelengths.

As shown in both figures, the same concentration of milk at Argon laser wavelengths results in much higher SR and μ_s' values as compared to the 670 nm laser diode. With the lines projected back to the origin (representing zero scattering), it is clearly evident that

the μ_s' slope for the Argon laser line is much greater than for the 670 nm laser diode [25]. For example, for a 0.26 mL / 20 mL concentration of milk, $\mu_s' = 2.50$ cm^{-1} for the 670 nm laser diode, while $\mu_s' \approx 4.65$ cm^{-1} for the Argon laser, which is an increase of approx. 1.9 times. These results confirm that milk-based scattering solutions exhibit much lower scattering as the wavelength is increased towards the NIR spectrum.

6.1.2 Imaging results with the 670 nm laser diode

The first experiments with the 670 nm laser diode were conducted to compare its imaging performance with previous results with the Argon laser (*Chapter 5*). Water scans are useful for comparison purposes because they provide a consistent baseline of imaging with no scattering. Figure 6-3 presents an image scan taken with 670 nm illumination of small test structures in 5 cm of water, while Figure 6-4 presents the same scan but with Argon ion (488-514 nm) light. Both scans are taken with the test structure slide placed at the front of the sample container (nearest to the incoming laser beam).

Figure 6-3 Small test structure (204 μm – 51 μm) scans in 5 cm of water (Front position) at λ = 670 nm.

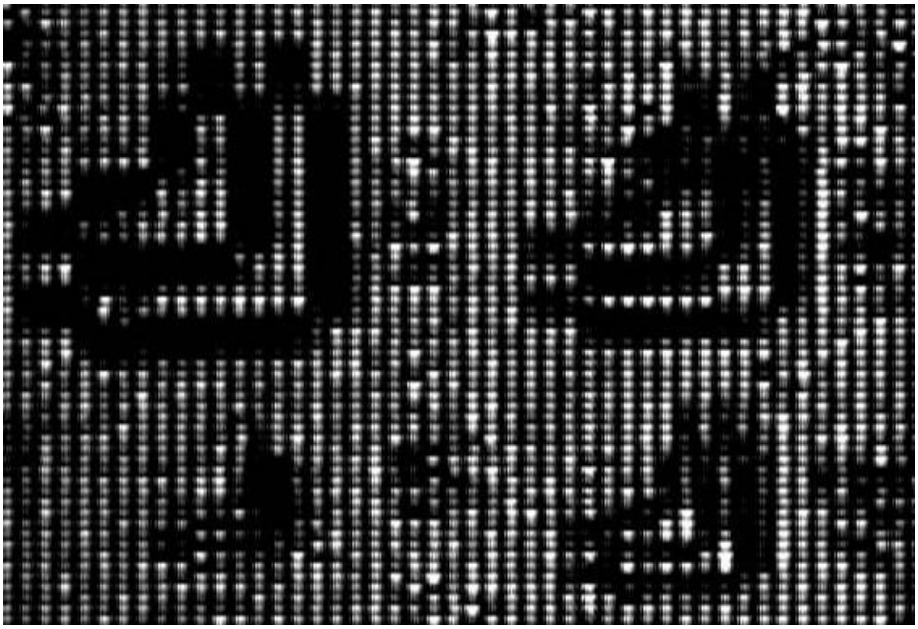

Figure 6-4 Small test structure (204 μm – 51 μm) scans in 5 cm of water (Front position) at λ = 488-514 nm.

The Argon laser image (Figure 6-3) shows better object edge definition as compared to the 670 nm laser diode image (Figure 6-4). In both these images, the lines and spaces of the three largest test structures (204 μm, 153 μm, and 102 μm) are resolvable while the

smallest (51 µm) test structure is detectable but not clearly resolvable. Also, the increased darkness within the test structure lines for the Argon laser scan shows greater signal.

Figure 6-5, shown as follows, plots out the pixel intensity line profile across a horizontal line of the 204 µm test structure. The intensity plots given in Figure 6-5 correspond to the area of the test structure that is shown circled, as sampled from top to bottom.

(a) Argon

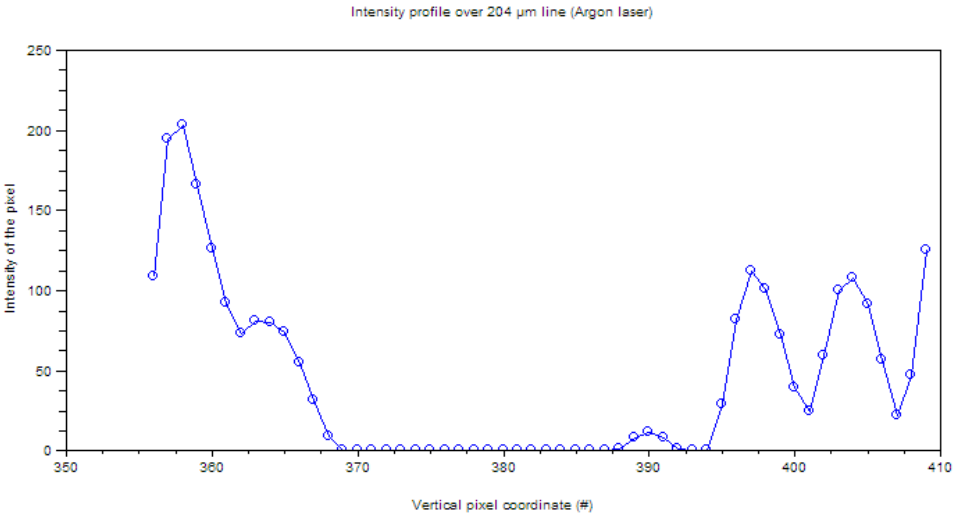

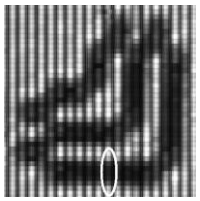

(b) 670 nm

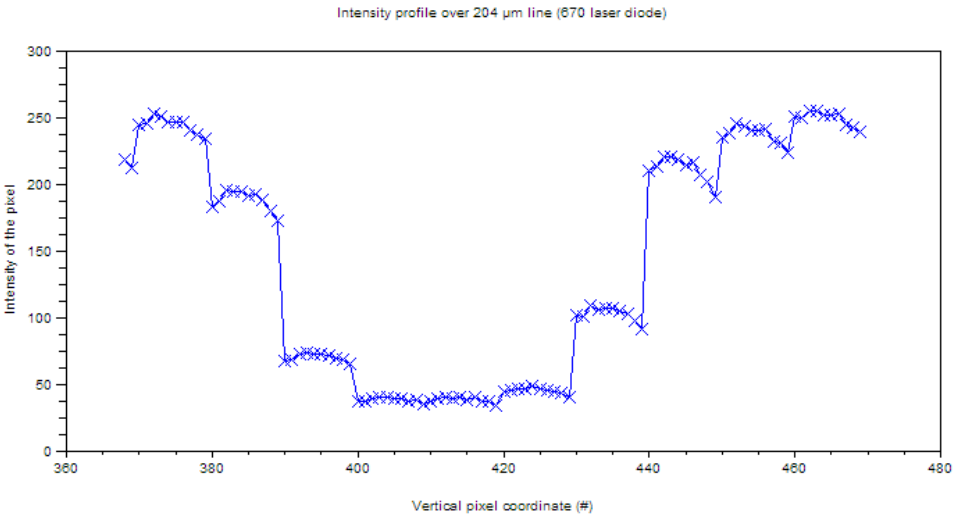

Figure 6-5 Intensity line profile for a 204 µm line in 5 cm water for the Argon and diode laser setups.

Contrast ratio *CR* is defined by the following formula,

$$CR = \frac{I_{\max} - I_{\min}}{I_{\max} + I_{\min}}, \qquad \textbf{Equation 6-1}$$

where I_{max} is the bright level and I_{min} is the dark level of the areas being measured, and with a *CR* of 1 being the maximum possible contrast and 0 being the minimum.

Figure 6-5 indicates that contrast is similar for both the Argon and 670 nm laser diode scans. In the Argon scan, the dark areas within the 204 µm test structure line is completely black (zero), and so *CR* = 1. In the 670 nm laser diode scan, the illuminated areas above and below the 204 µm line have intensities of approx. 250, with the dark region of the line reaching approx. 32, which results in a contrast ratio of 0.77. Thus, while contrast is high for both sets of results, the Argon laser image has a much higher contrast ratio. The line intensity plots also show that the Argon scan has slightly sharper slopes (-2.09 μm^{-1} vs. -1.46 μm^{-1}), which can be perceived in the image as sharp edges.

It is unexpected that the intensity of the dark 204 µm line is non-zero instead of completely black in the 670 nm image, since the scan was taken under zero scattering conditions. A potential explanation for this is that the 670 nm illumination beam, which is many times larger in area than the 204 µm lines, is not perfectly collimated, but exhibits some divergence or convergence within the beam cross-section. This could cause illumination from above or below the test structure line to cross over inside that region, causing it to appear partially illuminated. Further exploration should be conducted to determine whether beam divergence/convergence is a significant factor with this setup.

6.1.2.1 Diffraction effects at 670 nm

An important question is whether the longer 670 nm wavelength introduces significant diffraction effects. Diffraction can be a limiting factor in imaging performance for both the 670 nm laser diode and Argon ion laser setups. Diffraction will occur when light passes through a narrow slit or opening, such as a space between the test structure lines, assuming the slit size is sufficiently small relative to λ. Diffraction from the edges of the slit causes the light to be spread outwards in angle, and so diffraction effects are amplified over distance. For the test structures, diffusion can lead to the spreading and blurring of light by up to tens of microns when projected over a distance of 5 cm, which spills slightly over into the dark portions of the test structure. In addition, when two slits

are spaced closely together, interference patterns from coherent light can be formed because the two slits act as point sources which interfere with each other. Because the lines and spaces of the test structures are two orders of magnitude larger than the Argon and 670 nm wavelengths, diffraction effects are minimal for the largest test structures. In addition, the 670 nm laser diode has a relatively short coherence length (approx. 2 nm linewidth), which means that interference effects from a double slit would be minimal.

Another effect of increasing the wavelength to 670 nm is due to diffraction from the AFA tunnel openings. Light that is diffracted beyond a very small angle at the front of the AFA tunnels will be attenuated by the tunnel walls, while light diffracted at the end of the tunnels will spread out until reaching the image sensor. For a single slit opening, the projected illumination intensity I is related to angular spread θ according to Fraunhofer interference, which is described as follows,

$$I(\beta) = I_0\left[\frac{\sin(\beta)}{\beta}\right]^2, \qquad \textbf{Equation 6-2}$$

where $\beta = \frac{\pi \cdot b \cdot \sin(\theta)}{\lambda}$, b is the width of the opening, and λ is the illumination wavelength. The AFA tunnels have an estimated width and height of 51 µm and 17 µm, respectively, which results in the diffraction angle graph shown in Figure 6-7.

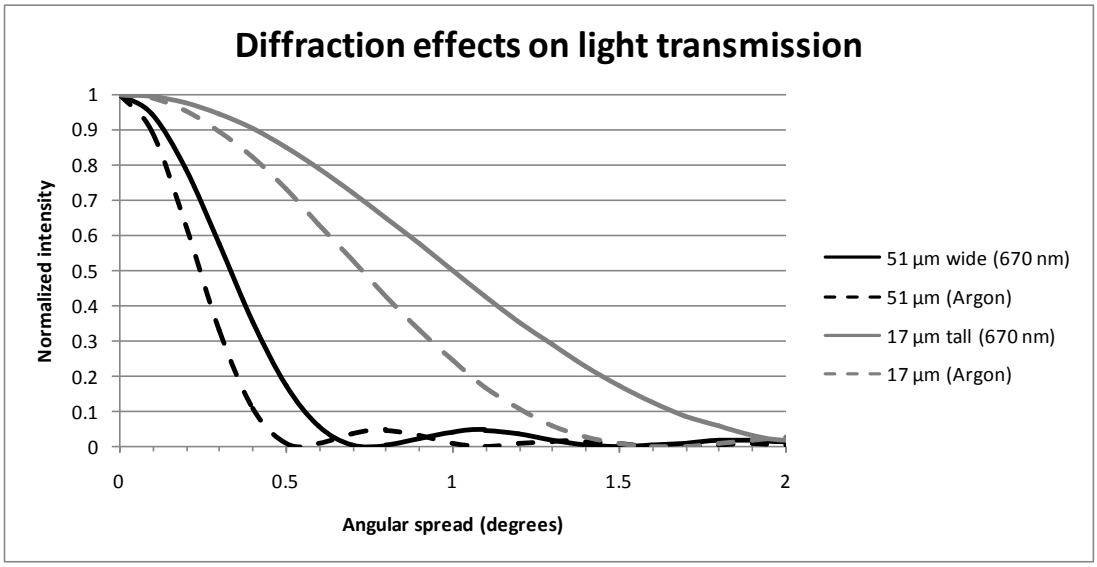

Figure 6-6 Theoretical angular spread due to diffraction from the AFA tunnel end at λ = 670 nm.

According to the formula for Fraunhofer interference, diffracted 670 nm light will spread horizontally and vertically by up to 0.7° and 2°, respectively, at which point the intensity falls to zero forming the first minimum (see Figure 6-6). Assuming a gap of approximately 2 mm between the tunnels and the image sensor, this results in a spread of approximately 49 µm horizontally and 140 µm vertically. Thus, the contribution of diffraction serves to spread out the light as it emerges from the tunnels, which may be the reason that light levels within each tunnel appear to be fairly uniform as opposed to showing finer image detail. At Argon laser wavelengths, the angular spread is smaller, reaching zero intensity at 0.6° (horizontal) and 1.6° (vertical), which corresponds to spreading of 42 µm and 111 µm, respectively.

In summary, while there are differences between the Argon laser and 670 nm laser diode scans in water, these images demonstrate that the 670 nm system provides similar baseline performance in water as previous research. The following subsections will explore the 670 nm system's performance under highly scattering conditions.

6.1.2.2 Varying the SR of the scattering medium

The following images examine the imaging performance of the 670 nm ADI system over a range of highly scattering conditions, with some comparison to previous Argon ADI results. Note that the exposure times t_{exp} given are for each individual line scan of the image (e.g. 10 pixels), with typically 75 lines or more making up each image. These exposure times do not include hardware and software overhead times between line scans.

(a) SR = 7.5×10^2:1, t_{exp} = 20 ms @ 1.77 mW

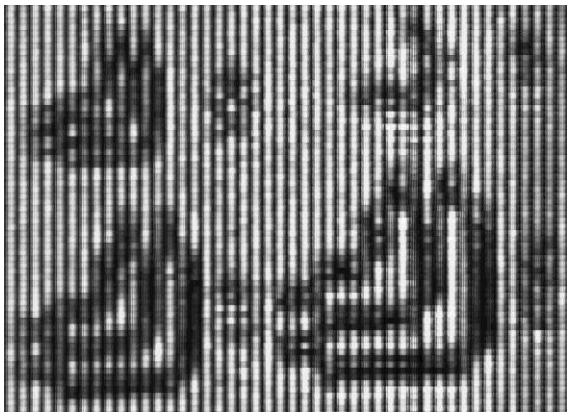

(b) SR = 1.5×10^4:1, t_{exp} = 35 ms @ 16.7 mW

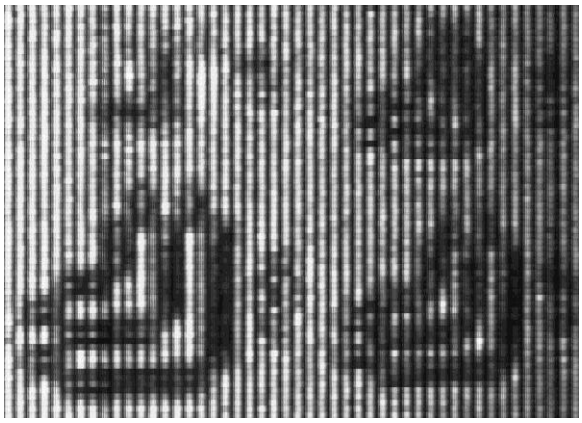

(c) SR = 1.3×10^5:1, t_{exp} = 15 ms @ 106 mW

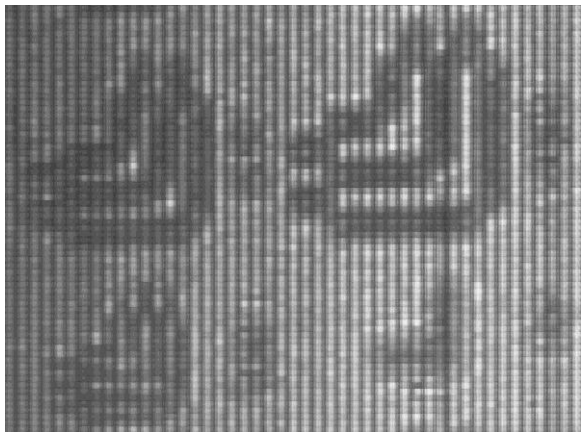

(d) SR = 1.4×10^6:1, t_{exp} = 40 ms @ 114 mW

Figure 6-7 Small test structures (204 μm – 51 μm) in 5 cm (Front) at λ = 670 nm from SR ~ 10^2:1 to 10^6:1.

Figure 6-7 shows 670 nm scans ranging from 10^2:1 to 10^6:1 in SR value. As SR is increased, the resolution of the test structure edges does not appear to degrade noticeably. However, contrast does degrade as the scattering level increases. Note that the contrast ratio of the largest 204 μm test structures decreases slightly as SR increases from 7.5×10^2:1 (CR = 0.80) to the 10^4 (CR = 0.73) and 10^5:1 (CR = 0.68) level. Contrast ratio degrades significantly by SR = 1.4×10^6:1 to CR = 0.33. These results at λ = 670 nm agree with previous Argon laser results that increased scattering level has a significant effect on signal-to-noise in the image (i.e. contrast), while having limited to no effect on image resolution.

In a highly scattering medium, almost all of the light is scattered off its original trajectory after multiple scattering events. As a result, there exists a small proportion of scattered light that will emerge with exit angles within the acceptance angle of the AFA, and thus, be passed through to the image sensor. This scattered light acts as noise in the image and decreases contrast because it is indistinguishable from the non-scattered light that bears useful information. However, as the scattering level increases, the amount of ballistic and quasi-ballistic photons falls until it declines below this background level. Thus, objects in the sample that should appear black (i.e. they block all non-scattered light) can appear partially illuminated (grey) because of the contribution of background scattered light that emerge behind an object. However, while contrast can be lowered significantly due to background scattered light, the resolution or edge definition of objects should not degrade significantly, even at high SR levels. For example, at SR = 1.4×10^6:1 (Figure 6-7d), image contrast appears very low while the edge definition is similar to scans taken at SR = 0:1 / water (Figure 6-3).

As shown in *Chapter 5* [2], [9], SR = 10^6:1 is at or near the limit of Argon ion laser ADI setups' capabilities for detecting small test structures (204 µm to 51 µm) when using a spherical beam expander and Angular Filter Array. The following images compare results in the range of SR = 10^6:1 for the 670 nm laser diode setup and the Argon laser (with spherical beam expander) setup.

670 nm laser diode **Argon ion laser**

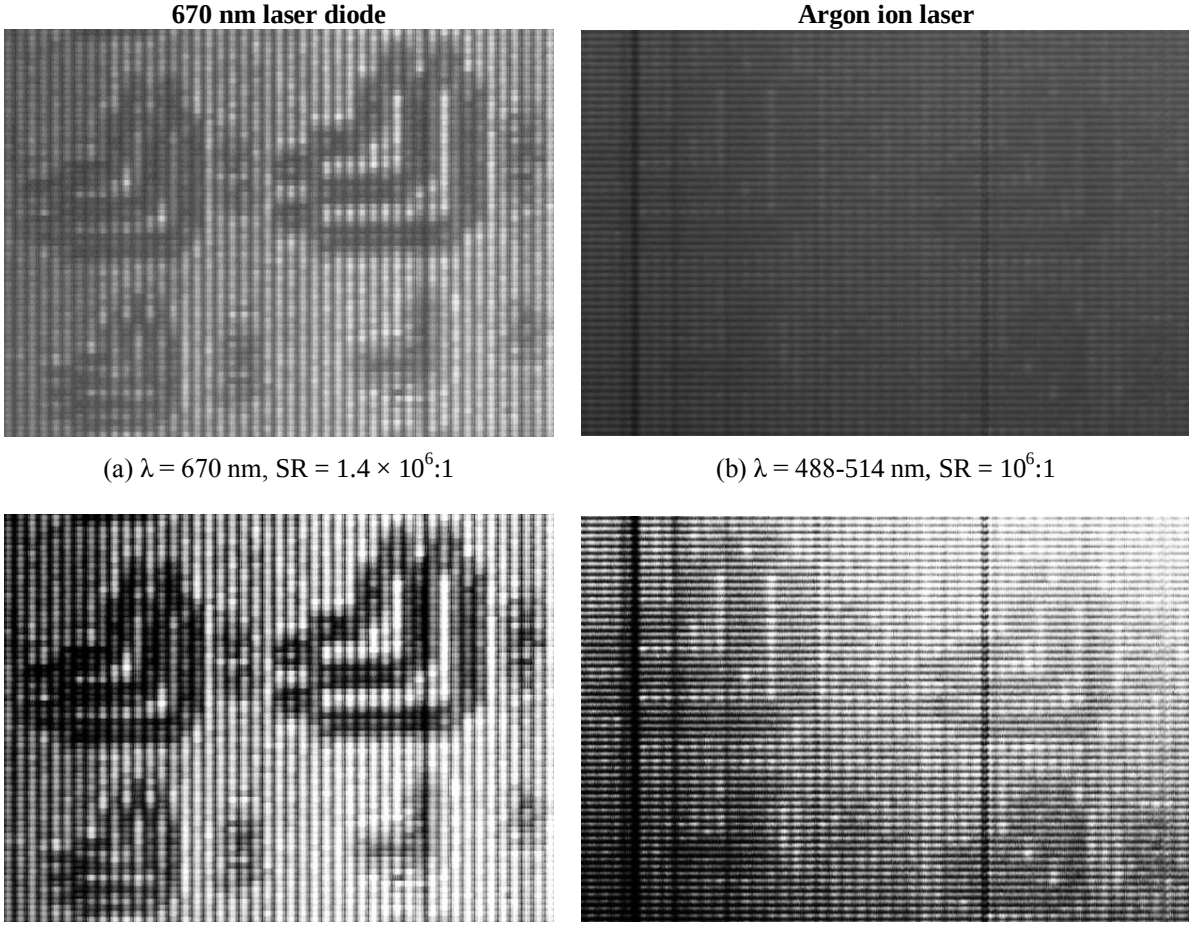

(a) λ = 670 nm, SR = 1.4 × 10^6:1

(b) λ = 488-514 nm, SR = 10^6:1

(c) *auto contrast enhanced version of (a)*

(d) *auto contrast enhanced version of (b)*

Figure 6-8 Small test structures (204 µm – 51 µm) in 5 cm (Front) at λ = 670 nm and 488-514 nm for SR ~ 10^6:1.

Figure 6-8 demonstrates that both the 670 nm and Argon laser (with spherical beam expander) setups are just barely capable of resolving small test structures at SR ~ 10^6:1. It is noteworthy that the 670 nm images exhibit higher contrast compared to the Argon laser images. For example, at λ = 670 nm (Figure 6-8a), the contrast ratio for the 204 µm lines is 0.33, while the contrast ratio for the corresponding Argon laser scan (Figure 6-8b) is virtually indiscernible. This difference in contrast can be attributed to the fact that the 670 nm illumination beam is shaped into an approx. 3.5 mm thick line of light, while the Argon laser is expanded into a much larger, circular beam of illumination. This 3.5 mm line is much taller than the Argon laser CSC line presented in *Section 3.2.1.2*. Hence, the SR limit for the 670 nm setup should be lower, as is seen.

Figure 6-9, shown as follows, presents images taken at higher SR values to determine the scattering limit for the 670 nm laser diode setup, as compared to images from the Argon laser with CSC beam expander. While both setups shape their illumination beams into a thin line of light, the Argon laser beam is shaped significantly more thinly (approx. 125 µm vertically) compared to the 670 nm laser diode beam (approx. 3.5 mm vertically), which helps reduced background scattered levels.

670 nm laser diode **Argon ion laser**

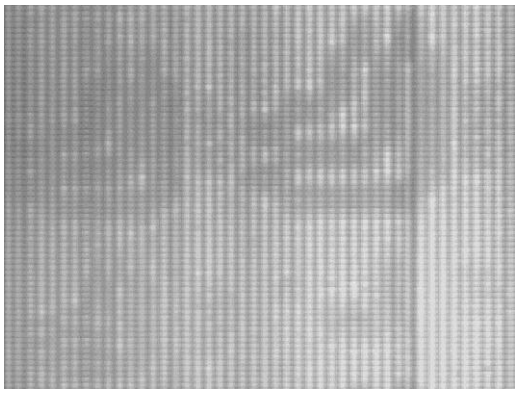

(a) λ = 670 nm, SR = 1.0×10^7:1, t_{exp} = *90 ms @ 117 mW*

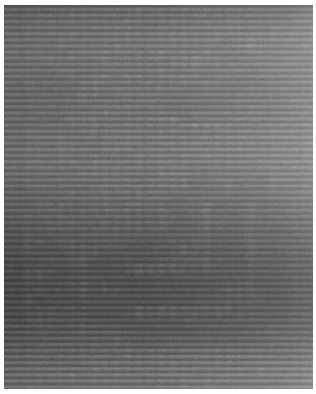

(b) λ = 488-514 nm (CSC expander), SR = 10^8:1

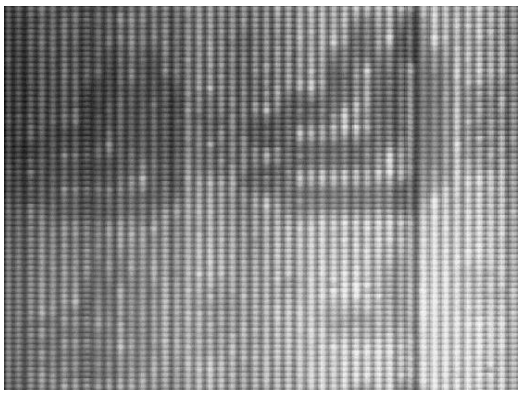

(c) *stretch contrast enhanced version of (a)*

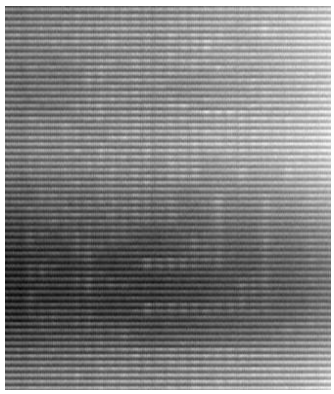

(d) *stretch contrast enhanced version of (b)*

Figure 6-9 Small test structures (204 µm – 51 µm) in 5 cm (Front) at λ = 670 nm and 488-514 nm at high SR values.

Figure 6-9 shows 670 nm laser diode scans at SR = 1.0×10^7:1 and Argon ion laser scans at SR = 10^8:1. For both setups, the 204 µm test structure lines and spaces are clearly resolvable, with the smallest test structure (51 µm) only faintly visible. The 153 µm lines

and spaces are visible in the 670 nm scans, with the 102 µm test structure exhibiting interference-like artefacts as discussed previously.

While the Argon laser setup is able to resolve images at a Scattering Ratio of 10^8:1, the 670 nm laser diode setup is limited to an SR of approximately 1.0×10^7:1, which appears to be the scattering limit for the current 670 nm setup. For a higher SR of 10^8:1, Figure 6-10 shows that the current setup is unable to resolve any test structures (204 µm or smaller) in the image.

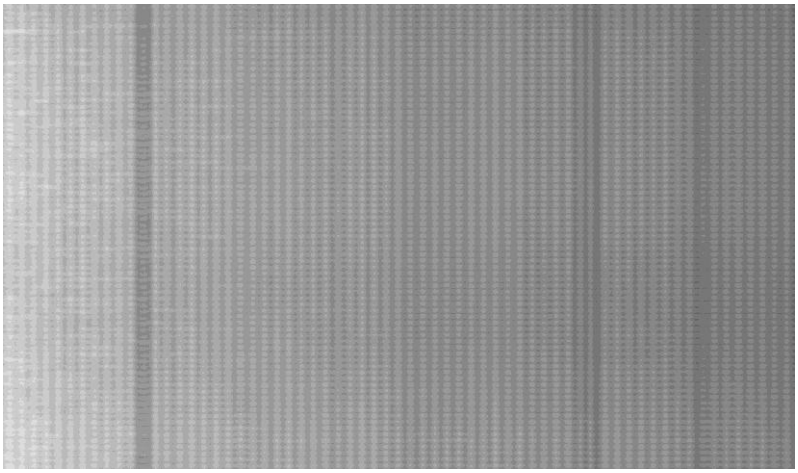

Figure 6-10 Small test structures (204 µm – 51 µm) in 5 cm (Front) at $\lambda = 670$ nm and SR = 9.9×10^7:1.

Based on previous research, it is expected that further thinning of the 670 nm illumination beam will improve contrast and allow for higher SR's to be imaged. A thinner line could be achieved similarly to the CSC beam expander (for the Argon laser), by using a spherical and cylindrical lens to converge and re-collimate the beam vertically. Another technique for increasing contrast and image performance at high SR's is through the use of digital signal processing (DSP) image techniques. Work on this project by SFU student Fartash Vasefi has shown the reduction the background scattered light through the use of digital image processing and optical techniques [21], [30].

In summary, experiments with the 670 nm laser diode setup with milk-based scattering solutions of varying SR values demonstrate performance falling in between previous Argon laser results with the spherical beam expander and the CSC beam expander. These

results indicate that illumination beam thinness is a dominant factor in imaging performance, as the 670 nm system features an illumination beam that is in between the spherical beam expander and CSC beam expander in thickness.

6.1.2.3 Varying depth in the scattering medium

At the 5 cm (front) position and λ = 670 nm (Figure 6-8), an image artefact is visible for the 102 µm test structure with SR = 1.4×10^6:1. Instead of the three flat horizontal lines in the test structure, it appears that four horizontal lines are shown in the image. A line intensity plot across the 102 µm test structure is given in Figure 6-11.

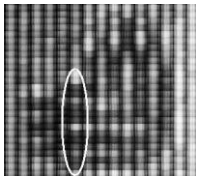

(a) 102 µm, 5 cm position

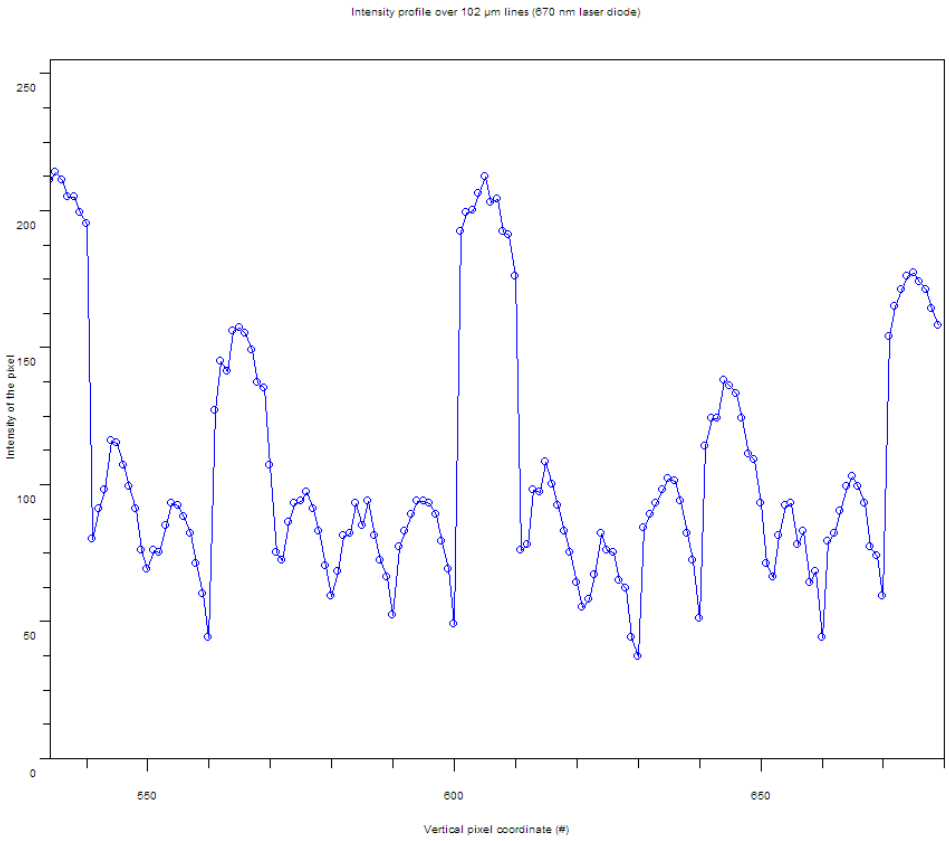

Figure 6-11 Intensity line profile for 102 µm lines in the 5 cm position for SR = 10^6:1 and λ = 670 nm.

As shown in Figure 6-11, four dark bands are clearly evident, which indicates 4 lines. Because there are only 3 lines in the actual test structure, this visual artefact may be a result of double slit interference. For a double slit, the projected illumination intensity *I* is

related to angular spread θ according to the following formula (very similar to Equation 6-2),

$$I(\beta) = I_0 \left[\frac{\sin(\beta)}{\beta} \right]^2 \left[\frac{\sin(n\gamma)}{\gamma} \right]^2, \qquad \textbf{Equation 6-3}$$

where $\beta = \frac{\pi \cdot b \cdot \sin(\theta)}{\lambda}$, $\gamma = \frac{\pi \cdot d \cdot \sin(\theta)}{\lambda}$, b is the width of the opening, d is the spacing between the openings, and λ is the illumination wavelength. This formula gives the interference intensity plot shown in Figure 6-12. In actuality, the 102 µm lines do not truly form a double slit because the outer edges are illuminated (instead of continuing on as a baffle). Therefore, this formula is only an approximation of the actual optical behaviour.

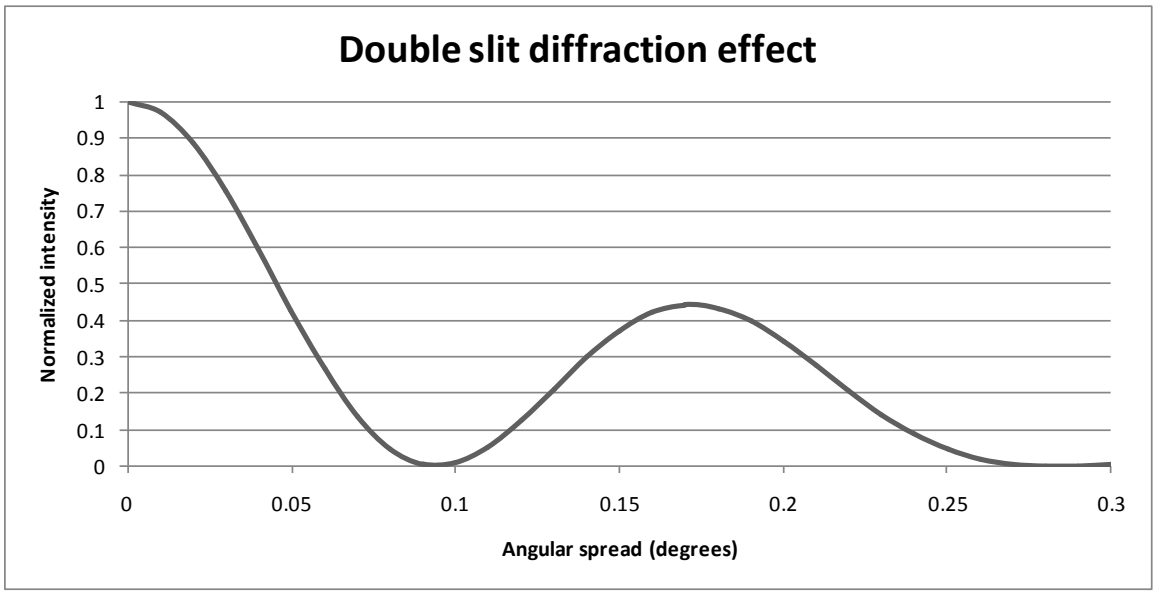

Figure 6-12 Theoretical angular spread (one-sided) due to interference from 102 µm slits spaced 204 µm apart at λ = 670 nm.

Figure 6-12 shows a one-sided profile of the diffraction pattern from the double slit formed by the 102 µm test structure. As calculated from this plot, if the AFA is 5 cm away from the test structure, up to four dark lines should be visible, each spaced approx. 180 µm apart (compared to 204 µm spacing for the actual test structure). This analysis is only preliminary, as diffraction effects should theoretically be minimal since slits of

102 µm and spacings of 204 µm in size are still two orders of magnitude greater than the wavelength.

Previous Argon AFA experiments in *Section 5.1.1* [9] have demonstrated that placing the test objects further back (towards the image sensor) in the scattering medium improves image contrast and definition. The following experiments were undertaken to determine if the same behaviour can be observed for the 670 nm laser diode setup.

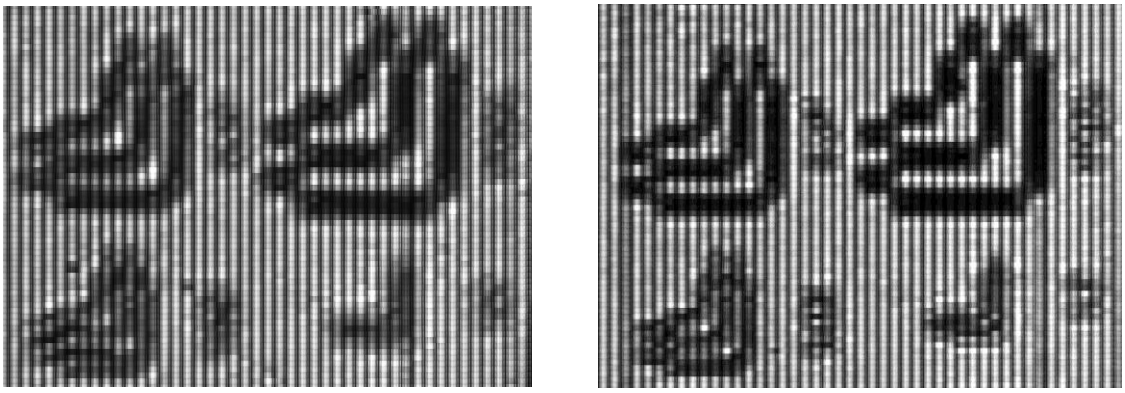

(a) Front position (5 cm) (b) Middle position (2.7 cm)

Figure 6-13 Small test structures (204 µm – 51 µm) at front and near-middle positions in 5 cm water at $\lambda = 670$ nm.

Figure 6-13 presents two scans taken with no scattering in a 5 cm deep water sample. The first scan (Figure 6-13a) was taken with the entire water sample (5 cm) between the test objects and the image sensor, and the second (Figure 6-13b) was taken with just over half of the water sample (2.7 cm) in between the objects and sensor. Even though there is no scattering of light, the first image is very slightly blurrier as compared to the second image, due to the increased distance from the test objects to the image sensor. Line intensity profiles across the bottom horizontal line of the 204 µm test structure are virtually identical in contrast and edge sharpness. However, line intensity profiles across the horizontal lines of the smaller 102 µm test structures exhibit greater differences, as shown in Figure 6-14.

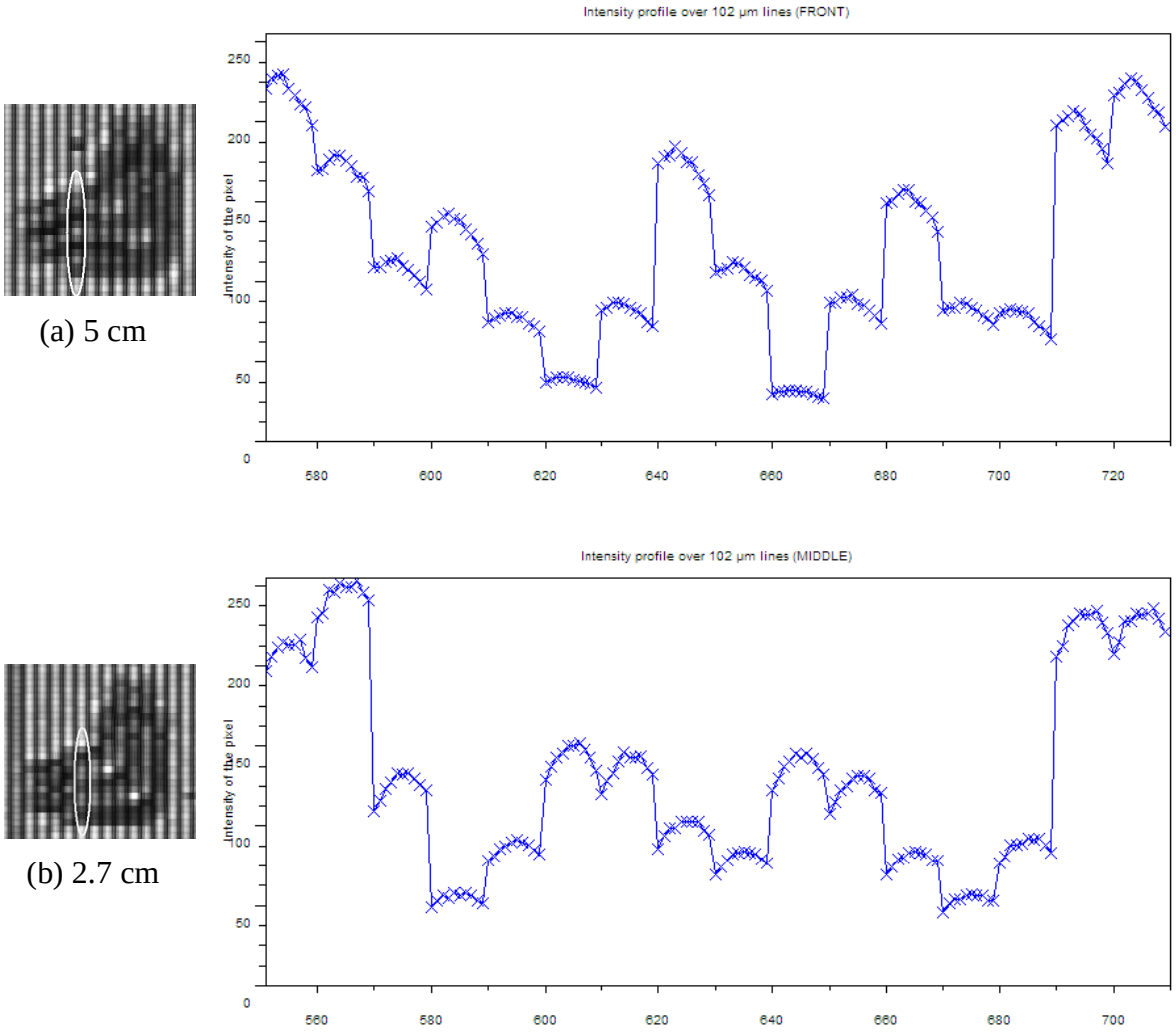

Figure 6-14 Intensity line profile for 102 µm lines in 5 cm and 2.7 cm water with $\lambda = 670$ nm.

As shown above, four valleys appear in the line profile plot for the front position (Figure 6-14a), while the expected three valleys appear for the middle position plot (Figure 6-14a). These results reconfirm the observation that interference-like effects are exhibited when the test structures are placed 5 cm from the AFA. However, as the distance between the test structures and AFA is reduced by approximately half, this phenomenon appears to subside and the correct number of horizontal structure lines reappear in the image. Furthermore, further investigation should be conducted into the nature of the interference-like effect, as gaps and spaces on the order of a hundred microns are expected to produce only minimal diffraction.

The following figure presents scans with test objects in the front and middle positions at SR = 1.0×10^7:1.

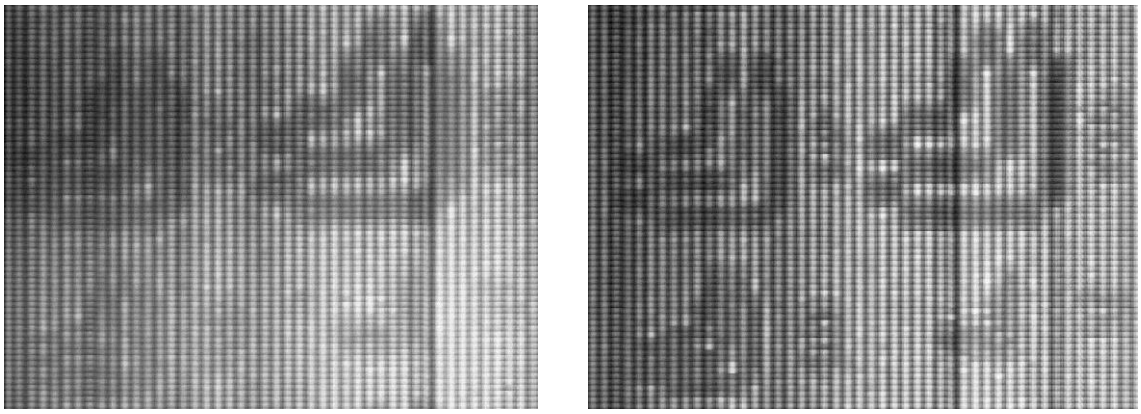

(a) Front position (5 cm), *stretch contrast enhanced* (b) Middle position (2.7 cm), *stretch contrast enh.*

Figure 6-15 Small test structures (204 µm – 51 µm) at front and near-middle positions at λ = 670 nm and SR = 1.0×10^7:1.

Figure 6-15 illustrates that middle position scans of 204 µm to 51 µm test structures in a highly scattering medium have similar resolution and slightly higher image contrast compared to front position scans. From line intensity plots across the 204 µm test structures, shown in Figure 6-16, the horizontal lines appear with a contrast ratio of approx. 0.36 for the 5 cm position, and 0.45 when the test structures are brought to the 2.7 cm position.

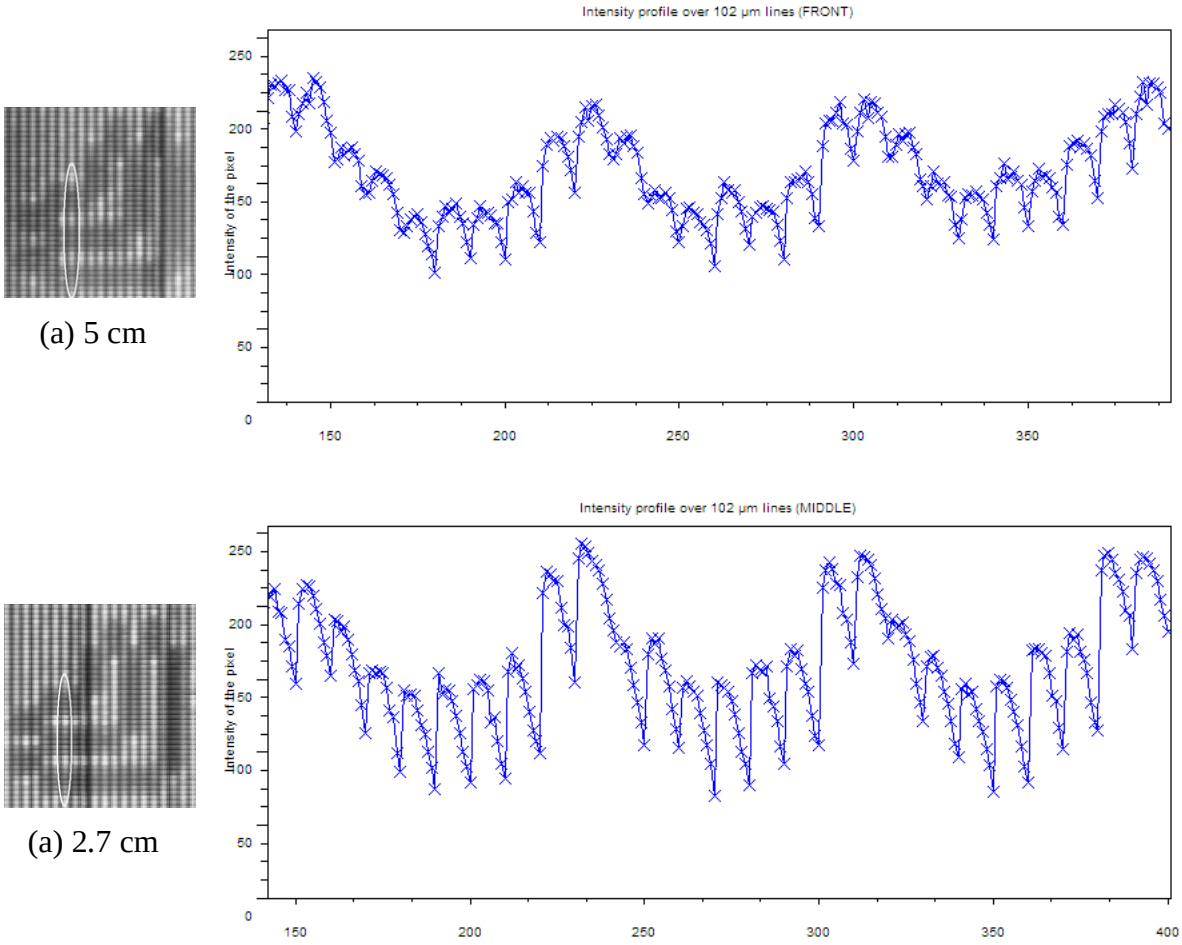

Figure 6-16 Intensity line profile for a 204 µm line in the 5 cm and 2.7 cm positions at SR = 1.0×10^7:1 and $\lambda = 670$ nm.

Results with test structures at varying depths demonstrate interference like effects are reduced when the distance between test objects and the AFA is decreased. In addition, these results confirm that image contrast improves slightly when test objects are brought from the front (5 cm) to the middle (2.7 cm) position of the scattering medium, which agrees with previous Argon laser ADI research.

6.2 Chicken breast tissue imaging with the 670 nm laser diode

Because biological tissues exhibit much lower scattering and absorption levels for infrared and NIR wavelengths, the 670 nm laser diode is much better suited than the Argon ion laser for biological tissue scans. Commercially available chicken breast is used

as the biological tissue for transillumination ADI experiments. The tissue is sectioned using a scalpel and compressed between two glass microscope slides using firm pressure, with minimal reduction in sample thickness (on the order of a millimeter) [25]. The glass slides are then secured together under pressure using tape, as illustrated below in Figure 6-17. Samples can be prepared at various thicknesses (after compression) in the range of one millimeter to several centimetres.

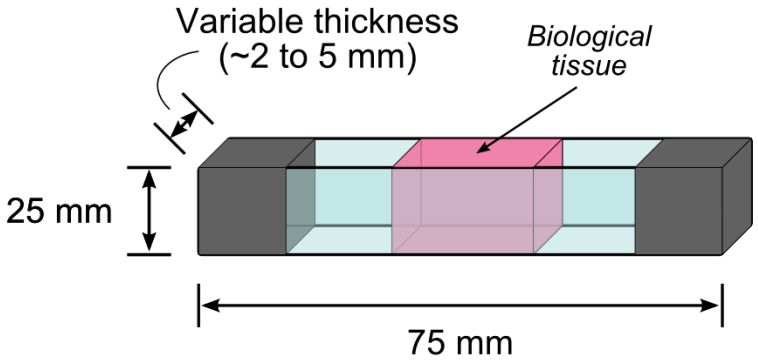

Figure 6-17 Illustration of a biological tissue sample.

Figure 6-18 presents a photograph of a chicken breast tissue sample as prepared for ADI experimentation.

Figure 6-18 Photograph of a chicken breast tissue sample.

6.2.1 Chicken breast tissue scans with non-uniformity comparison

The imaging performance and resolution limits for 670 nm laser diode AFA imaging of chicken tissue samples is explored in this section. The following three figures present

scans of chicken breast tissue with thicknesses of approx. 1.2 mm, 2.7 mm, or 3.8 mm, either with no test structures (tissue only) or with 204 µm to 51 µm test structures.

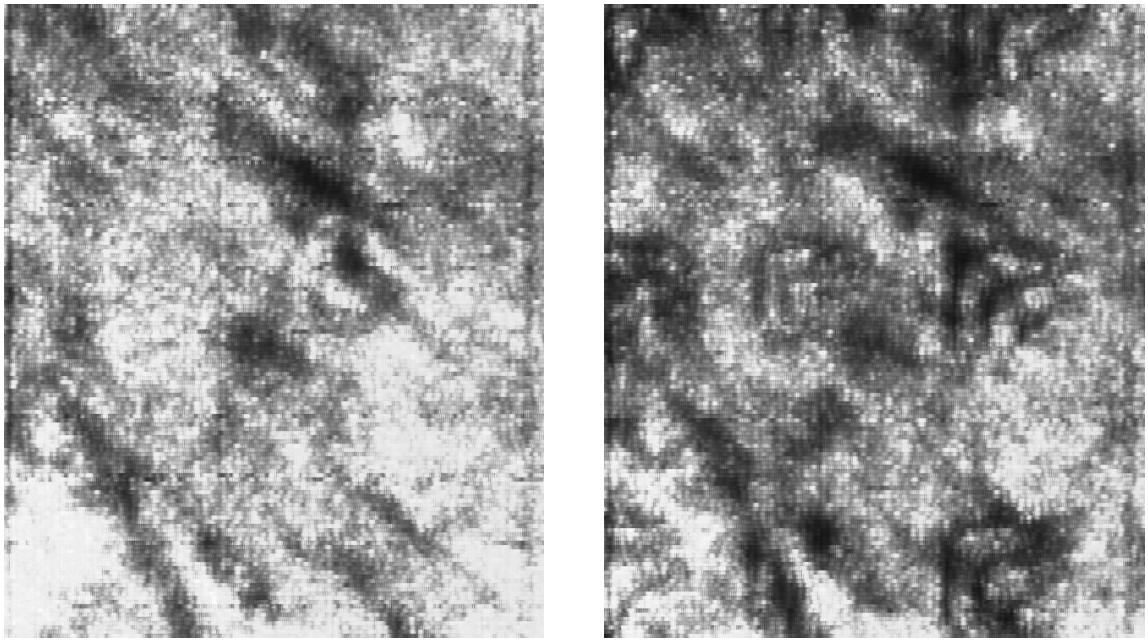

(a) Tissue only (b) Tissue with small test structures

Figure 6-19 Small test structures (204 µm – 51 µm) at λ = 670 nm in front of ~1.2 mm chicken breast tissue.

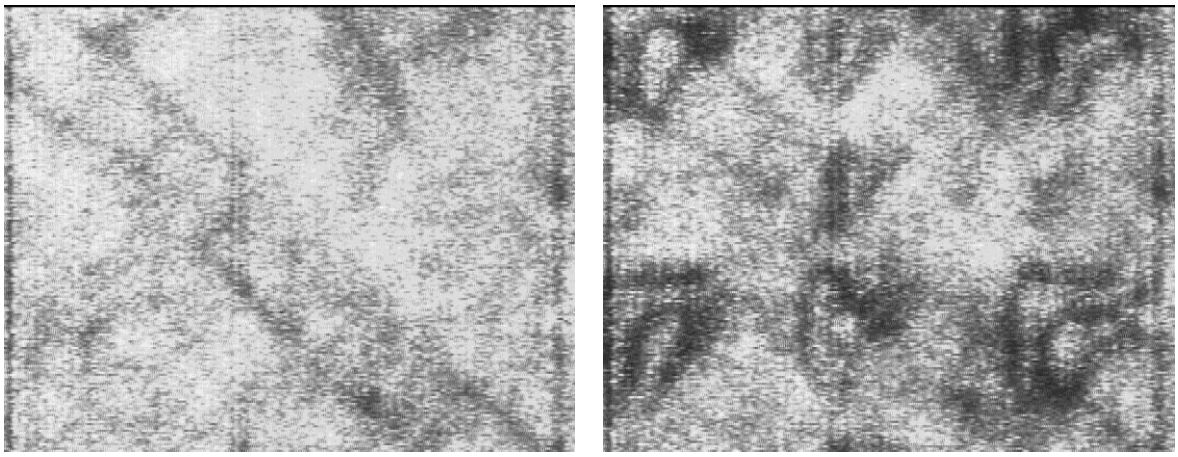

(a) Tissue only (b) Tissue with small test structures

Figure 6-20 Small test structures (204 µm – 51 µm) at λ = 670 nm in front of ~2.7 mm chicken breast tissue.

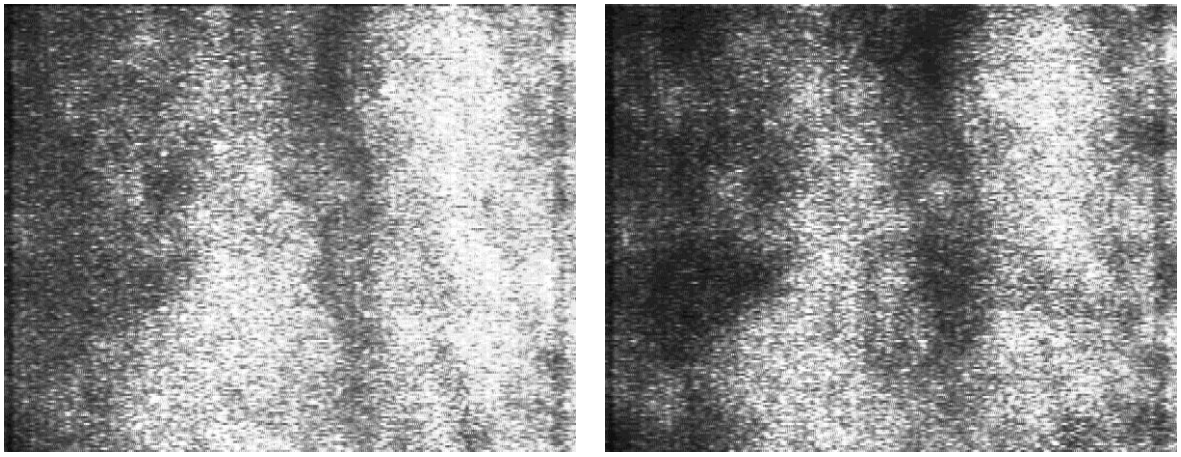

(a) Tissue only (b) Tissue with small test structures

Figure 6-21 Small test structures (204 μm – 51 μm) at λ = 670 nm in front of ~3.8 mm chicken breast tissue.

The tissue only scans indicate the presence of many non-uniformities from within to the tissue. For example, Figure 6-19a, Figure 6-20a, and Figure 6-21a show much unevenness brightness and many occlusions in the image, which may represent characteristics of the tissue such as fat deposits, etc. When compared to milk scattering solutions, it is evident that chicken tissue is not a homogenous medium and contains many non-uniformities that can obscure test structures during imaging. However, in applications such as medical imaging, these non-uniformities may actually correspond to features of the tissue that are supposed to be in the image, instead of artificial test objects. Thus, the fact that these tissue non-uniformities appear in our imaging tests may prove beneficial in future biomedical applications.

The following section analyzes the imaging and resolution performance for tissue scans with the small test structures.

6.2.2 Imaging and resolution performance

Figure 6-22 presents the ~1.2 mm chicken tissue sample scan, with the largest test structure (204 μm) clearly labeled.

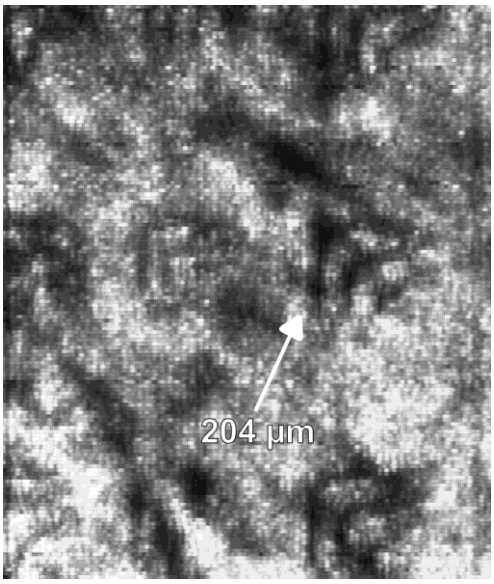

Figure 6-22 Small test structures (204 µm – 51 µm) at λ = 670 nm in front of ~1.2 mm chicken breast tissue.

The previous scan shows that the largest two test structures (204 µm and 153 µm) are visible, with most of the lines and spaces individually resolvable for each. However, the 102 µm and 51 µm test structures are not clearly detectable in the image. These results demonstrate partial resolution of features sized 204 µm and 153 µm when imaging ~1.2 mm chicken breast tissue at λ = 670 nm.

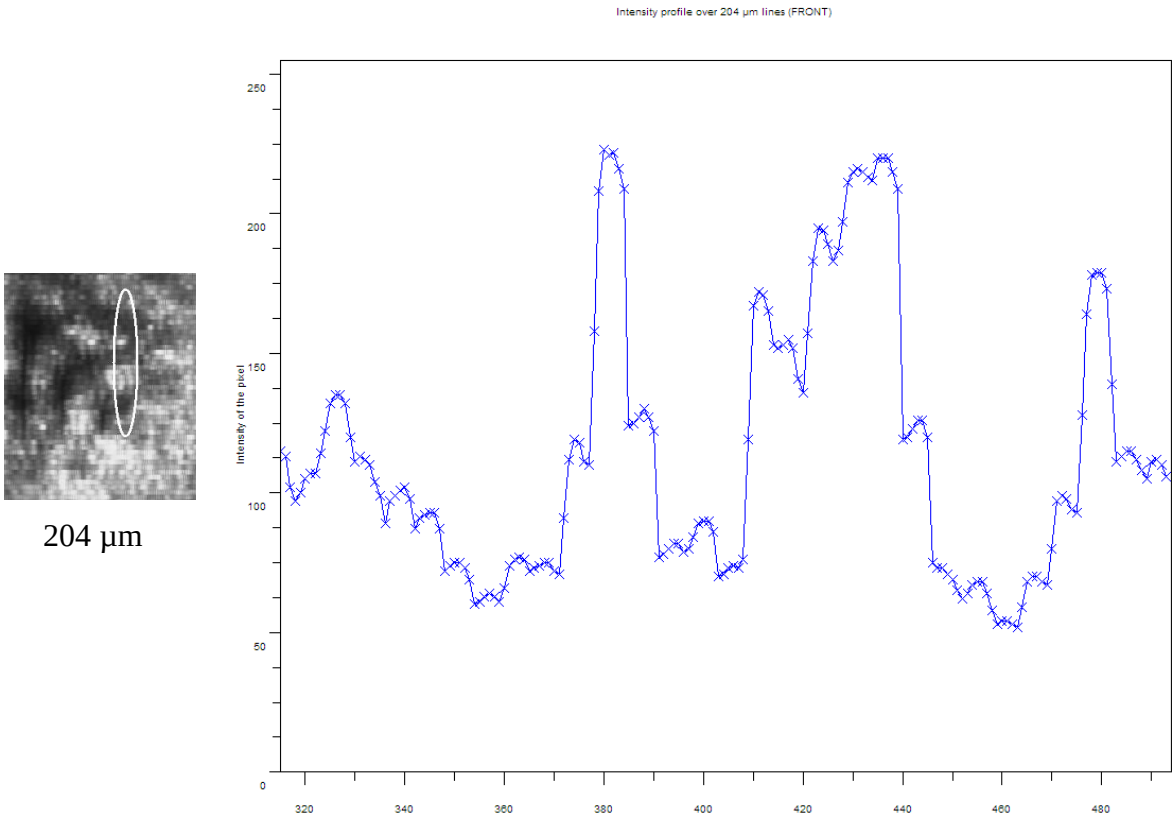

Figure 6-23 Intensity line profile for the 204 µm lines in front of ~1.2 mm chicken breast tissue and $\lambda = 670$ nm.

The above intensity profile plot can be used as an indicator of image contrast ratio. The 204 µm wide lines provide a contrast ratio of approx. 0.40 to 0.53. The exact contrast ratio is difficult to determine because of the unevenness of the image.

For scans of the ~2.7 mm and ~3.8 mm thick chicken samples, shown as follows in Figure 6-24, the 204 µm test structure is clearly labeled.

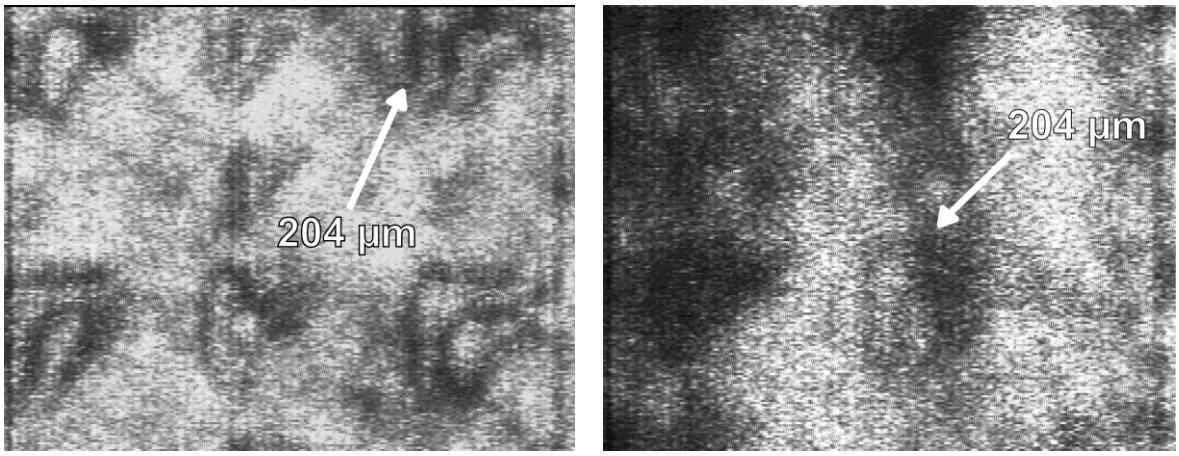

(a) ~2.7 mm thick (b) ~3.8 mm thick

Figure 6-24 Small test structures (204 µm – 51 µm) at λ = 670 nm in front of ~2.7 mm and ~3.8 mm chicken breast tissue.

The ~2.7 mm scan (Figure 6-24a) shows the 204 µm, 153 µm, and 102 µm test structures all visible in the image, with the 51 µm test structure not clearly visible. However, only the 204 µm lines and spaces in the image are partially resolvable, while the individual 153 µm lines are not clearly distinguishable. The ~3.8 mm scan (Figure 6-24b) shows the 204 µm test structure visible in the image, but its individual lines and spaces are largely obscured. The three smaller test structures are not clearly visible and appear obscured by non-uniformities in the tissue.

The following figure presents a line profile plot across the 204 µm lines and spaces for the ~2.7 mm thick sample.

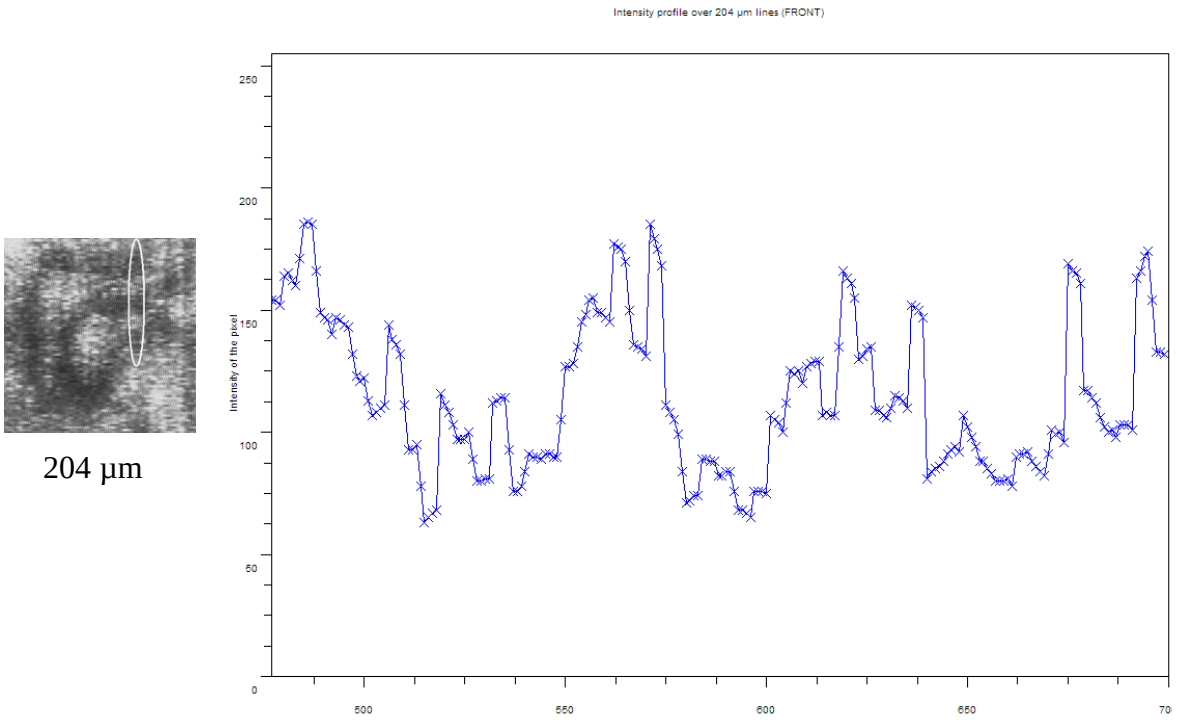

Figure 6-25 Intensity line profile for the 204 µm lines in front of ~2.7 mm chicken breast tissue and λ = 670 nm.

As compared to the line profile for the ~1.2 mm thickness sample, the ~2.7 mm sample exhibits an approx. 0.46 contrast ratio for the 204 µm test structure lines, which is lower on average than the 0.40 to 0.53 contrast ratio for the thinner sample. Furthermore, the ~3.8 mm thick sample appears to exhibit similar or lower contrast compared to the ~2.7 mm sample. Thus, these results appear to indicate that contrast is degrading as thicker biological tissue samples are being imaged. However, there exists a high number of artefacts in the images, which makes it difficult to draw definitive conclusions on imaging performance and contrast from these results.

Similarly as for the milk scattering solution scans, digital signal processing techniques have also been employed by Vasefi for these biological tissue scans to enhance contrast and bring out information that is not clearly distinguishable to the naked eye [25]. These results with DSP enhancement demonstrate that image contrast and resolution can be improved using DSP techniques, which may allow for more highly scattering tissue samples (e.g. thicker tissue) to be imaged in the future.

6.2.3 Surface scattering effects with the chicken tissue samples

In addition to tissue non-uniformities, unexpectedly high scattering levels were measured for the chicken tissue samples used in this ADI research. Scattering Ratios and other parameters calculated for the ~1.2 mm, ~2.7 mm, and ~3.8 mm chicken breast tissue samples are presented as follows.

Table 6-1 Calculated scattering values for the chicken tissue samples.

Sample thickness	Measured SR	Preliminary μ_s'	Exponential-fit μ_s'
~1.2 mm	1.90×10^4:1	16.4 cm^{-1}	6.8 cm^{-1} to 8.9 cm^{-1}
~2.7 mm	5.27×10^4:1	8.1 cm^{-1}	
~3.8 mm	1.40×10^5:1	6.2 cm^{-1}	

From an analysis of the scattering values shown in Table 6-1, it can be seen that when the thickness of a scattering sample is doubled or more, the measured SR does not increase by the square from the Beer-Lambert Law (Equation 1-1) suggests. For example, when sample thickness is increased from approx. 1.2 mm to 2.7 mm (a factor of 2.25×), the SR is increased by a multiplicative factor of 2.77× (SR = 5.27×10^4:1), as opposed to being raised to the 2.25^{th} power (SR = 4.24×10^9:1). This relationship between scattering medium thickness and measured SR is illustrated by Figure 6-26, which plots Scattering Ratio (in log scale) versus sample thickness.

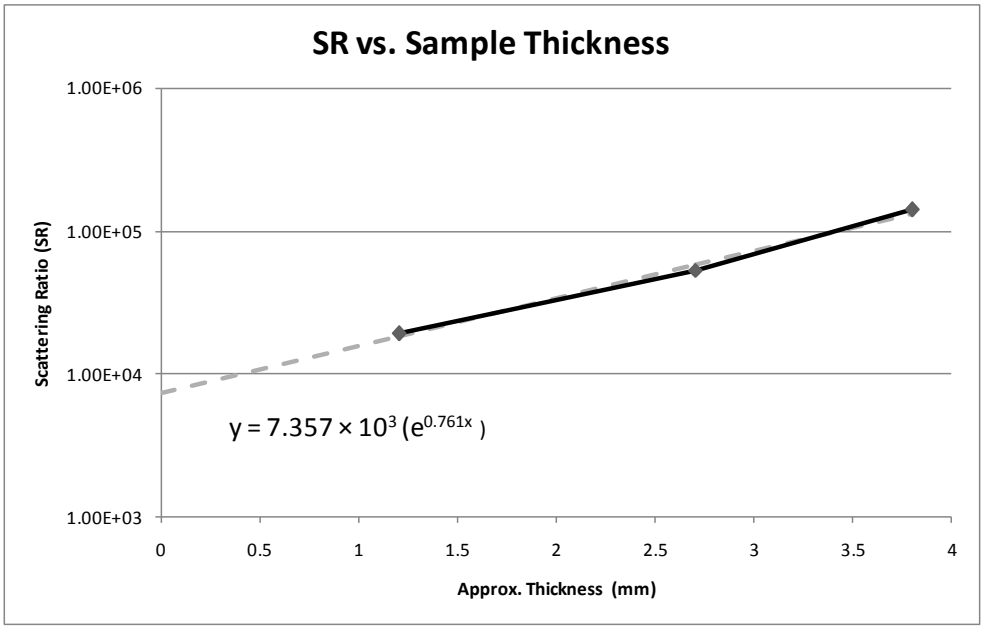

Figure 6-26 Scattering Ratio versus sample thickness for chicken breast tissue at $\lambda = 670$ nm.

The line plotted in Figure 6-26 does not appear to originate from the "origin" of the graph but appears to have a large vertical offset. Indeed, if an exponential line is fitted to the three data points, it intercepts the vertical axis at SR = 7.357×10^3:1, which corresponds to the scattering level for a zero thickness tissue sample. The actual formula for this fitted line is $y = 7.357 \times 10^3 (e^{0.761x})$, where x is the tissue thickness. With a sample of zero thickness (i.e. no sample at all), one would expect zero scattering, and thus there appears to be a scattering effect which can be modeled as a multiplicative factor to Scattering Ratio and is constant regardless of sample thickness. Thus, the Beer-Lambert Law can be modified to reflect this new multiplicative factor as follows,

$$I_{out} = I_{in} \cdot \frac{1}{S_x} \cdot e^{-(\mu_a + \mu_s)d}, \qquad \textbf{Equation 6-4}$$

where S_x can be termed the surface scattering constant, and is the value of the y-intercept found for Figure 6-26. Thus, from our results S_x is approximately 7.357×10^3. Assuming that chicken tissue acts generally as a homogenous scattering medium, then this surface scattering factor can be attributed to effects from the interfaces between surfaces for the tissue sample, and not a product of the interior components of the tissue. No surface scattering factor was observed for the milk-based scattering solution experiments, which

had an air-glass interface and a glass-solution interace. The tissue samples have the same air-glass interface, but also have a glass-gap-tissue interface, and thus it is probable that the surface scattering effect is a product of the latter. The effects of possible surface scattering at this interface are illustrated as follows in Figure 6-27 (the effect of glass is ignored for simplicity).

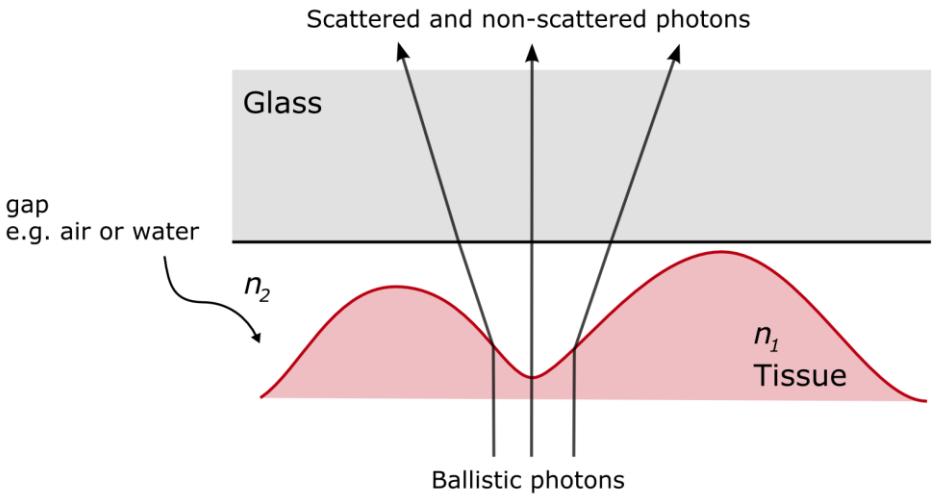

Figure 6-27 Illustration of the surface topology index mismatch effect at glass-gap-tissue interface.

The surface scattering effect can attributed to an uneven topology of the tissue coupled with an index of refraction mismatch between the tissue and another medium. Because the tissue sample is composed of a heterogeneous collection of biological cells that has been sectioned by hand with a scalpel, its surface topology will not form a perfectly flat interface when compressed against a glass slide. Rather, an uneven topology will form in contact with the glass slide with numerous gaps in between filled either by vacuum or air ($n_2 \approx 1$) or fluid (e.g. water: $n_2 = 1.33$), which can have different indices of refraction relative to the tissue (n_1) or glass. As a result, ballistic or quasi-ballistic light that passes through this interface will be refracted off their perpendicular trajectories according to Snell's Law, leading to an increase in scattered light in a distribution of angles. Such a surface topology index mismatch can scatter ballistic and quasi-ballistic light as illustrated in the previous figure. A full computational model relating the amount of surface scattering to the index of refraction change and the height and depth frequency of the surface structures has been developed by Nick Pfeiffer to be presented in his forthcoming PhD thesis.

Another indication that scattering is occurring apart from the internal tissue scattering is the fact that the reduced scattering coefficient μ_s' has different values when calculated at different tissue thicknesses (see Table 6-1). However, the μ_s' parameter describes the scattering properties of a tissue and should be constant for all tissue samples of the same type. Because surface scattering is dependent on the glass-gap-tissue interface, then as the sample thickness is increased, surface scattering will stay constant while the internal scattering of the tissue will increase exponentially. However, at these thicknesses, the surface scattering level is dominant. Therefore, as the sample thickness is increased the relative contribution of the surface scattering offset S_x slowly becomes minimal, causing the measured μ_s' value to decrease (16.4 cm^{-1} at ~1.7 mm thick tissue to 6.2 cm^{-1} at ~3.8 mm thick tissue) towards that of the internal tissue alone.

One way to find the μ_s' value of the internal tissue only (apart from the S_x effect) is to calculate the slope between points in the SR vs. Sample Thickness plot (Figure 6-26) to find the μ_s' value. The procedure for this is as follows. First, we can rewrite the Beer-Lambert Law (Equation 1-1), ignoring the effect of absorption, to introduce the surface scattering factor S_x as follows,

$$I_{out} = I_{in} \cdot \frac{1}{S_x} \cdot e^{-(\mu_s')d} . \qquad \textbf{Equation 6-5}$$

This equation can be manipulated as follows,

$$S_x \cdot e^{(\mu_s')d} = \left(\frac{I_{in}}{I_{out}} \right) = SR . \qquad \textbf{Equation 6-6}$$

Thus, by taking the natural logarithm of a measured Scattering Ratio *SR* for a given scattering medium thickness *d*, the exponential function is removed and the equation becomes an expression in terms of μ_s'. Thus, by taking the natural logarithm of two SR values for two different thicknesses, and subtracting one from the other, one obtains

$$\ln(SR_2) - \ln(SR_1) = \ln(S_x) + \mu_s' d_2 - \ln(S_x) - \mu_s' d_1 = (d_2 - d_1)\mu_s' , \qquad \textbf{Equation 6-7}$$

where d_1 and d_2 are the sample thicknesses for two different samples. This formula can be solved to find the μ_s' value for tissue as given by,

$$\mu_s' = \frac{\ln(SR_2) - \ln(SR_1)}{(d_2 - d_1)}. \qquad \textbf{Equation 6-8}$$

Using the data points from Figure 6-26, one can calculate a range of μ_s' = 6.8 cm^{-1} to 8.9 cm^{-1}, which is much lower than the 6.2 cm^{-1} to 16.4 cm^{-1} range of values that do not take the S_x factor into account. However, current literature indicates a reduced scattering coefficient μs' value in the range of 2.2 cm^{-1} to 2.4 cm^{-1} for chicken breast tissue at 670 nm [29]. This difference in calculated μ_s' may be due to differences in the chicken tissue used as samples. Further research should be undertaken to understand this discrepancy between our chicken tissue sample reduced scattering coefficient and that reported in the literature.

Index matching fluids have been employed in an effort to minimize the surface scattering effect. An index matching fluid is a fluid that shares the same index of refraction as the tissue sample (i.e. $n_1 \approx n_2$). The tissue sample either has the index matching fluid applied to the tissue-glass interface or the tissue can be suspended in the index matching fluid so as to fill the gaps created by the uneven tissue topology. If these gaps are filled with a medium sharing the same index of refraction as the tissue, then the tissue surface effectively becomes planarized and will no longer exhibit surface scattering due to index mismatch (i.e. light rays will not change in angle). It is important to use a fluid that matches the tissue index of refraction as closely as possible, while maintaining a stable relationship with the tissue (e.g. does not dry out or break down the tissue). One difficulty is that simply adding water for index matching results in other problems. Water does not adequately wet the surface, creating bubbles and other index mismatch problems. As a result, preliminary experiments with water and other potential index matching fluids have not significantly reduced the surface scattering effect. Exploration into which fluids perform best with chicken breast tissue remains to be conducted.

6.3 Chapter summary

Results with the new 670 nm laser diode AFA system demonstrate comparable performance with previous ADI research conducted using the Argon ion laser AFA system for milk-based scattering solutions. Lower scattering coefficients were observed at the 670 nm wavelength compared to the Argon ion wavelengths (488 – 514 nm) for calibrated milk solutions. Milk solutions at SR = 1.0×10^7:1 were successfully imaged with resolution of 153 µm or better. As the SR is increased, image resolution was found to be largely unaffected while image contrast degrades significantly, which agrees with previous Argon ADI results. Also in agreement are results showing that 670 nm laser diode scans show better image contrast when test objects are brought closer to the AFA in a highly scattering medium. Interference pattern-like effects were observed in the 670 nm scans for the 102 µm test structure when placed at the front (5 cm) position of the sample. Individual 204 µm- and 153 µm-sized lines and spaces were partially resolvable for chicken breast tissue samples ~1.2 mm and ~2.7 mm thick. At a thickness of ~3.8 mm, the 204 µm test structure was partially resolvable, with image contrast decreasing slightly as tissue thickness is increased.

A surface scattering effect independent of sample thickness was observed for the chicken tissue samples. The effect of index mismatch between the uneven topology of the tissue and the gap at the glass-gap-tissue sample interface, leading to changes in angle to non-scattered light, were discussed. Estimated reduced scattering coefficients (μ_s') for the tissue alone were calculated. The use of index matching fluids to minimize the effect of surface scattering was also discussed. Further research can be undertaken to characterize the surface scattering effect by measuring the angular distribution of light as it exits the scattering sample. These results would help answer questions regarding how ballistic and quasi-ballistic light are being affected by surface scattering.

The following chapter discusses enhancements to the Angular Filter Array imaging process, including modifications to the AFA tunnel surface to reduce reflected light and smaller tunnel geometries and scanning step sizes to improve spatial resolution.

Chapter 7

Angular Filter Array Imaging Enhancements

Imaging with the Angular Filter Array encounters two issues that limit its performance. Firstly, a small proportion of the scattered light will always be transmitted through the AFA tunnels due to reflection, especially at very shallow angles. This scattered light degrades the signal-to-noise ratio in the image and prevents an intelligible image from being resolved under high SR conditions. This chapter introduces two different methods for addressing this problem: coating the tunnel surface with a light absorbing material; and roughening the topology of the tunnel surface to deflect scattered light that strikes the tunnel walls by large angles.

The second issue that is investigated in this chapter is the resolution limit due to the AFA tunnel geometry and scanning procedure. The effect of reducing the cross-sectional dimensions of the tunnels is explored. In addition, the effect of decreasing the vertical step size for the sample during imaging is examined.

7.1 Surface-Roughened Angular Filter Arrays

As the Scattering Ratio of a medium is increased, then by definition the proportion of scattered light to non-scattered light is directly increased. Thus, at high SR's, the ratio of noise (scattered) photons to signal (non-scattered) photons in the image is very high as light exits the medium and arrives at the Angular Filter Array. Because the noise photons are those which arrive at the AFA with large deviation angles, they are attenuated when they collide with a tunnel sidewall. However, AFA tunnels are composed of silicon and will reflect up to 40% of light upon a perpendicular reflection, with reflection close to unity at very shallow angles [24]. As calculated in *Section 2.2.3* using the Fresnel reflection formulae (Equation 2-1), light arriving at the acceptance angle of 0.29° will be reflected by up to 95% - 97%, depending on polarization. Reflected light within the tunnels will also emerge at a wide range of angles and can blur the image at the sensor. Figure 7-1 demonstrates the effect of scattered light reaching the image sensor under

conditions ranging from no scattering to high scattering levels under illumination from the Argon laser and Galilean spherical beam expander.

(a) SR = 0:1 (water) (b) SR = 1.0×10^7:1 (c) SR = 6.0×10^9:1

Figure 7-1 Angular Filter Array tunnels under illumination at λ = 488-514 nm and varying SR values.

As shown in Figure 7-1a, with no scattering the illuminated tunnels are well defined and isolated from one another in the image. Some vertical spreading is noticeable, as the tunnels should appear as horizontal semi-circles instead of vertical ellipses. This may be attributed to diffraction along the top and bottom edges of the tunnel, which is discussed in the next section (*Section 6.2*). As the SR is increased to 1.0×10^7:1 (Figure 7-1b), which is just beyond the scattering limit for imaging with the Argon laser with spherical beam expander, however, we see that the spreading of the tunnels increases, and the illuminated region from each tunnel appears to spill into the inter-tunnel gap and into adjacent tunnels due to the reflection of light at large angles. This trend continues as SR is increased to 6.0×10^9:1 (Figure 7-1c), which is far beyond the scattering limit for successful imaging with the setup. If the tunnel walls were perfectly absorbing, this behaviour would not occur. The transmission of reflected scattered light presents two problems: firstly, this reflected proportion of scattered light will add to the scattered light accepted by the AFA, increasing the background noise level. This results in a degradation of signal-to-noise ratio, and consequently, a loss in contrast. Secondly, as light reflects within the tunnels and spreads into other tunnel regions in the image, spatial resolution is lost.

Two avenues for increasing the attenuation of reflected light within the AFA tunnels are explored: coating of the tunnels with an absorbing carbon layer; and roughening the tunnel surface topology using an NH_4OH-based solution.

7.1.1 Tunnel coating via carbon evaporation deposition

Carbon was chosen as a coating material because it is highly absorbent to light. A simple evidence of this is its black color, which indicates that it absorbs light across the visible spectrum. A carbon arc evaporator system from the Physics department of Simon Fraser University was employed to deposit a carbon layer on the AFA tunnels. The evaporator operates by passing a high current (approx. 100 Amperes) through two carbon tip electrodes, thereby evaporating a portion of the electrodes and depositing a thin film of carbon on the AFA pieces placed in the evaporator chamber. The deposition process was completed four times, for an estimated film thickness of 30-40 nm, though this value is solely based on listed estimates for the machine. The work presented in this section with the carbon deposited AFA devices was carried out in conjunction with PhD candidate and fellow researcher Fartash Vasefi.

The deposition process is a very messy process, with high levels of particulates and debris being generated (as shown in Figure 7-2). This leads to occlusion of the AFA tunnels, and aggressive cleaning techniques such as an RCA-1 clean (often used in microfabrication) leads to lift-off of the carbon film. Thus, an ultrasonic acetone bath was employed to clean the AFA, though it is much less effective.

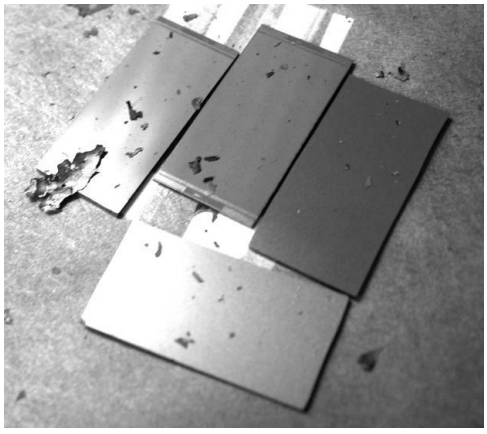

Figure 7-2 Photograph of AFA pieces after carbon evaporation deposition.

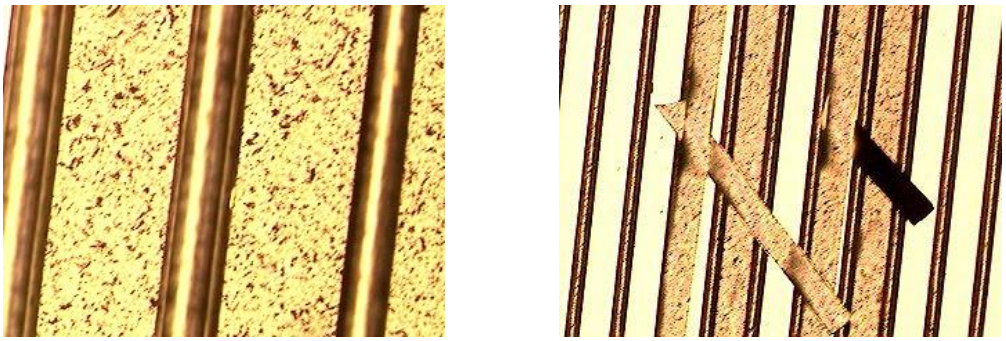

(a) Magnified view of coated AFA tunnels (b) Magnified view showing carbon film lift-off

Figure 7-3 Microscope images of the AFA after carbon evaporation deposition.

Preliminary experiments demonstrate that the carbon film deposition is effective in increasing the attenuation of light that enters an AFA tunnel outside its maximum acceptance angle [24]. Images of illuminated AFA tunnels comprised of untreated silicon (Si) or carbon deposited (C) tunnels are shown in Figure 7-4 across a range of alignment angles. In these experiments, the AFA device is intentionally misaligned by an angle greater than the acceptance angle in order to prevent ballistic light from passing straight through the tunnels. Instead, the only light detected by the image sensor will be light that is reflected off the tunnel walls. Thus, these experiments allow us to measure how effective the AFA devices are in attenuating scattered or reflected light. *Tilt down* images represent an intentional vertical misalignment of the AFA to the incoming illumination beam (Argon laser with spherical beam expander) by lowering the front end of the AFA. *Yaw left* represents a lateral misalignment by shifting the front end of the AFA to the left.

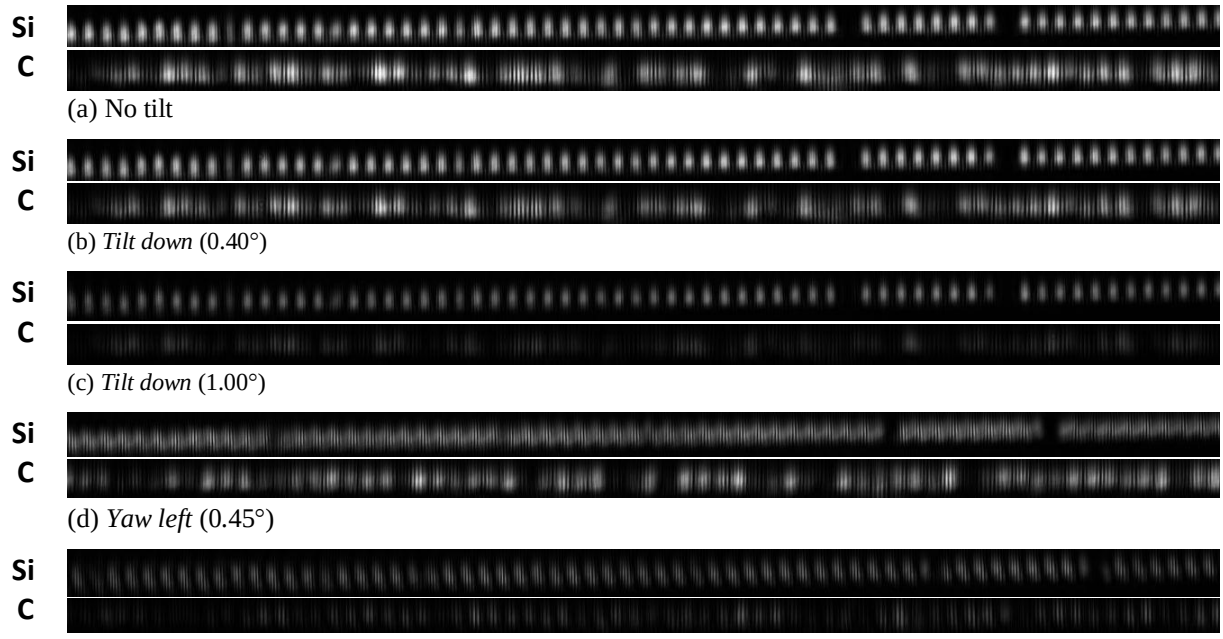

Figure 7-4 Tilt images for untreated and carbon coated AFA tunnels under illumination (Argon laser).

As shown in Figure 7-4, as the AFA is tilted downwards towards 1.00°, the carbon coated AFA tunnels attenuate light such that illumination is brought almost to zero, while the untreated silicon tunnels still appear illuminated at the same angles. Similarly, the same behaviour is observed when the AFA is yawed to the left by 0.91°. These results indicate that the carbon coating improves attenuation of reflected light for incident angles greater than the acceptance angle (0.29°). This attenuation is a result of the absorbent properties of carbon and also the uneven deposition and topology of the carbon coating, which helps attenuate shallow angle reflection.

However, a significant challenge arises from occlusion in the AFA tunnels caused by debris from the deposition process which causes illuminated tunnels to appear dark. This translates into dark columns in AFA ADI scans, as shown in Figure 7-5, where imaging information has been lost. At a high SR of 2×10^6:1, the inter-tunnel region appears darker than before, which indicates that scattered light reflected within the tunnels is being attenuated more effectively.

(a) carbon deposited, SR = 0:1 (DI water)

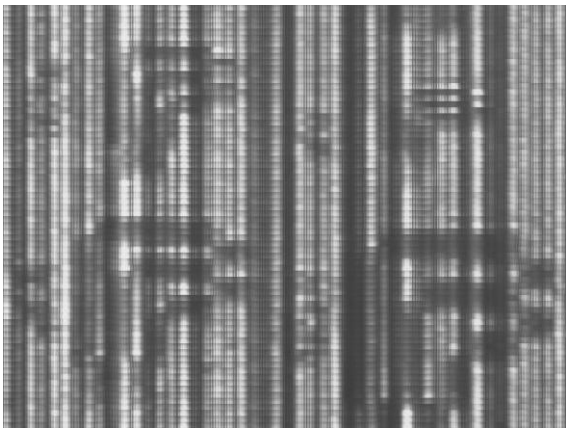

(b) carbon deposited, SR = 2×10^6:1

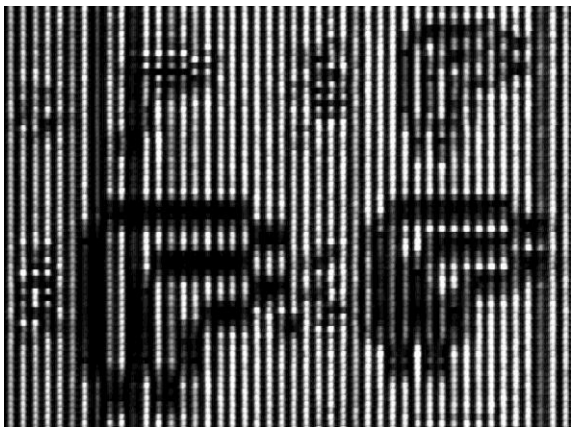

(c) normal silicon, SR = 0:1 (DI water)

Figure 7-5 Small test structures (204 μm – 51 μm) in 2.7 cm (Middle) at λ = 488-514 nm with carbon deposited AFA tunnels.

The carbon deposition results presented in this section demonstrate that they are effective in attenuating reflected light within the tunnels. However, debris from the deposition process interfere with successful imaging using the carbon coated tunnels, and the scattering limit for a carbon deposited AFA device is still on the order of SR = 10^6:1.

To remove the surface debris problem, a more conformal method of carbon deposition was been conducted by fellow researcher Fartash Vasefi. This experimentation showed that sputter deposition of a smooth carbon film (approx. 200 nm thick) does not significantly increase attenuation of reflected light at shallow angles [31]. Because of the smoothness of the film, the Fresnel reflection formulae (see Equation 2-1) apply and

reflection at very smooth angles will be close to unity (e.g. >90%). In order to more fully determine the potential performance benefits of AFA tunnel carbon deposition, further experiments should be conducted.

7.1.2 Chemical roughening via an NH_4OH-based solution

Surface topology is a significant factor in attenuating reflected light within the AFA tunnels. Because the AFA is etched from polished silicon, the tunnel walls are naturally smooth and quite reflective to light, and light that enters at shallow angles will undergo only a small number of reflections before exiting the tunnel. However, if the tunnel wall topology can be significantly roughened, light that intersects the tunnel sides at shallow angles is no longer encounters a flat sidewall at a shallow angle, but instead will be reflected along a wide distribution of angles depending on the roughness of the tunnel. Thus, even shallow angle light becomes reflected into higher angles, which means it will undergo many reflections. Therefore, by significantly increasing the average number of reflections that a scattered photon must undergo before exiting the tunnel, the losses at each reflection rapidly attenuate the light and the overall level of scattered light that is transmitted through the AFA can be greatly reduced.

The method chosen for roughening the AFA tunnel topology consisted of chemical etching of the AFA device using a NH_4OH solution. The procedure requires a 5:1 ratio solution of de-ionized water (H_2O) to ammonium hydroxide (NH_4OH), heated to an approximate temperature of 80° C. The addition of hydrofluoric acid (HF) to the solution in a ratio of 5:1:0.1 (H_2O:NH_4OH:HF) was observed to aid in roughening uniformity across the AFA surface. The AFA devices are first hydrated in DI water before being immersed in the heated H_2O:NH_4OH solution for 10 minutes, followed by a DI water rinse. Results after NH_4OH roughening were inconsistent, and even roughening across the entire AFA surface was hard to achieve. Further experimentation is required to produce chemically roughened AFA devices with the desired optical characteristics. Results with roughened AFA tunnels under 670 nm laser diode illumination are shown in Figure 7-6.

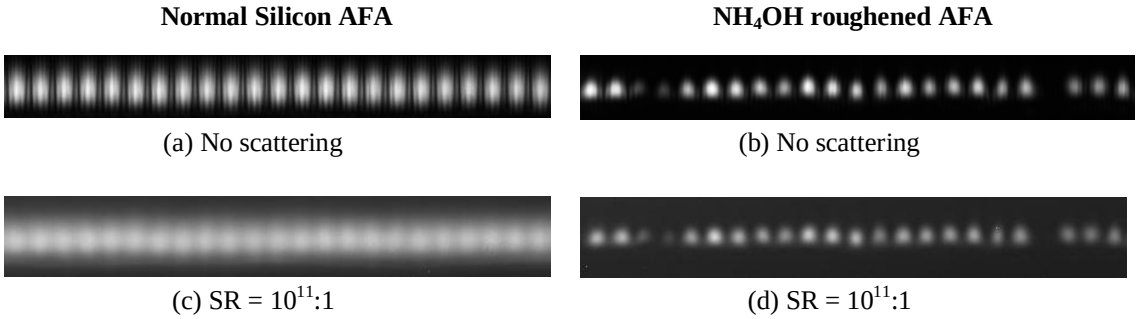

Figure 7-6 Normal and NH_4OH roughened AFA devices at $\lambda = 670$ nm without or with scattering.

As shown in Figure 7-6, roughening of the AFA tunnels significantly attenuates reflected scattered light within the tunnels. The inter-tunnel spacings appear black for the NH_4OH tunnels, while light appears diffuse and greyish amongst the normal silicon AFA tunnels under high scattering levels. This result shows that reflected light is being attenuated within the NH_4OH tunnels before it can exit and reach the image sensor. In addition, the NH_4OH roughened tunnels appear more tightly confined in shape under illumination, as opposed to appearing vertically elongated in the case of the untreated tunnels. This vertical elongation is a result either of reflected light bouncing in the tunnels or diffraction effects from the tunnel opening. In either case, Figure 7-6 demonstrates that the NH_4OH roughened tunnels are effectively attenuating reflected light along the vertical axis. However, it should be noted that a small proportion of the NH_4OH roughened tunnels appear occluded under illumination, thus resulting in dark vertical bands in the scans where image information is missing. Further experiments should be conducted to improve the evenness of the silicon roughening process so as to keep the channels clear and intact for imaging.

Figure 7-7, shown as follows, presents two scans of 204 µm to 51 µm test structures placed in front of a 5 cm SR = 10^6:1 medium imaged through a normal and an NH_4OH roughened AFA device.

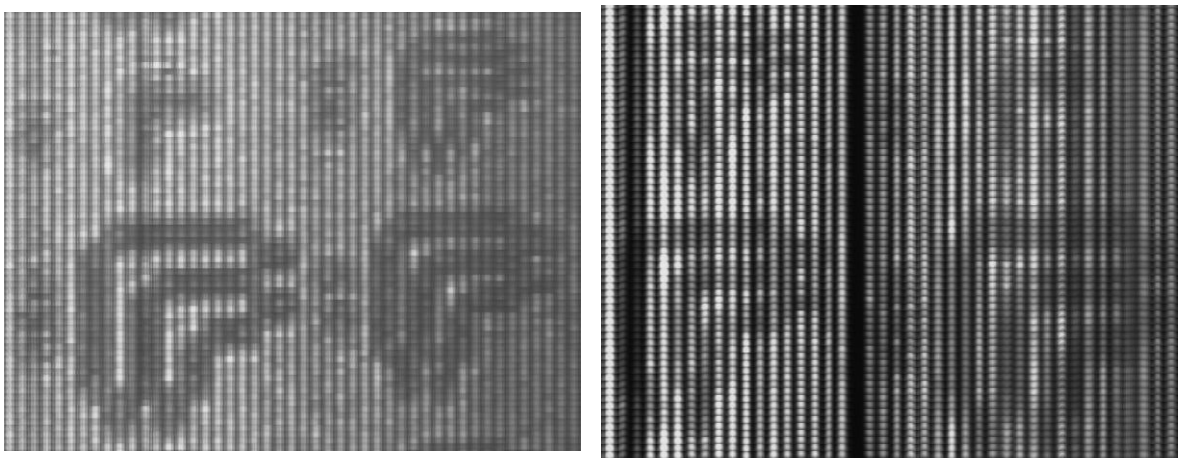

(a) normal silicon, $\lambda = 670$ nm, SR = 10^6:1 (b) NH_4OH roughened, $\lambda = 670$ nm, SR = 10^6:1

Figure 7-7 Small test structures (204 µm – 51 µm) in 5 cm (Front) with normal and NH_4OH roughened tunnels at high SR.

Figure 7-7 shows that the NH_4OH roughened tunnels significantly reduce the illumination between tunnels, leading to the inter-tunnel gaps appearing as dark, vertical columns in the image (Figure 7-7b) instead of the lighter, grayish bands between the normal AFA tunnels (Figure 7-7a) [25]. However, the overall image contrast does not appear noticeably improved. The following figure presents an intensity line profile plot across the 204 µm test structure lines for both scans.

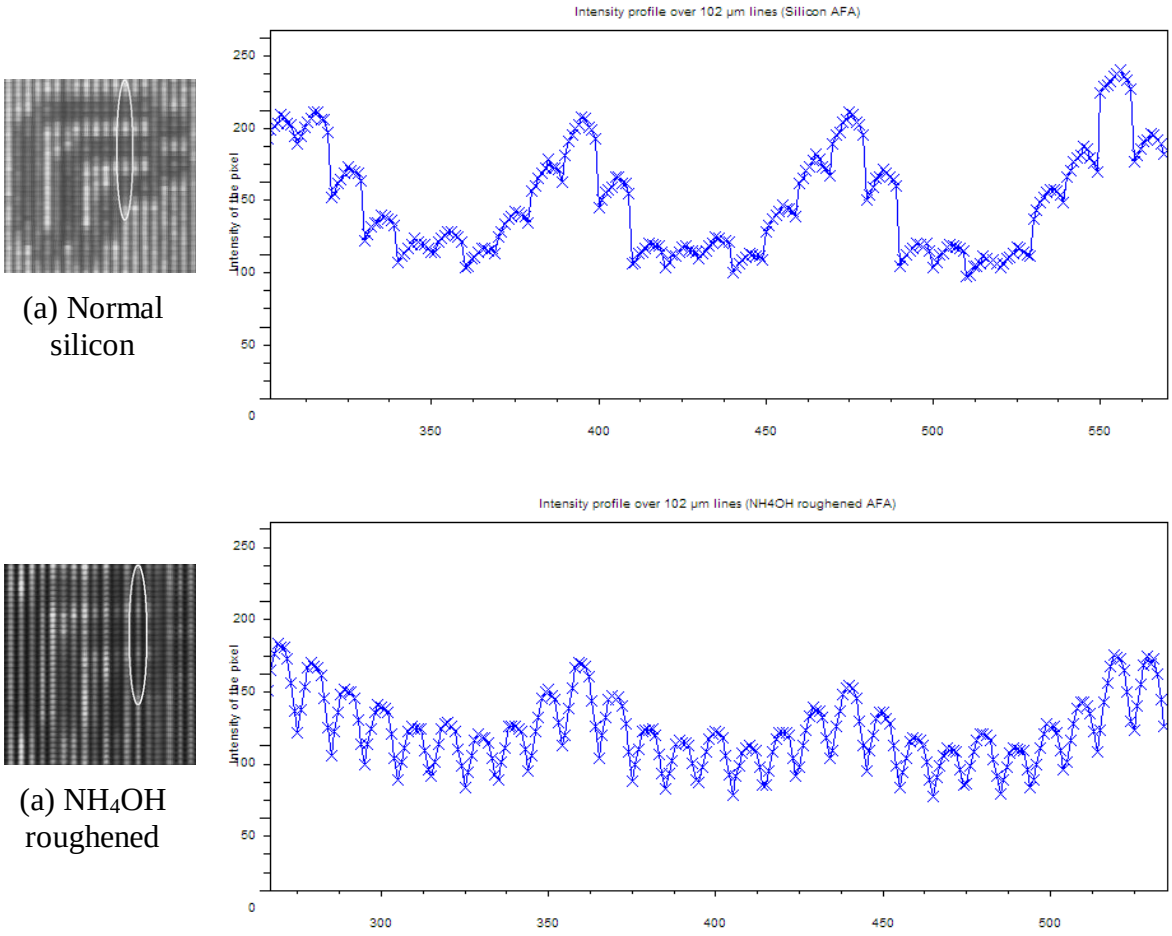

Figure 7-8 Intensity line profile for 204 µm lines in 5 cm at SR = 10^6:1 for the normal Silicon and NH_4OH roughened AFA devices.

From Figure 7-8, an estimated contrast ratio of approx. 0.26 can be calculated across the 204 µm lines in the Silicon AFA scan. For the NH_4OH scan, the estimated contrast ratio is approx. 0.32, which indicates that contrast for both scans is similar, with the NH_4OH showing higher contrast.

NH_4OH roughening appears to be similarly or more effective than carbon deposition for attenuating reflected light within the AFA tunnels, while suffering much less from occlusion of the tunnels. However, further experimentation into NH_4OH roughening of the AFA tunnels to determine its potential benefits for image contrast and resolution should be undertaken in future work, in addition to determining the scattering limit for its performance.

7.2 Smaller Angular Filter Dimensions and Vertical Step Sizes

Object resolution appears limited by two factors in AFA ADI scans: horizontally, by the width of the AFA tunnels; and vertically, by the height of the region that is imaged during each incremental step in imaging (i.e. the vertical step size). This section will explore the effects of reducing the tunnel cross-sectional dimensions, along with reducing the vertical step size used in AFA imaging, with discussion on the effects of these changes on image contrast and resolution. These scans were taken using the Argon ion laser with spherical beam expander.

7.2.1 Smaller AFA tunnel dimensions

The standard dimensions of an AFA tunnel is 51 µm wide × approx. 17 µm high, with a length of 1 cm. Smaller AFA tunnels were fabricated at 25.5 µm wide × approx. 10 µm high, with the same length of 1 cm, using the same photolithography equipment as discussed previously in *Section 2.2.2*. Slightly different etch times were used (approx. 4 minutes), and the mask section previously designed for 25.5 µm channels was used (see Figure 2-7 for the mask pattern as transferred onto a silicon wafer). This mask pattern starts with narrower 5 µm wide openings in the oxide for these tunnels. The desired amount of etching was achieved by etching the silicon for a set amount of time, checking the dimensions of the tunnels under a microscope, and then resuming etching if more was required.

A scanning electron micrograph of a 25.5 µm AFA device without covering piece (Figure 7-9), along with a profilometer measurement of the channel topology (Figure 7-10) are presented as follows. Note that as the profilometer stylus is ~10 µm in size itself, it only measures the top width and depth of the tunnels accurately, while the shape of the slopes will be distorted.

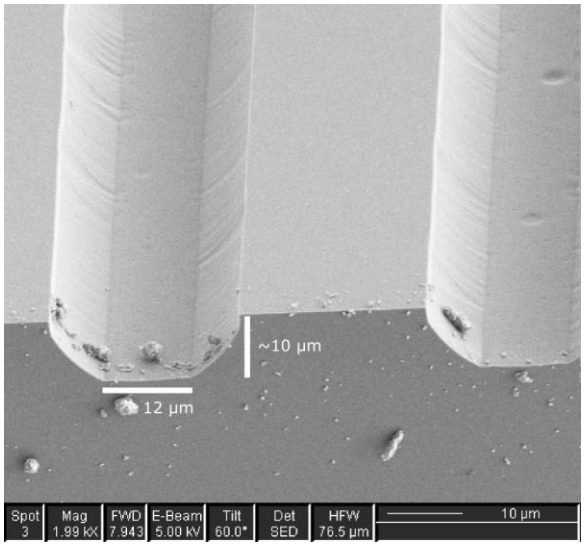

Figure 7-9 Scanning electron micrograph of the 25.5 µm AFA channel.

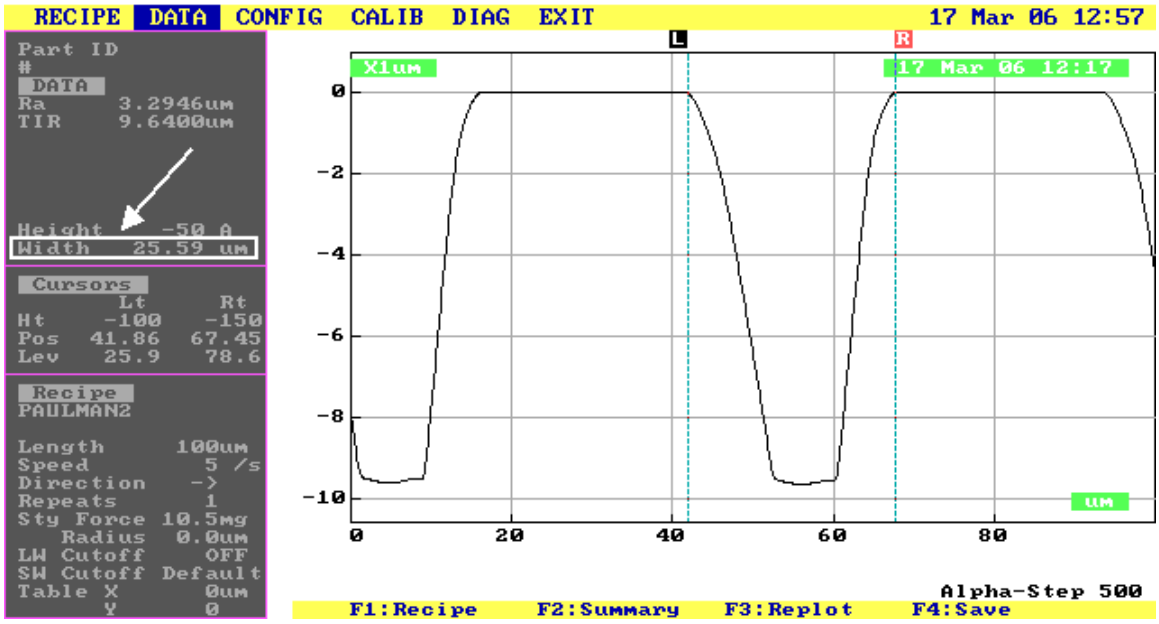

Figure 7-10 Profilometer screen capture of a 25.5 µm AFA channel (horizontal axis is compressed).

Two challenges were presented by the smaller 25.5 µm AFA tunnels. Firstly, the 25.5 µm AFA tunnels appeared highly vertically elongated under illumination as compared to the normal dimension AFA tunnels (see Figure 7-11). Secondly, power levels much greater than normal were required to illuminate the 25.5 µm AFA tunnels, as compared with the 51 µm AFA tunnels, even when under non-scattering conditions. This difference in

required power is much greater than expected, and thus, further investigation should be conducted as to its cause.

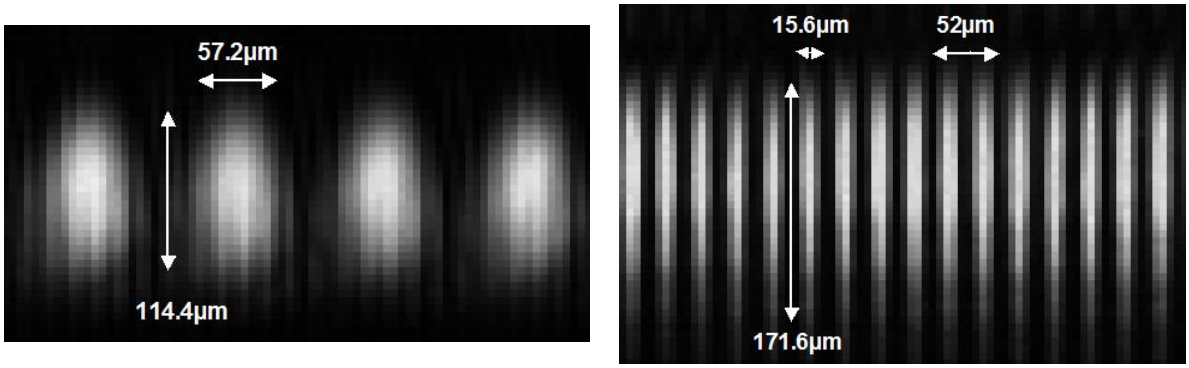

(a) Illuminated 51µm tunnels, λ = 488-514 nm **(b)** Illuminated 25.5µm tunnels, λ = 488-514 nm

Figure 7-11 Illuminated 51 µm- and 25.5 µm- wide AFA tunnels at λ = 488-514 nm.

The 25.5 µm AFA tunnels appear narrowly confined in the horizontal axis in the image, but are greatly spread out in the vertical axis. In fact, the smaller AFA tunnels appear approx. 171.6 µm high when their physical height is only approx. 10 µm. The larger 51 µm-wide AFA tunnels appear approx. 114.4 µm in height (physical height is approx. 17 µm), which is actually smaller compared to the 25.5 µm-wide tunnels.

Diffraction effects appear to be noticeable for the 25.5 µm-wide tunnels (Figure 7-11b), which is an indication that diffraction is becoming more significant at small geometries such as these. For example, diffraction is the probable cause of the vertical elongation of the illuminated tunnels. For tunnels with a height of 17 µm or 10 µm, which is close to only one order of magnitude greater than the illuminating wavelength (i.e. 488-514 nm), diffraction can become a significant factor in angular spread of non-scattered light. Using the formula for Fraunhofer interference (see Equation 6-2), Figure 7-12 and Figure 7-13 graph the relationship between angular spreading in the horizontal and vertical axes, respectively, for diffracted light. Results are shown for both the 51 µm- and 25.5 µm-wide AFA tunnels.

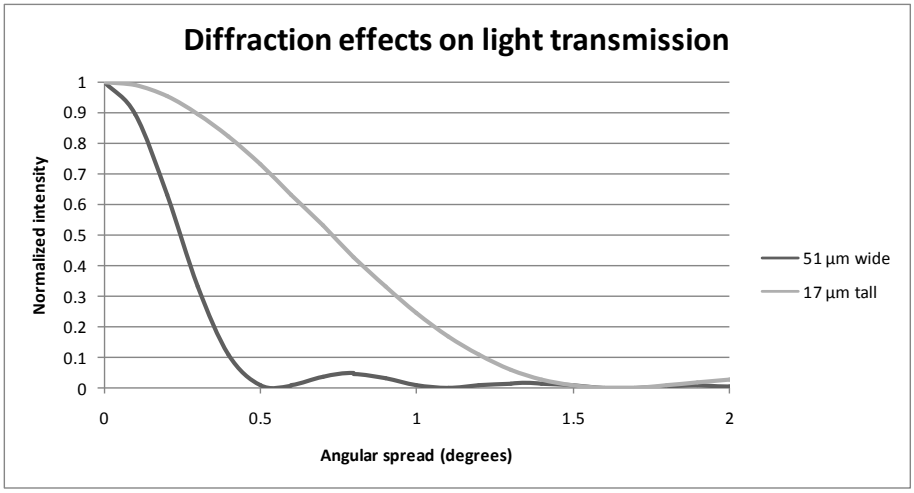

Figure 7-12 Angular spread due to diffraction from the AFA tunnels (horizontal axis).

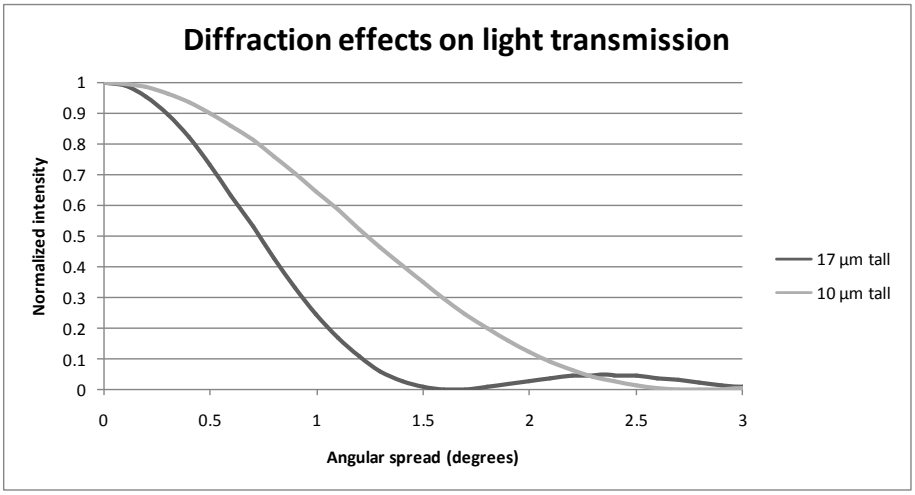

Figure 7-13 Angular spread due to diffraction from the AFA tunnels (vertical axis).

As shown in the above figures, diffraction effects are especially pronounced in the vertical axis (compared to the horizontal axis) because of the AFA tunnels' small heights. For an estimated distance of 2 mm between the end of the AFA tunnels and the image sensor, light will spread vertically by ±56 µm and ±98 µm for divergence angles of 1.6° and 2.8°, respectively. These results mean that diffracted light can spread vertically (from black to black) up to 112 µm for the 51 µm-wide AFA tunnels, and up to 196 µm for the 25.5 µm-wide tunnels. These vertical distances are similar to those observed in actual images (see Figure 7-11).

As mentioned previously, illumination levels much greater than expected are required for the 25.5 µm AFA versus the 51 µm AFA for a collimated illumination beam. Part of the cause for this may be due to the increased effect of the diffraction that occurs at both the openings and ends of the tunnels for the smaller AFA. Light that is diffracted at the tunnel opening beyond the 0.29° total acceptance angle will be attenuated by the tunnel walls before it can reach the image sensor. Also, light that is diffracted at the tunnel ends are spread across a large vertical area, which reduces power density at the image sensor. Further analysis and experimentation is required to understand the drastic reduction in transmissivity for the smaller AFA device. In addition, it should be noted that due to the reduced geometry and increase aspect ratio of the 25.5 µm-wide tunnels, alignment of the AFA device is more difficult compared to the 51 µm-wide AFA.

7.2.2 Smaller vertical step sizes

The AFA ADI capture procedure involves stepping the sample vertically upwards by a fixed distance (52 µm by default), capturing a line image through the Angular Filter Array, and then repeating the entire process until a 2-D image can be assembled from the entirety of line images. Therefore, resolution in the vertical axis can theoretically be improved by increasing the vertical spatial sampling rate (i.e. decreasing the step size). However, this potential improvement must be verified and characterized through experimentation.

7.2.3 Experimental results

Figure 7-14, shown as follows, presents scans at the default vertical step size of 52 µm for both the standard 51 µm-wide and 25.5 µm-wide AFA tunnels, with small test structures (204 µm – 51 µm) placed at the back face of the sample (closest to AFA and imager).

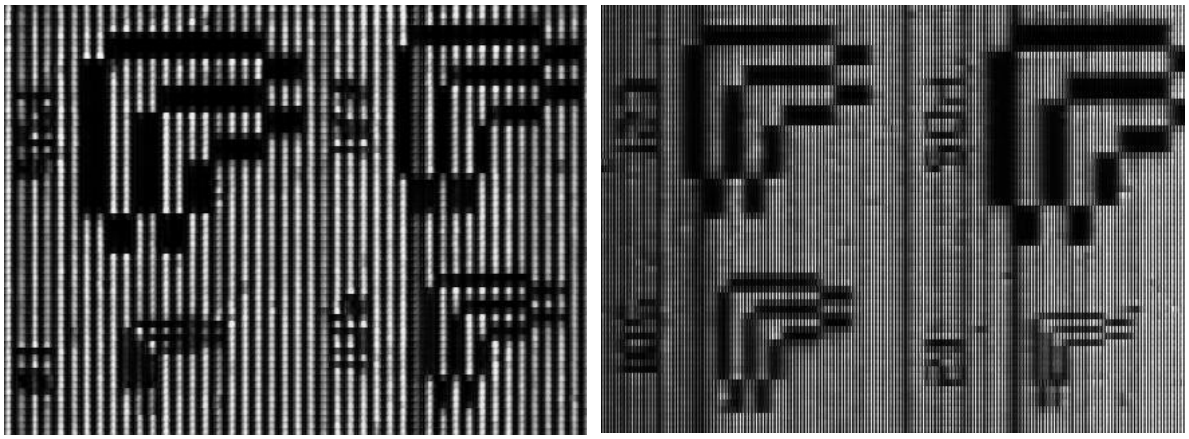

(a) *51 µm-wide, λ = 488-514 nm,*
Step size = 52 µm, SR = 0:1 (water)

(b) *25.5 µm-wide, λ = 488-514 nm,*
Step size = 52 µm, SR = 0:1 (water)

Figure 7-14 Small test structures (204 µm – 51 µm) at 0 cm (Back) for both AFA devices with 52 µm vertical step size.

As shown Figure 7-14, horizontal resolution is improved from 102 µm, previously, to 51 µm or better by reducing the width of the AFA tunnels from 51 µm to 25.5 µm. In the 25.5 µm AFA scan (Figure 7-14b), all the 51 µm-wide lines and gaps in the smallest test structure are individually resolvable, whereas they were previously indistinguishable along the horizontal axis in Figure 7-14a. Also, note that the numeric labels besides the test structures are more clearly visible in the narrower tunnel scan.

Vertical resolution appears improved with the 25.5 µm-wide AFA, as well. However, since the vertical step size is 52 µm, it should be noted that the smallest 51 µm features may disappear due to aliasing, as according to Nyquist's theorem, if the starting point for scanning was shifted by a certain amount.

Figure 7-15, shown as follows, presents scans with a smaller vertical step size of 25.5 µm for both the standard 51 µm-wide and 25.5 µm-wide AFA tunnels.

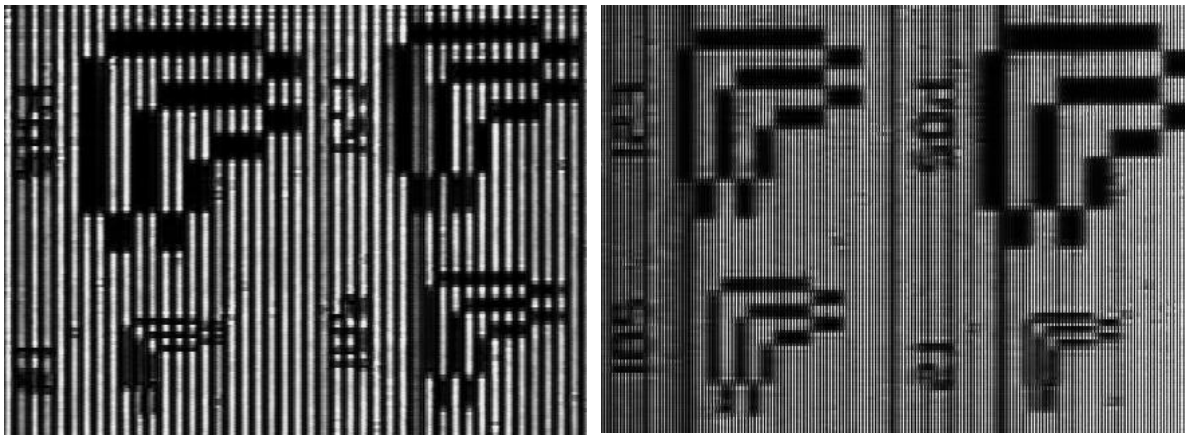

(a) *51 µm-wide, λ = 488-514 nm,*
Step size = 26 µm, SR = 0:1

(b) *25.5 µm-wide, λ = 488-514 nm,*
Step size = 26 µm, SR = 0:1

Figure 7-15 Small test structures (204 µm – 51 µm) at 0 cm (Back) for both AFA devices with 26 µm vertical step size.

Halving the vertical step size from 52 µm to 26 µm improves vertical image resolution for both sets of AFA tunnels. For the 51 µm-wide AFA scan (Figure 7-15a), the horizontal lines and spaces of the 51 µm test structure (bottom left of image) can now be independently resolved, whereas previously they were not individually distinguishable (see Figure 7-14a). As expected, horizontal resolution is not improved by reducing the vertical step size.

Scans taken with smaller step sizes (16 µm, 10 µm, and 5 µm), with test structures in the middle sample position (2.7 cm), and with SR = 8.0×10^5:1 all show similar results as those presented in this subsection, and thus are not included in this thesis due to repetition [32]. Results are consistent with the observed trend that 25.5 µm wide AFA tunnels improve spatial resolution, especially in the horizontal axis, while smaller vertical step sizes can improve vertical resolution, although with no significant improvement below a vertical step size of 26 µm. It should be noted that scans under highly scattering conditions, such as SR = 8.0×10^5:1, were only obtainable with the 51 µm AFA device because light transmission levels were too low for imaging a highly scattering medium with the 25.5 µm AFA.

7.3 Chapter summary

In this chapter, two solutions were examined for attenuating reflected light within AFA tunnels. Carbon deposition increased attenuation of scattered light beyond the AFA acceptance angle, but caused occlusion of the tunnels due to debris from deposition. Chemical roughening of the AFA tunnel topology using NH_4OH was successful in increasing attenuation of scattered light outside the acceptance angle, but with much less occlusion of the tunnels. While inter-tunnel illumination was reduced using both these methods, improvements in image contrast and maximum scattering limit were not observed.

In order to improve horizontal and vertical spatial resolution, smaller AFA tunnel dimensions and vertical step sizes were tested. By halving the width of the AFA tunnels from 51 µm to 25.5 µm, horizontal resolution was improved so that 51 µm features became resolvable. However, due to the smaller height and dimensions of the tunnels, increased diffraction effects were observed. In addition, illumination levels dropped many times lower than expected for the smaller 25.5 µm-wide AFA tunnels as compared to the 51 µm tunnels. This may partly be a result of increased diffraction at the entrance and ends of the AFA tunnels. However, further research should be conducted to determine the cause for this drastic drop in illumination.

Reducing the vertical step size from 52 µm to 26 µm produced the desired effect of improving vertical spatial resolution from 102 µm, previously, to 51 µm or better. Decreasing the vertical step size below 26 µm did not produce any significant effects for the experiments we conducted.

The following chapter presents experimental results for Spatial Filter ADI and compares theory with observed images.

Chapter 8

Angular Domain Spatial Filtering

The goal of this chapter is to verify the Spatial Filter theory introduced previously in *Section 2.3* with empirical results. Results for SF ADI are presented and analyzed, with a discussion on image contrast and resolution performance as Scattering Ratio, aperture diameter, image distance (i.e. magnification), and converging lens focal length.

Without detailed knowledge of the angular distribution of quasi-ballistic and scattered light exiting a scattering medium, it is not possible to quantitatively predict the image contrast and resolution in experimental results [22]. However, the trade-off between image contrast and resolution demonstrated in the SF ADI results is consistent with Equation 2-4 and Equation 2-10, introduced previously (and reposted as follows):

$$\theta_a = \frac{2r_f}{z_f} = \frac{d_a}{z_f} \text{ and } \Delta r_{o,a} = \frac{\lambda z_f}{d_a}.$$

Acceptance angle controls the level of angular discrimination of scattered light photons. Therefore, smaller acceptance angles result in a higher non-scattered (signal) to scattered (noise) photon ratio, which translates into higher image contrast. When d_a is increased (or z_f is shortened), the acceptance angle θ_a increases and the resolution error due to the aperture $\Delta r_{o,a}$ decreases. The opposite happens when d_a is decreased (or z_f is lengthened). Therefore, spatial resolution due to the aperture can be improved by increasing d_a or shortenting z_f, but at the expense of reducing image contrast, and vice versa.

Resolution error due to the acceptance angle is also a factor, as described by Equation 2-11 (reposted below):

$$\Delta r_{o,t} \approx \frac{\theta_a}{2}\left(z_f + z_i\right) = \frac{d_a}{2}\left(\frac{1}{M} + 1\right).$$

As d_a is decreased, $\Delta r_{o,a}$ (aperture) decreases while $\Delta r_{o,t}$ (acceptance angle) increases, and thus it remains unclear at first glance which is dominant.

8.1 SF ADI experimental results

This section presents experimental results conducted using the Spatial Filter setup (see *Chapter 3*) to verify and compare SF theory and actual behavior under a range of situations. The following figures present SF ADI results with 204 µm to 51 µm test structures placed in front of 5 cm of water or a highly scattering solution. Argon laser light (488 – 514 nm) provides full-field illumination for these experiments using the Keplerian spherical beam expander.

8.1.1 SF ADI with varying Scattering Ratio

The first and most important test of the spatial filter is how well its acceptance angle filters out the scattered light. Thus, in this section the aperture diameter d_a is fixed and images are taken at many scattering levels.

Figure 8-1, shown as follows, presents SF ADI images for SR = 0:1 (water) to 2×10^8:1 with a fixed converging lens focal length (z_f = 50 mm) and aperture diameter d_a = 300 µm. Image distance z_i = 50 mm is equal to z_f, and thus image magnification M is set to unity. From Equation 2-4, the acceptance angle can be calculated to be 0.34°.

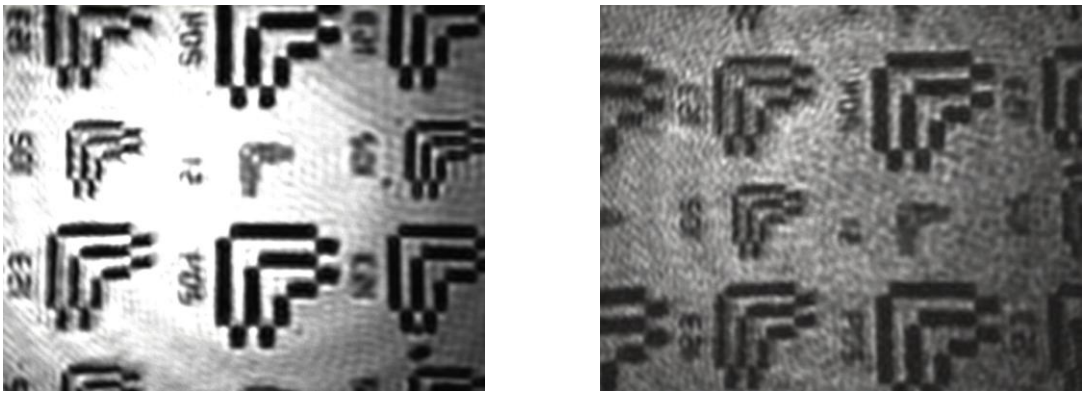

(a) SR = 0:1 (water), t_{exp} = 0.11 ms

(b) SR = 5×10^5:1, t_{exp} = 76.7 ms

(c) SR = 5.4×10^7:1, t_{exp} = 131.4 ms

(d) SR = 2×10^8:1, t_{exp} = 131.4 ms

Figure 8-1 SF ADI with z_f = 50 mm, z_i = 50 mm, and d_a = 300 µm for varying SR values.

For the SR = 0:1 (water) scan, the test structures are clearly visible with good contrast, although interference patterns are visible (as they are across the other SR values). At SR = 5×10^5:1, the test structures are still clearly visible but contrast begins to degrade. At SR = 5.4×10^7:1, contrast is poor but the test structures are still visible, while at SR = 2×10^8:1 the test structures are no longer clearly visible in the image.

Image resolution in Figure 8-1 appears to be at 102 µm or better for all SR values when objects are visible. The lines and spaces of the smallest 51 µm test structure are not individually distinguishable, but the structure on the whole is detectable in the image. Image resolution appears to stay constant even as the SR is increased from 0:1 (Figure 8-1a) to 5.4×10^7:1 (Figure 8-1c). Thus, increasing SR does not appear to have any significant effect on image resolution. It should be noted that these SF images were

captured one image at a time with short exposure times ranging from 0.11 ms to 131.4 ms. This is much faster than the line-by-line scanning which is required by the AFA ADI technique, which can average up to 1 to 2 minutes per scan.

As the scattering level is increased, image contrast degrades until the test structures appear indistinguishable at SR = 2×10^8:1, which appears to be at the scattering limit for this SF ADI setup. Figure 8-2, shown as follows, presents line profile plots across a 204 µm test structure line in each of the SR = 0:1 to 5.4×10^7:1 scans.

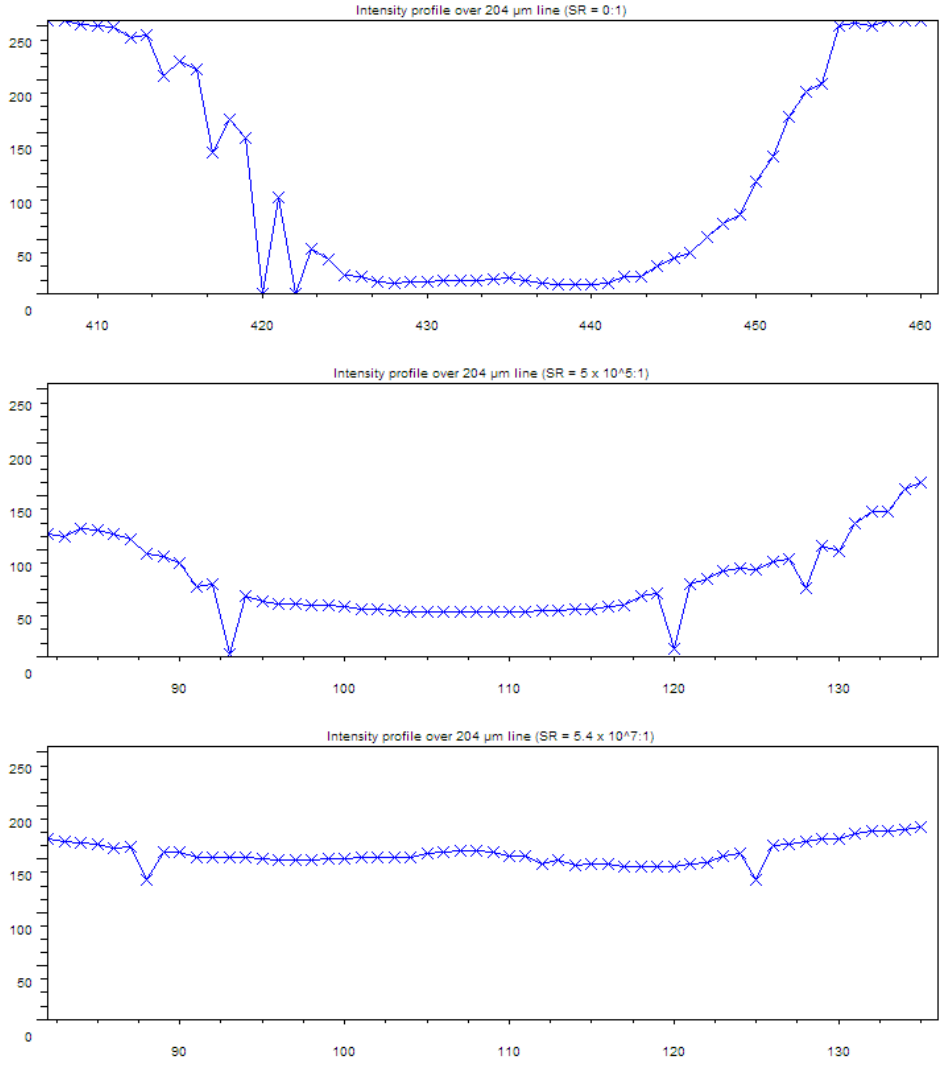

Figure 8-2 Intensity line profile across a 204 µm line for varying SR values and aperture diameters.

From Figure 8-2, we can estimate contrast ratios of 0.91, 0.46, and 0.06 for SR = 0:1, 5×10^5:1, and 5.4×10^7:1, respectively. These results clearly indicate that contrast degrades significantly with increasing SR, which is to be expected because higher scattering levels lead to higher background scattered noise-to-signal levels.

Table 8-1 presents a summary of the SR experiments in this section.

Table 8-1 Summary results, calculations, and measurements for SF ADI as from Pfeiffer et al [22].

Figure No.	**Acceptance angle θ_a (degrees)**	**Aperture Dia. d_a (µm)**	**Scattering Ratio *SR***	***Aperture Resolution*** $\Delta r_{o,a}$ ***(µm)***	***Trajectory Resolution*** $\Delta r_{o,t}$ ***(µm)***	**Measured Resolution Δr_o (µm)**
Figure 8-1a	0.34	300	0 (water)	***85.7***	***300***	50-100
Figure 8-1b	0.34	300	5.0×10^5	***85.7***	***300***	50-100
Figure 8-1c	0.34	300	5.4×10^7	***85.7***	***300***	100
Figure 8-1d	0.34	300	2.0×10^8	***85.7***	***300***	not observable

As indicated above, the acceptance angle of this SF setup is 0.34°, which is similar to the slightly more restrictive the acceptance angle of the AFA device (0.29°). With this acceptance angle, test structures at SR values up to 5.4×10^7 can be resolved with ~100 µm resolution and full circular illumination. These results show performance on par with or better than the AFA with spherical beam expander setup (which reaches its scattering limit at SR ~ 10^6:1).

It should be noted that the circular ringed patterns which appear in water and all SR samples are caused by interference effects from the optical setup that could not be suppressed. One source of circular ring interference is reflection off the faces of the lenses that comprise the Keplerian beam expander and spatial filter, resulting in constructive and destructive interference. Intentionally misaligning the lenses does not appear to correct the problem, which suggests that interference is occurring due to reflections within individual lenses, rather than reflection between lenses. A second source of circular rings is from the diffraction due to the SF aperture. Interference from the aperture is not very noticeable at the largest aperture diameter, but becomes more pronounced at smaller aperture diameters. Finally, a diagonal interference pattern of lines is visible in all images, and appears to occur at the image sensor. This appears to be from the glass covering and glass layers of the sensor. One approach to reducing these

interference effects is to replace the illumination source with a low coherence emitter, such as a spectrally wide light emitting diode (LED) or incoherent source.

8.1.2 SF ADI with varying aperture diameter

According to theory, decreasing the aperture diameter d_a should lead to increased contrast due to a reduced acceptance angle (Equation 2-4), but an increase in resolution error due to the aperture (Equation 2-10). At the same time, resolution error due to trajectory filtering (Equation 2-11) is predicted to decrease along with d_a. The results in this section indicate which of these resolution errors is dominant.

The following figure (Figure 8-3) presents images with varying aperture diameters ranging from d_a = 300 µm to 100 µm, at a constant SR of 1.4×10^7:1.

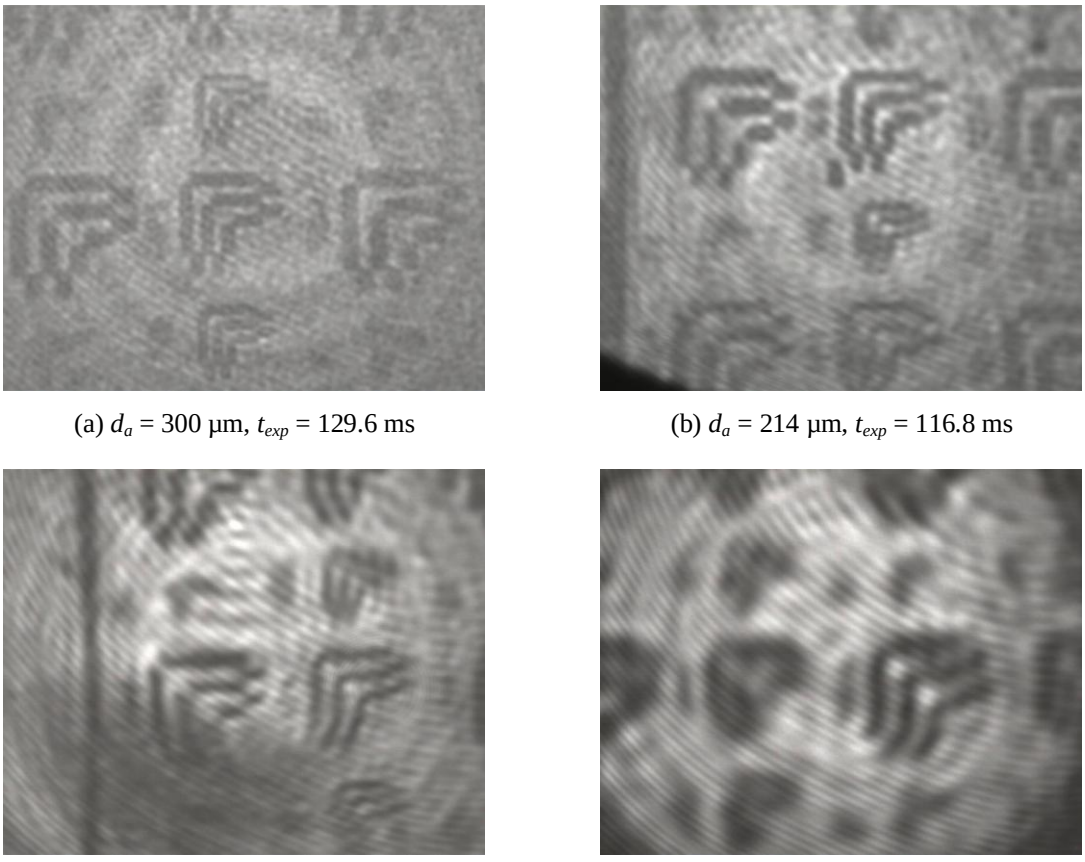

(a) d_a = 300 µm, t_{exp} = 129.6 ms

(b) d_a = 214 µm, t_{exp} = 116.8 ms

(c) d_a = 161 µm, t_{exp} = 120.5 ms

(d) d_a = 100 µm, t_{exp} = 118.7 ms

Figure 8-3 SF ADI with z_f = 50 mm and z_i = 50 mm at SR = 1.4×10^7:1 with varying aperture diameters.

As d_a is reduced from 300 µm (Figure 8-3a) to 100 µm (Figure 8-3b), we see that image contrast increases, while image resolution decreases and the test structures appear blurrier. These results confirm and show that the resolution error due to aperture is the resolution limiting factor under these conditions, and also indicate a trade-off between image resolution and contrast. Features as small as 102 µm are resolvable for d_a = 300 µm to 161 µm, while only the 204 µm-sized features are resolvable at d_a = 100 µm. Figure 8-2, shown as follows, presents line profile plots across three 204 µm test structure lines in each of the scans.

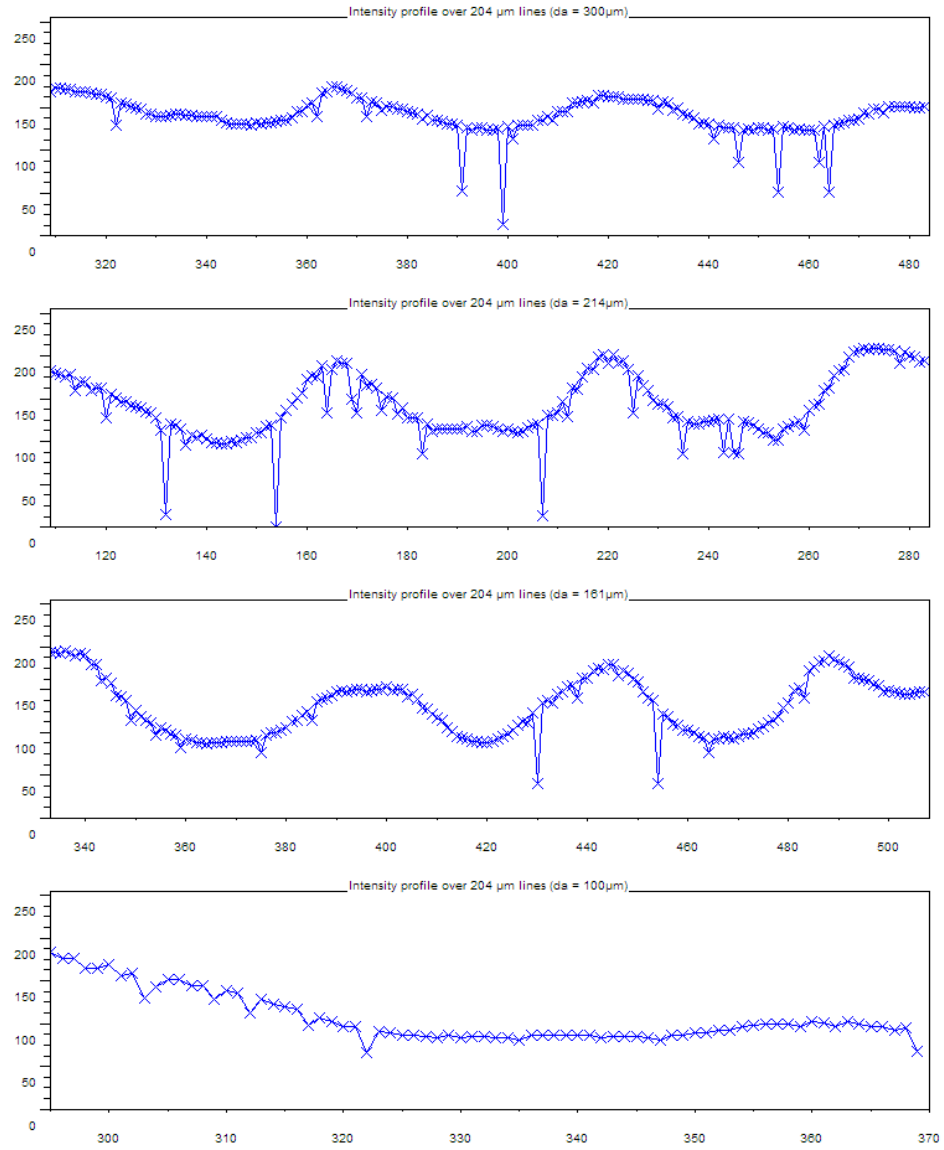

Figure 8-4 Intensity line profile across three 204 µm lines at SR = 1.4 × 10^7:1 with d_a = 300 µm, 214 µm, 161 µm, and 100 µm.

As shown by Figure 8-2, as the aperture diameter is reduced from 300 µm to 214 µm, the contrast ratio increases from approx. 0.15 to 0.30. For d_a = 161 µm, the contrast ratio is approx. 0.38 (left part of intensity plot), but loss of resolution leads to blurring of the test structure lines, which in turn lowers the contrast ratio between the 204 µm test lines. Similarly, for d_a = 100 µm, the contrast ratio is approx. 0.35 between the area outside the test structure and inside the test structure, with the test structures blurred together with the surrounding regions.

Table 8-2 presents a summary of the experiments with varying aperture diameter in this section.

Table 8-2 Summary results, calculations, and measurements for SF ADI as from Pfeiffer et al [22].

Figure No.	**Acceptance angle θ_a (degrees)**	**Aperture Dia. d_a (µm)**	**Scattering Ratio *SR***	***Aperture Resolution*** $\Delta r_{o,a}$ ***(µm)***	***Trajectory Resolution*** $\Delta r_{o,t}$ ***(µm)***	**Measured Resolution Δr_o (µm)**
Figure 8-3a	0.34	300	1.4×10^7	***85.7***	***300***	100
Figure 8-3b	0.25	214	1.4×10^7	***120.1***	***214***	100-150
Figure 8-3c	0.18	161	1.4×10^7	***159.6***	***161***	100-150
Figure 8-3d	0.11	100	1.4×10^7	***257***	***100***	150-200

As indicated above, the calculated resolution error due to aperture ($\Delta r_{o,a}$) increases (worsens) as d_a is decreased, which appears to be the dominant effect observed in the previous images (i.e. resolution worsens with smaller d_a). Conversely, the acceptance angle is found to decrease along with d_a, and this results in the increased contrast as observed in Figure 8-3.

8.1.3 SF ADI results with varying image distance (magnification)

The experiments in this section examine the effect of reducing the aperture diameter but at half the image distance z_i (half times image magnification). The expectation that resolution error and contrast increase as d_a is decreased will be verified at a magnification M of 0.5 times.

The following figure (Figure 8-5) presents images taken with a varying d_a of 300 µm to 100 µm similar to the previous figure, but with z_i = 25 mm (i.e. M = 0.5).

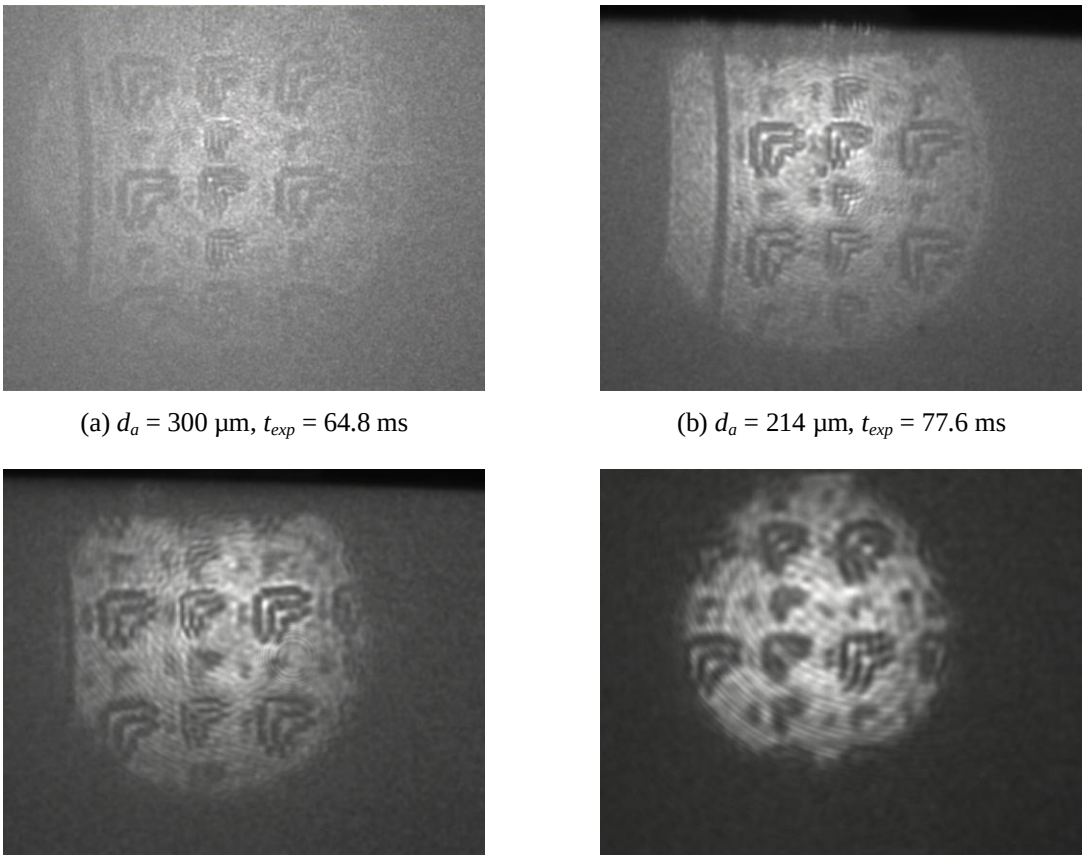

(a) d_a = 300 µm, t_{exp} = 64.8 ms

(b) d_a = 214 µm, t_{exp} = 77.6 ms

(c) d_a = 161 µm, t_{exp} = 81.2 ms

(d) d_a = 100 µm, t_{exp} = 28 ms

Figure 8-5 SF ADI with z_f = 50 mm and z_i = 25 mm at SR = 1.4 × 10^7:1 with varying aperture diameters.

As expected, image contrast improves as aperture diameter is reduced, while image resolution degrades. One difference with results for M = 0.5 is that the smallest resolvable feature size increases to 153 µm for $d_a \geq$ 161 µm. For d_a = 100 µm, the smallest resolvable feature increases to 204 µm. These results illustrate the trade-off that exists between image contrast and resolution as the aperture diameter is changed.

Table 8-3 presents a summary of the experiments with varying aperture diameter in this section.

Table 8-3 Summary results, calculations, and measurements for SF ADI as from Pfeiffer et al [22].

Figure No.	Acceptance angle θ_a (degrees)	Aperture Dia. d_a (µm)	Scattering Ratio *SR*	*Aperture Resolution* $\Delta r_{o,a}$ *(µm)*	*Trajectory Resolution* $\Delta r_{o,t}$ *(µm)*	Measured Resolution Δr_o (µm)
Figure 8-5a	0.34	300	1.4×10^7	***85.7***	***450***	200
Figure 8-5b	0.25	214	1.4×10^7	***120.1***	***321***	150
Figure 8-5c	0.18	161	1.4×10^7	***159.6***	***241.5***	150
Figure 8-5d	0.11	100	1.4×10^7	***257***	***150***	200

As indicated above, the calculated resolution error due to aperture ($\Delta r_{o,a}$) increases as d_a is decreased, which appears to be the dominant effect observed in the previous images (i.e. resolution decreases along with d_a). Conversely, the acceptance angle decreases along with d_a, which results in the increased contrast as observed. These results are consistent with those observed at M = 1, except that larger resolution error due to trajectory ($\Delta r_{o,t}$) values appear to result in greater measured resolution (Δr_o) errors for M = 0.5.

8.1.4 SF ADI with varying converging lens focal length

According to theory, the major effect on image quality for increasing the focal length of the converging lens is to decrease contrast due to an increased acceptance angle (Equation 2-4) while increasing resolution error due to diffraction from the aperture (Equation 2-10). These effects from varying focal length are the exact inverse of varying aperture diameter.

The following figure (Figure 8-6) presents images taken at SR $\approx 10^7$:1 with both z_f = 35 mm, 50 mm, and 100 mm. Image distance z_i was set equal to z_f to keep magnification at unity.

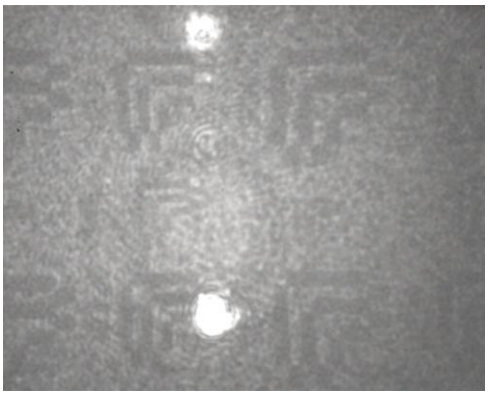

(a) z_f = 35 mm, z_i = 35 mm,
SR = 1.5 × 10^7:1, t_{exp} = 108.6 ms

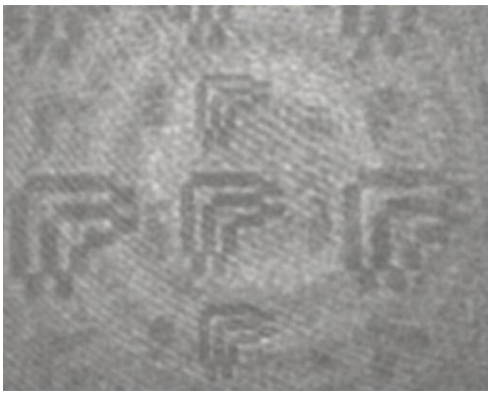

(b) z_f = 50 mm, z_i = 50 mm,
SR = 1.4 × 10^7:1, t_{exp} = 129.6 ms

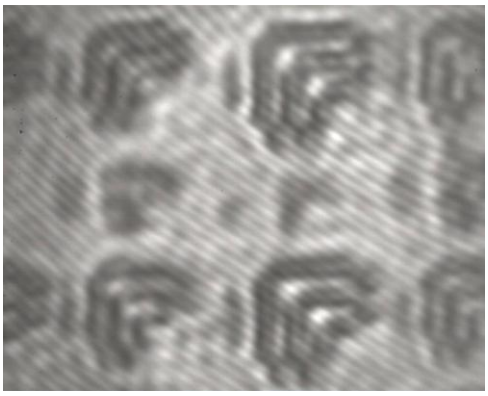

(c) z_f = 100 mm, z_i = 100 mm,
SR = 2.2 × 10^7:1, t_{exp} = 131.4 ms

Figure 8-6 SF ADI with d_a = 300 μm at SR ≈ 10^7:1 with varying z_f and z_i values from 35 mm to 100 mm.

The results in Figure 8-6 show that for short z_f values, resolution error is small while contrast is poor. However, as z_f is increased with magnification kept constant, resolution degrades while contrast improves. It should be noted that the bright spots in the first image (Figure 8-6a) are artefacts caused by reflections between optical elements in the setup and are not part of the sample. Figure 8-7, shown as follows, presents line profile plots across the 204 μm test structure lines for each of the scans.

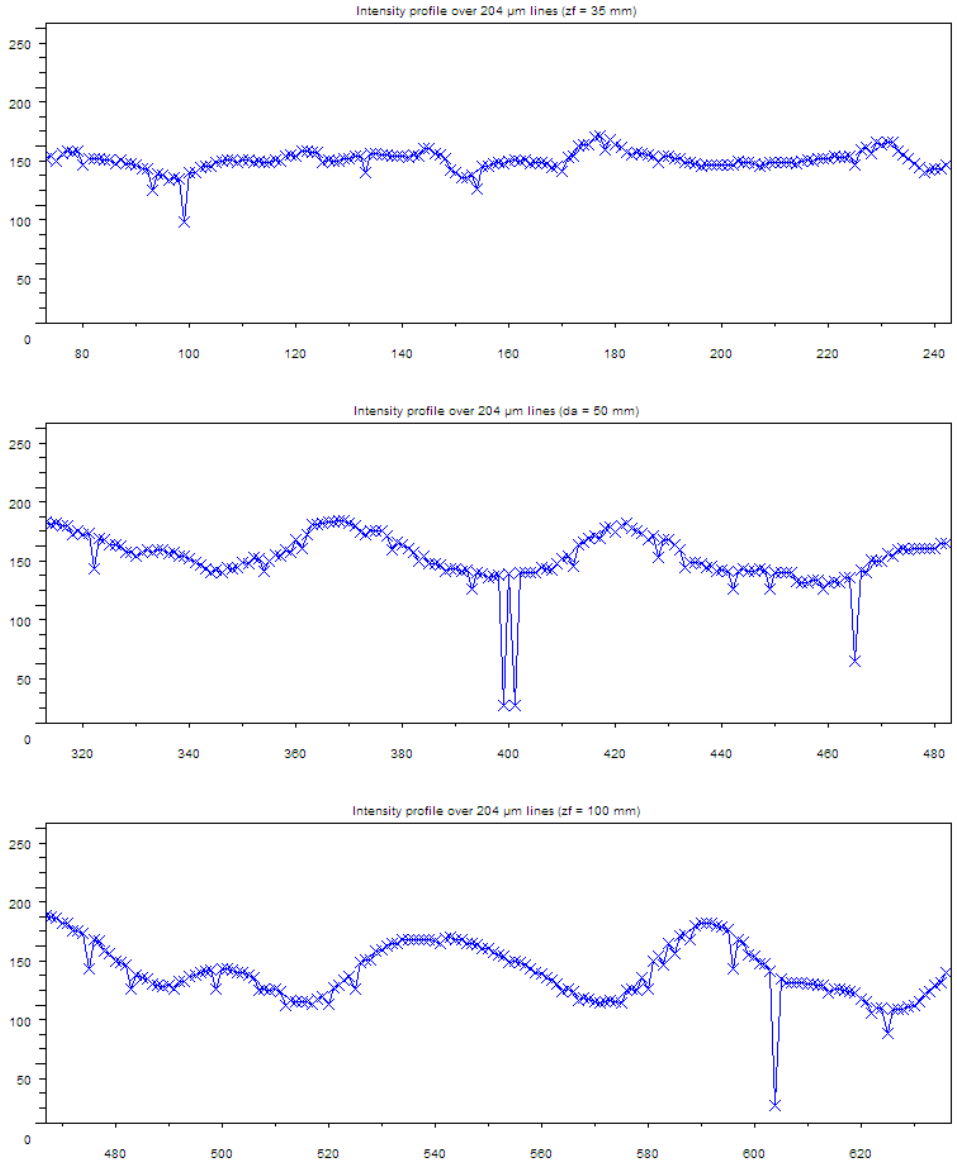

Figure 8-7 Intensity line profile across three 204 µm lines at SR ≈ 10^7:1 with z_f = 35 mm, 50 mm, and 100 mm.

As shown in Figure 8-7, at z_f = 35 mm, the contrast ratio is very low at approx. 0.09. However, as z_f is increased to 50 mm and 100 mm, the contrast ratio increases to approx. 0.17 and 0.21, respectively, while the profile plot becomes more gradual in slope (i.e. poorer image resolution). These results confirm previous theory, which predicted improved contrast and increased resolution error as z_f is increased.

Table 8-4 presents a summary of experiments with varying z_f and z_i.

Table 8-4 Summary results, calculations, and measurements for SF ADI as from Pfeiffer et al [22].

Figure No.	Acceptance angle θ_a (degrees)	Focal Distance z_f (mm)	Aperture Dia. d_a (µm)	Scattering Ratio *SR*	*Aperture Resolution* $\Delta r_{o,a}$ *(µm)*	*Trajectory Resolution* $\Delta r_{o,t}$ *(µm)*	Measured Resolution Δr_o (µm)
Figure 8-6a	0.49	35	300	1.5×10^7	***60.0***	***300***	150
Figure 8-6b	0.34	50	300	1.4×10^7	***85.7***	***300***	100
Figure 8-6c	0.017	100	300	2.2×10^7	***171.3***	***300***	150-200

As indicated above, as the focal length is decreased (along with z_i), the acceptance angle also decreases, which results in greater contrast ratio as observed. However, decreasing z_f also increases the resolution error due to aperture ($\Delta r_{o,a}$), which results in poorer spatial resolution as observed in Figure 8-6.

8.2 Imaging speed with the SF

A significant advantage belonging to the SF ADI approach compared to the current AFA ADI method is the ability to capture a full-frame image at once without requiring line-by-line scanning (as with the AFA). For example, at SR = 3.2×10^7:1, a typical image scan time takes 1 to 2 minutes using the AFA. However, a typical SF image capture time is only 131.4 ms at SR = 5.4×10^7:1, which is approximately 10^3 times faster in acquisition time. At such an imaging speed, video capture at 7.6 frames per second is possible. In addition, SF image capture time can be further reduced by increasing laser power, using a more sensitive camera, or boosting input gain.

8.3 Further discussion of predicted results with theory

Table 8-5 presents a summary of all the SF experimental results presented thus far and includes calculated and approximate measured values for object resolution.

Table 8-5 Summary results, calculations, and measurements for SF ADI as from Pfeiffer et al [22].

Figure No.	Focal Distance z_f (mm)	Image Distance z_i (mm)	Aperture Dia. d_a (µm)	Scattering Ratio *SR*	*Aperture Resolution* $\Delta r_{o,a}$ *(µm)*	*Trajectory Resolution* $\Delta r_{o,t}$ *(µm)*	Measured Resolution Δr_o (µm)
Figure 8-1a	50	50	300	0 (water)	***85.7***	***300***	50-100
Figure 8-1b	50	50	300	5.0×10^5	***85.7***	***300***	50-100
Figure 8-1c	50	50	300	5.4×10^7	***85.7***	***300***	100
Figure 8-1d	50	50	300	2.0×10^8	***85.7***	***300***	not observable
Figure 8-3a	50	50	300	1.4×10^7	***85.7***	***300***	100
Figure 8-3b	50	50	214	1.4×10^7	***120.1***	***214***	100-150
Figure 8-3c	50	50	161	1.4×10^7	***159.6***	***161***	100-150
Figure 8-3d	50	50	100	1.4×10^7	***257***	***100***	150-200
Figure 8-5a	50	25	300	1.4×10^7	***85.7***	***450***	200
Figure 8-5b	50	25	214	1.4×10^7	***120.1***	***321***	150
Figure 8-5c	50	25	161	1.4×10^7	***159.6***	***241.5***	150
Figure 8-5d	50	25	100	1.4×10^7	***257***	***150***	200
Figure 8-6a	35	35	300	1.5×10^7	***60.0***	***300***	150
Figure 8-6b	50	50	300	1.4×10^7	***85.7***	***300***	100
Figure 8-6c	100	100	300	2.2×10^7	***171.3***	***300***	150-200

As just mentioned, it is unclear from theory alone whether the actual spatial resolution will improve or worsen when d_a is decreased. In fact, the measured resolution error is almost always smaller in our results than predicted by the $\Delta r_{o,t}$ (acceptance angle) value, and instead more closely follows $\Delta r_{o,a}$ (aperture). The reason that the calculated $\Delta r_{o,t}$ value is not a hard limiting factor is because it was calculated (see Equation 2-11) under the worst-case assumption that light is scattered uniformly across all angles as it exits the medium. However, as indicated previously by H-G function modeling (see Figure 1-4), scattering materials with high g factors exhibit forward weighted scattering even after multiple scattering events. Thus, a forward weighted scattering distribution may explain why observed resolution error falls below the calculated $\Delta r_{o,t}$ value.

Table 8-5 shows that as z_f is increased, observed resolution error increases accordingly, as predicted by Equation 2-10. This effect is similar to the effect of decreasing d_a. Finally, it is observed that increasing SR alone does not appear to increase resolution error as long as the test structures are detectable, as expected from previous AFA research.

8.4 Chapter summary

This chapter compared predicted behavior from Spatial Filter theory to actual imaging results from the SF ADI setup. In accordance with previous research in AFA ADI, it was

found that increasing the SR of a scattering sample degrades contrast, but does not noticeably affect resolution. With an aperture diameter d_a = 300 μm, converging lens focal length z_f = 50 mm, and an image distance of z_i = 50 mm, the SF ADI system successfully resolved test structure lines and spaces of 102 μm for SR up to 5.4×10^7:1. At SR = 2×10^8:1, a scattering limit for this setup was reached with the test structures not clearly visible.

SF theory predicts that decreasing the aperture diameter increases image contrast and the resolution error due to aperture. With $z_f = z_i$ = 50 mm as before, this behavior was confirmed in actual experiments for d_a = 300 μm to 100 μm at a constant SR of 1.4×10^7:1. When z_i is reduced to 25 mm (i.e. half times magnification), the same relation between d_a and image contrast and resolution is observed, as expected from theory. These results also indicate that under those conditions, the resolution error due to aperture is dominant.

Theory regarding the focal length z_f of the converging lens was also confirmed. Results showed that as z_f is increased, contrast increases while image resolution degrades as a direct result of increased resolution error due to the aperture.

Both theory and results confirm that there exists a trade-off between image contrast and resolution error. By either decreasing d_a or increasing z_f, image contrast improves while resolution error increases, and vice versa. In addition, it was observed that under these experiment conditions, the resolution error due to aperture was more of the limiting factor in the final image, even when the the resolution error due to trajectory filtering was calculated to be higher. This result suggests that light may be significantly forward scattered in the scattering medium.

Interference patterns were observed in the SF images as a result of the optics setup. However, using only passive optics elements allowed for an entire SF ADI image to be captured at one time, which resulted in much faster imaging rates (e.g. hundreds of milliseconds) compared to AFA imaging (e.g. 1 to 2 minutes) at high SR values.

SF ADI results at high scattering levels indicate that SR ~ 10^7:1 to 10^8:1 represents the scattering limit for the current setup. Higher SR's may be reached in the future by limiting the illumination area from the full sample region to a smaller region, such as by using a thin line of illumination or "pencil" beam for imaging. In addition, reducing the aperture diameter can enable the detection of test objects at higher scattering levels, but at a cost of spatial resolution.

The following chapter presents conclusions for this thesis and thoughts on future work.

Chapter 9

Conclusions

This thesis has investigated several features of the Angular Domain Imaging method for Optical Tomography in scattering media. To begin with, wavelength independent operability was demonstrated in moving from a 488-514 nm Argon ion laser to a 670 nm laser diode source for the Angular Filter Array setup. Milk-solution experiments demonstrated lower scattering coefficients at λ = 670 nm as compared to Argon ion wavelengths, such that higher concentrations were required to achieve the same Scattering Ratio levels. Image results (λ = 670 nm) at high SR proved comparable with previous Argon laser experiments, with the maximum SR achievable of 10^7:1 falling in line between the limit for the spherical beam expander Argon laser system (SR ~10^6:1) and the Cylindrical-Spherical-Cylindrical beam shaper Argon laser system (SR ~ 10^8:1).

ADI at λ = 670 nm was capable of successfully resolving images of sub-millimeter (204 µm or better) test objects in chicken breast tissue up to 3.8 mm thick. Chicken breast tissue was found to exhibit unexpectedly high scattering levels which indicate the presence of high levels of surface scattering at the glass and tissue sample interface. In addition, the tissue samples contained non-uniformities intrinsic to the tissue that obscured the artificial test structures during imaging. However, these results demonstrate successful imaging of biological tissues at λ = 670 nm in AFA ADI.

Two methods were employed to reduce the effect of scattered light that is reflected and transmitted through the AFA tunnels. Carbon deposition by physical evaporation was shown to be modestly effective in reducing reflected light within the AFA tunnels, but led to occlusion of the tunnels due to debris. Tunnel surface roughening via NH_4OH etching was found to be a more effective solution in increasing attenuation of reflected light within the tunnels, with a much smaller impact on AFA occlusion and degredation.

Smaller AFA tunnel geometries (25.5 µm widths) were demonstrated to improve horizontal spatial resolution in experiments from 102 µm to 52 µm, although diffraction

effects became more evident. Smaller vertical step sizes also improved vertical spatial resolution from 102 μm to 52 μm when step sizes were reduced from 52 μm to 26 μm.

All previous ADI work has employed microcollimator Angular Filter Arrays. This thesis examined an alternative, a spatial filter employing a converging lens and aperture. Experiments were used to compare theoretical predictions of the SF with actual results. ADI with spatial filtering at λ = 488-514 nm proved successful at resolving images at SR = 1.4×10^7:1 with 102 μm resolution or better, with an aperture diameter d_a of 300 μm and a converging lens focal length z_f of 50 mm. Increasing SR was shown to significantly degrade image contrast, but with no noticeable effect on image resolution. Both image contrast and image resolution error were found to be directly proportional to the z_f, while inversely proportional to d_a. Thus, there exists a trade-off between image contrast and resolution performance, where improving one negatively affects the other. It was found that observed resolution was more closely limited by the resolution error due to the aperture compared to resolution error due to trajectory filtering, which suggests that scattered light emerging from the scattering medium is forward peaked in angular distribution. Imaging speed was demonstrated to be a major advantage for SF ADI over AFA ADI, with an entire image able to be captured in 131 ms at high SR values, compared to scan times of up to 1 to 2 minutes for the AFA ADI setup.

9.1 Future work

Laser diodes of different wavelengths can be employed to gain additional information from a sample. Multi-spectral imaging can be explored where multiple wavelengths of illumination are employed to image the same sample, potentially simultaneously.

The 670 nm laser diode ADI setup can be improved by modifying the beam shaping optics to produce a thinner beam of light. This change should decrease the scattered to non-scattered light proportion reaching the AFA and improve image contrast, thus allowing media with higher SR's to be imaged.

ADI with different wavelengths and illumination sources can be explored. Multispectral imaging can yield new and complementary information depending on the scattering sample. Fluorescence can also be utilized as an alternate imaging technique.

Further work remains to be performed to better understand and characterize the surface scattering effect observed for our chicken breast tissue samples. In addition, techniques such as immersing the tissue sample in an index matching fluid should be employed in order to minimize the surface scattering effect.

Techniques for modifying the AFA tunnels to reduce reflected and scattered light transmission can be further explored, including thin film deposition and surface topology roughening. New tunnel dimensions and aspect ratios (acceptance angles) should be studied in order to determine potential performance enhancements and trade-offs in image contrast and resolving power.

Digital image processing techniques show promise in significantly improving image contrast and detectability. Complementary techniques, such as using a wedge prism to deviate the illumination beam and capture only the scattered light information [30], have proven to work well with digital image processing in increasing the maximum scattering limit at which ADI can operate.

Reference List

[1] International Agency for Research on Cancer, "Overall Evaluations of Carcinogenicity to Humans," *International Agency for Research on Cancer*. [Online]. Available: http://monographs.iarc.fr/ENG/Classification/crthgr01.php [Accessed Jan 5, 2008].

[2] G.H. Chapman, P.K.Y. Chan, J. Dudas, J. Rao and N. Pfeiffer, "Angular Domain Image Detectability with Changing Turbid Medium Scattering Coefficients", *Proc. SPIE Int. Soc. Opt. Eng. 5695,* pp. 160-171, 2005.

[3] G. Chapman, M. Trinh, N. Pfeiffer, G. Chu, and D. Lee, "Angular Domain Imaging of Objects Within Highly Scattering Media Using Silicon Micromachined Collimating Arrays," *IEEE Journal of Selected Topics in Quantum Electronics,* vol. 9, no. 2, pp. 257-266, 2003.

[4] M. Tank, "Development of a Silicon Micromachined Collimator Array to Detect Objects within Highly Scattering Mediums," M.A.Sc. thesis, Simon Fraser University, Burnaby, BC, Canada, 2001.

[5] G. Chu, "Probing Structures in Scattering Medium using a Silicon Micromachined Collimator Array," B.A.Sc. thesis, Simon Fraser University, Burnaby, BC, Canada, 2001.

[6] M. Trinh, "Pushing the Limits of Optical Tomography Using a Silicon Micromachined Collimator Array," B.A.Sc. thesis, Simon Fraser University, Burnaby, BC, Canada, 2002.

[7] D. Lee, "Imaging Objects at Various Depths in Scattering Mediums Using a Silicon Micromachined Collimating Array," B.A.Sc. thesis, Simon Fraser University, Burnaby, BC, Canada, 2002.

[8] B. Wai, “Angular Domain Optical Tomography Using Silicon Micromachined Collimating Arrays,” B.A.Sc. thesis, Simon Fraser University, Burnaby, BC, Canada, 2004.

[9] P. Chan, “Exploring the Limits of Silicon Micromachined Collimating Array Assisted Optical Tomography” B.A.Sc. thesis, Simon Fraser University, Burnaby, BC, Canada, 2005.

[10] F. Vasefi, P. K. Y. Chan, B. Kaminska, G. H. Chapman, and N. Pfeiffer, “An Optical Imaging Technique Using Deep Illumination in the Angular Domain,” *IEEE J. Sel. Topics Quantum Electron.*, vol.13, no.6, pp. 1610-1620, 2007.

[11] A. F. Fercher, W. Drexler, C. K. Hitzenberger, and T. Lasser, ‘‘Optical coherence tomography–principles and applications,’’ *Rep. Prog. Phys.*, vol. 66, pp. 239–303, 2003.

[12] V. Peters, D. Wyman, M. Patterson, and G. Frank, “Optical properties of normal and diseased human breast tissues in the visible and near infrared,” *Physics in Medicine and Biology*, vol. 35, no. 9, pp. 1317-1334, Sept. 1990.

[13] S. L. Jacques, C. A. Alter, S. A. Prahl, "Angular dependence of HeNe laser light scattering by human dermis," *Lasers Life Sci.*,vol. 1, pp. 309-333, 1987.

[14] S. Jacques, “ECE 532 Introduction to Biomedical Optics,” *Oregon Graduate Institute*. [Online]. 2002, http://omlc.ogi.edu/classroom/ece532/index.html [Accessed: 4 February 2008].

[15] D. Grosenick, K. Moesta, H. Wabnitz, J. Mucke, C. Stroszczynski, R. Macdonald, P. Schlag, and H. Rinneberg, “Time-domain optical mammography: initial clinical

results on detection and characterization of breast tumors," *Appl. Opt.*, vol. 42, pp. 3170–86, 2003.

[16] A. P. Gibson, J. C. Hebden, and S. R. Arridge, "Recent advances in diffuse optical imaging," *Phys. Med. Biol.*, vol. 50, pp. R1-R43, 2005.

[17] B. B. Das, F. Liu, and R. R. Alfano, "Time-resolved fluorescence and photon migration studies in biomedical and model random media," *Rep. Prog. Phys.*, vol. 60 pp. 227–92, 1997.

[18] A. Pifferi, P. Taroni, A. Torricelli, F. Messina, and R. Cubeddu, "Four-wavelength time-resolved optical mammography in the 680–980 nm range," *Opt. Lett.*, vol. 28, pp. 1138–40, 2003.

[19] W. Drexler, "Ultrahigh resolution optical coherence tomography," *J. Biomed. Opt.*, vol. 9, pp. 47-74, 2004.

[20] Nikon, Inc., "Introduction to Confocal Microscopy: Basic Concepts," *Nikon MicroscopyU*. [Online]. 2008, http://www.microscopyu.com/articles/confocal/confocalintrobasics.html [Accessed: 11 August 2008].

[21] F. Vasefi, P. K. Y. Chan, B. Kaminska, G. H. Chapman, "Deep illumination angular domain imaging within highly scattering media enhanced by image processing", *Proc. SPIE Int. Soc. Opt. Eng. 6380*, pp. 63800Q-1 – 12, 2006.

[22] N. Pfeiffer, P. Chan, G. H. Chapman, F. Vasefi, and B. Kaminska, "Optical imaging of structures within highly scattering material using a lens and aperture to form a spatiofrequency filter", *Proc. SPIE Int. Soc. Opt. Eng. 6854*, 68541D, 2008.

[23] J. W. Goodman, “Introduction to Fourier Optics”, 2d ed., San Francisco: *McGraw-Hill*, 1996, pp. 96-171.

[24] G.H. Chapman, J. Rao, T. Liu, N. Pfeiffer, and P.K.Y. Chan, “Enhanced Angular Domain Imaging in Turbid Media using Gaussian Line Illumination”, *Proc. SPIE Int. Soc. Opt. Eng.* 6084, 60841D, 2006.

[25] P. K. Y. Chan, F. Vasefi, G. H. Chapman, B. Kaminska, and N. Pfeiffer, “Multispectral angular domain optical tomography in scattering media with argon and diode laser sources", *Proc. SPIE Int. Soc. Opt. Eng. 6435*, 64350M, 2007.

[26] Sony Corporation, "SLD1332V," *Sony Global – Sony Semiconductor*. [Online]. Available: http://www.sony.net/Products/SC-HP/laserdiodewld/products/pdf/sld1332v.pdf [Accessed: July 18, 2008].

[27] J. Dykes, C. Plesa, and G. H. Chapman, “Enhancing direct-write laser control techniques for bimetallic grayscale photomasks”, *Proc. SPIE Int. Soc. Opt. Eng. 6883*, 688312, 2008.

[28] J. Dudas, “An Improved Detection System for Angular Domain Optical Tomography,” B.A.Sc. thesis, Simon Fraser University, Burnaby, BC, Canada, 2005.

[29] G. Marquez, L. Wang, S. Lin, J. Schwartz, and S. Thomsen, “Anisotropy in the Absorption and Scattering Spectra of Chicken Breast Tissue,” *Appl. Opt. 37*, 798-804, 1998.

[30] F. Vasefi, G. H. Chapman, P. K. Y. Chan, B. Kaminska, N. Pfeiffer, “Enhanced angular domain optical imaging by background scattered light subtraction from a deviated laser source”, *Proc. SPIE Int. Soc. Opt. Eng. 6854*, pp. 68541E, 2008.

[31] F. Vasefi, P. K. Y. Chan, B. Kaminska, G. H. Chapman, "Subsurface Bioimaging using Angular Domain Optical Backscattering Illumination," *Proc. 27th IEEE EMBS*, pp. 1932-1936, 2006.

[32] P. Chan, "An Investigation of Spatial Resolution Enhancements for Angular Domain Optical Imaging," University of British Columbia, Vancouver, Canada, EECE 544 Medical Imaging – Project Report, 2006.

Appendices

Appendix A: Miscellaneous Alignment Procedures

The contents of this section have been taken from the author's undergrad thesis, with some adaptations [9].

A.1 Spherical lens beam expander

Aligning the spherical lens beam expander with the laser light source is relatively simple. Each lens should first be auto-collimated with the laser beam, and the beam should be situated directly in the center of each beam. Depending on the focal lengths of the lenses used, the two lenses (one plano-concave; the other plano-convex) should be placed approximately $f_1 + f_2$ apart. The configuration used in the undergraduate research involved focal lengths of –25 mm and 225 mm, respectively. As a result, the separation distance between the two lenses should be approximately 20 cm. A diagram of the two spherical lenses and their relation to each other was shown previously. The end result of the cylindrical beam expander should be a beam that is 10x larger in diameter and is collimated and neither converges nor diverges.

A.2 AFA and 6 degree-of-freedom jig

The main goal in aligning the AFA is to be able to image a line of illuminated AFA tunnels of maximum intensity, as illustrated in the following figure (taken from Figure A-1).

Figure A-1 An image of the line of tunnels for an aligned SMCA device.

The first step in properly aligning the AFA device with the incoming light source is to bring the AFA fairly close to the CCD camera to within 1.5 cm or less. If the AFA is too far from the CCD, the CCD will not be able to pick up the very diffuse light from the illuminated AFA tunnels. The second step is to adjust the (vertical-axis) pitch and

(horizontal axis) yaw of the AFA so that light can pass through the tunnels; these pitch and yaw adjustments must be made to yield the highest intensity of illumination in the tunnels. Finally, the roll of the AFA must be adjusted in order to have a horizontal line of illuminated AFA tunnels. This is necessary because the *Ctrl2.exe* program captures horizontal line images (within a 3-pixel high region, by default); thus, it is imperative that the illuminated AFA tunnels are level with the CCD and centered about an identical y-coordinate in order that a level, horizontal line image can be captured. Maintaining the levelness of the line scans is important because the horizontal scans are added directly on top of each other, from bottom to top, to form a full 2-dimensional image.